Search for Second Generation Scalar Leptoquarks using the ATLAS Detector

Dissertation zur Erlangung des
naturwissenschaftlichen Doktorgrades
der Julius-Maximilians-Universität Würzburg

vorgelegt von

Jason Tam

aus Auckland, New Zealand

Lehstuhl für Physik und ihre Didaktik
Physikalisches Institut
Julius-Maximilians-Universität Würzburg

Würzburg, 2014

Eingereicht am: 24.07.2014
bei der Fakultät für Physik und Astronomie
1. Gutachter: .....
2. Gutachter: .....
3. Gutachter: .....
der Dissertation.

Vorsitzende(r).....

1. Prüfer: .....
2. Prüfer: .....
3. Prüfer: .....

im Promotionskolloquium.
Tag des Promotionskolloquiums: .....
Doktorurkunde ausgehändigt am: .....

Abstract

Leptoquarks are hypothetical particles that attempt to explain the coincidental similarities between leptons and quarks included in SM. Their exact properties vary between different theoretical models, and there are no strong theoretical constraints on their possible mass values. They can possibly be produced from particle collisions, and there have already been searching efforts at previous collider experiments. Their presence have yet been observed, and this fact has been translated into lower bound exclusions on their possible mass values. The Large Hadron Collider (**LHC**) being the most recently constructed particle collider with the highest collision energies ever achieved experimentally, provides a new platform to continue the search for Leptoquarks at even higher mass ranges.

This thesis describes a search for pair-produced second-generation Leptoquarks using 20.3 fb^{-1} of data recorded by the ATLAS detector of LHC at $\sqrt{s} = 8$ TeV. Events with two oppositely charged muons and two or more jets in the final state were used. Candidate leptoquark events were selected with the help of four observables: the di-muon invariant mass ($M_{\mu\mu}$), the sum of the p_T of the two muons (L_T), the sum of the p_T of the two leading jets (H_T) and the average Leptoquark mass (M_{LQ}). Monte Carlo simulations of SM background processes have shown to be in good agreement with data, both in the region constructed using selection requirements for candiate leptoquark events and in the designated control regions. Since no significant excess of events was observed in data, a exclusion limit was set as a function of the Leptoquark mass.

Zusammenfassung

Leptoquarks sind hypothetische Teilchen, mit deren Hilfe versucht wird die zufälligen Ähnlichkeiten zwischen den im Standardmodell enthaltenen Leptonen und Quarks zu erklären. Ihre exakten Eigenschaften variieren zwischen verschiedenen theoretischen Modellen und es gibt keine starken theoretischen Beschränkungen auf ihre möglichen Massen. Sie können wohl bei Teilchenkollisionen erzeugt werden und es gab bereits an früheren Beschleuniger-Experimenten Bemühungen bei der Suche nach ihnen. Ihre Existenz konnte bisher nicht beobachtet werden, was in untere Ausschlussgrenzen für mögliche Massen übertragen wurde. Der zuletzt gebaute Teilchenbeschleuniger, der Large Hadron Collider (LHC) erreicht die bisher höchsten Kollisionsenergien und bietet damit eine neue Grundlage, um die Suche nach Leptoquarks bei noch höheren Massenregionen fortzusetzen.

Diese Arbeit beschreibt eine Suche für paarerzeugte Leptoquarks der zweiten Generation, wobei 20,3 fb^{-1} Daten vom ATLAS Detektor am LHC bei $\sqrt{s} = 8$ TeV benutzt wurden. Es wurden Ereignisse mit zwei gegensätzlich geladenen Myonen und zwei oder mehr Jets im Endzustand verwendet. Leptoquark-Kandidaten wurden mit der Hilfe vierer Observablen selektiert: die Dimuon invariante Masse ($M_{\mu\mu}$), die Summe des p_T der beiden Myonen (L_T), die Summe des p_T der beiden führenden Jets (H_T) und die durchschnittliche Leptoquarkmasse (M_{LQ}). Es erwies sich, dass die Monte Carlo Simulationen von Standardmodell-Untergrundprozessen sowohl in der Region, die unter Verwendung der Selektionsbedingungen für Ereignisse mit Leptoquark-Kandidaten gestaltet wurde, als auch in den gewählten Kontroll-

Regionen in guter Übereinstimmung mit den Daten sind. Da kein signifikanter Überschuss an Ereignissen in den Daten beobachtet werden konnte, wurde eine Ausschlussgrenze in Abhängigkeit der Leptoquarkmasse bestimmt.

Contents

List of Figures

List of Tables

Chapter 1

Introduction

There has been a long history of mankind searching for the underlying patterns of mother nature, which has spanned from the largest to the smallest scale of observables. Pioneer achievements such as Kepler's law of planetary motion that uses rigorous mathematical equations to describe regularities and patterns of motions in nature have proven to be significant for later developments. Newton's theory of Gravitation and Laws of motion have became core foundations for many areas of physics, especially in the later categorized area of Classical Mechanics. Classical Mechanics describes the relationship between the motion of physical objects and forces, and have proven to be extremely accurate within the macroscopic domain.

Classical Mechanics starts to lose its accuracy as the conditions of the system move towards the extreme ends of the scale. Extension theories maintaining some of the core concepts such as Quantum Mechanics and Relativity have emerged as extentions to Classical Mechanics respectively at extremely small scales and speeds close to the speed of light. Systems at extremely small scales that are also moving at relativistic speeds are governed by Quantum Field Theory (**QFT**)[1], which describes the interactions between different fields at a fundamental level.

Particle Physics is the branch of physics that studies the constituents of matter and their interactions at the most fundamental level. Beginning from the experimental achievements of Thomson [2], Rutherford [3] and many other physicists in the late 19th and early 20th century that led to the structure model of the atom, through to present day QFT with contributions from Dirac, Pauli, Schrödinger and many other physicists. It studies the interactions of particles at sub-atomic level, and attempts to model these behaviours using the QFT framework [4].

1.1 The Standard Model

The Standard Model (**SM**) [4] of particle physics is a theoretical framework based on QFT that represent a summary our present day knowledge of nature at the sub-atomic scale. It is a combination of theoretical models that describes the interactions of fundamental particles [1] governed by the Electromagnetic, Weak and Strong nuclear forces. This collaborative effort from many physicists in the latter half of the 20th century has shown to be consistent within its range of predictions against experimental results. Despite its shortcomings in describing some of the current unexplained phenomena in experimental physics and observational cosmology (see Section 1.2), it is nevertheless assumed to be a low energy approximation of a more comprehensive theory. It is regarded as a solid foundation in the field of particle physics, and many theoretical models are proposed as extensions to it in attempt to answer these open questions (see Section 1.3).

The SM contains six different leptons and six different quarks, also referred to as *flavours*. All except the three neutrinos carry electric charge, while the quarks also carry colour charge that is responsible for the Strong interaction. They are all fermions and carry similar quantum numbers with different values, and are categorized in three different generations within their family according to the symmetries between some of their quantum numbers, as shown in Tables 1.1 and 1.2. There is also a corresponding *antiparticle* to each of the leptons and quarks, with the same mass but oppositely-signed quantum numbers such as the electric charge. Interactions of the particles and antiparticles are slightly different under the SM framework due to the violation of CP symmetry, but insufficient to explain the observed matter-antimatter asymmetry [5].

The structure of generations in both the quark group and lepton group share similarities. Particles in the higher generations have higher mass, but share the same quantum numbers as the lower generations. Each quark has a tendency of trans-

[1] Fundamental/Elementary particles are particles with no known substructure. They are believed to be the most basic building blocks of nature that can not be further divided.

forming itself to another flavour via the Weak interaction, and the relative tendencies between different quark flavours are described by the Cabibbo–Kobayashi–Maskawa (**CKM**) Matrix [6]. The quarks are transformed to a different flavour of a lighter mass by either emitting a W^+ or a W^- boson, then the W boson decays hadronically into a quark-antiquark pair. The leptons can also transform into lower generations through the creation of a neutrino of its own flavour and the emission of a W boson, then the W boson also decay into a lepton and a neutrino of the same lepton flavour.

Generation	Quarks	Q_{EM}	Spin	EM	Weak	Strong
1^{ST}	Up (u)	$\frac{2}{3}$	$\frac{1}{2}$	Yes	Yes	Yes
	Down (d)	$-\frac{1}{3}$	$\frac{1}{2}$	Yes	Yes	Yes
2^{ND}	Charm (c)	$\frac{2}{3}$	$\frac{1}{2}$	Yes	Yes	Yes
	Strange (s)	$-\frac{1}{3}$	$\frac{1}{2}$	Yes	Yes	Yes
3^{RD}	Top (t)	$\frac{2}{3}$	$\frac{1}{2}$	Yes	Yes	Yes
	Bottom (b)	$-\frac{1}{3}$	$\frac{1}{2}$	Yes	Yes	Yes

TABLE 1.1: Quarks in the Standard Model. The electromagnetic charge Q_{EM}, is presented as multiples of the fundamental charge unit. [7]

Gauge symmetry plays a key role in the Standard Model. Noether's theorem [8] states that every symmetry in nature represents a conservation law, and vice versa. For example, the laws of physics are invariant over translations in time, which relates to the conservation of energy. Such quantity in the Lagrangian of a system is considered a redundent degree of freedom referred to as the *gauge*, and transformations over such quantity does not effect the equations of motion. The Lagrangian of the SM that summarises the different dynamics of the system is invariant under certain gauge transformations, where the changes in some configurations of the underlying fields of the system result in identical observables. The properties of gauge bosons in SM reflect the gauge symmetry shared between

Generation	Leptons	Q_{EM}	Spin	EM	Weak	Strong
1^{ST}	Electron (e)	-1	$\frac{1}{2}$	Yes	Yes	No
	Electron-Neutrino (ν_e)	0	$\frac{1}{2}$	No	Yes	No
2^{ND}	Muon (μ)	-1	$\frac{1}{2}$	Yes	Yes	No
	Muon-Neutrino (ν_μ)	0	$\frac{1}{2}$	No	Yes	No
3^{RD}	Tau (τ)	-1	$\frac{1}{2}$	Yes	Yes	No
	Tau-Neutrino (ν_τ)	0	$\frac{1}{2}$	No	Yes	No

TABLE 1.2: Leptons in the Standard Model. The electromagnetic charge Q_{EM}, is presented as multiples of the fundamental charge unit. [7]

the particles they interact with. The interactions in SM are mediated by the exchange of gauge bosons (see Table 1.3) between the leptons and quarks, and the combination of all different interactions gives the SM a symmetry group structure of:

$$SU(3)_C \times SU(2)_L \times U(1)_Y$$

where $U(n)$ denotes the group of $n \times n$ unitary matrices, and $SU(n)$ denotes a subgroup of $U(n)$ with determinant 1. The electromagnetic and weak interactions are unified through the process of spontaneous symmetry breaking in the $SU(2)_L \times U(1)_Y$ group [9], representing the Electroweak (**EW**) sector of the SM, while $SU(3)_C$ describes the gauge symmetry of Strong interactions, representing the Strong/Quantum Chromodynamics (**QCD**) sector of SM.

All leptons and quarks except the three neutrinos experience the Electromagnetic interaction via the exchange of the massless photon (γ). The massive Z ($M_Z \sim 91$ GeV) and $W^\pm$ ($M_{W^\pm} \sim 80$ GeV) bosons are respectively exchanged during neutral and charged Weak interactions. Eight different types of gluons are exchanged

Interaction	Boson	Charge$_{EM}$	Spin	Group
Electromagnetic	Photon (γ)	0	1	$SU(2)_L \times U(1)_Y$
Weak	$W^{\pm}$	± 1	1	$SU(2)_L \times U(1)_Y$
	Z	0	1	$SU(2)_L \times U(1)_Y$
Strong	8 Gluons (g)	0	1	$SU(3)_C$

TABLE 1.3: Gauge bosons and their responsible interactions in the Standard Model. The electromagnetic charge Q_{EM}, is presented as multiples of the fundamental charge unit. [7]

between quarks with different *colour charges* in the Strong interaction. All quarks carry either the *red*, *blue* or the *green* colour charge, and both the quarks and gluons only exist in confined combinations that are balanced over this degree of freedom.

Additionally the massive scalar Higgs boson is also a part of SM. It is an excitation of the Higgs field, where the interaction with other SM particles allows them to acquire mass. The fermions couple to the Higgs field via Yukawa couplings to acquire mass, while $W^{\pm}/Z$ vector bosons acquire mass via Electroweak Symmetry Breaking (**EWSB**), also known as the Higgs Mechanism. [10]

The first scientific evidence for the existence of the Higgs boson came only recently from CERN in July 2012, where both the ATLAS and CMS experiments announced to have independently reached a result with a local significance greater than 5σ on the discovery of a new particle [11, 12]. A further combined result from both experiments in March 2014 states that, results from further tests on the newly discovered particle strongly suggests that it has no spin (scalar) and positive parity [13, 14, 15]. Coupled with the measured interactions between the new particle with other known particles, the combined results strongly agrees with the properties of Higgs boson. Further tests are needed to confirm whether the newly discovered particle is indeed the Higgs boson in SM, or alternatively in other

models containing multiple Higgs bosons.

1.2 Inadequacies of The Standard Model

Despite the successes to date in matching its predictions with the results from experiments, there are still many important observations in nature that cannot be explained by SM, such as:

- *Gravity*: SM does not include any sort of description for the gravitational force. "Graviton", the theoretically proposed gauge boson that is responsible for the gravitational force in ways similar to the gauge boson in SM, is yet to be observed. It would be a massless spin 2 particle that carries no electric charge, and it would be incompatible with SM. [16]

- *Dark Energy*: A hypothetical form of energy is proposed to be responsible for the observed universe that is expanding in an accelerating rate. There is no explanation for this phenomena within the SM. [17]

- *Dark Matter*: Cosmological observations of large structures such as Galaxy rotation curves and gravitational lensing of background radiation have shown discrepancies with predictions from gravitational theories. The discrepancies suggest the presence of non-visible mass additional to the visible matter discribed by the SM. No part in SM can be used to fill this gap. [18]

- *Matter/Antimatter Asymmetry* [19]: The imbalance between the amount of existing matter and antimatter in the observed universe today has yet to have any viable explanations with support from experimental results. Proposed modifications of the SM involving *CP violation* as an explanation for

this has yet to be observed from experiments. [5]

- *Neutrino Mass*: Neutrinos exists as massless particles within the SM framework. Results from neutrino oscillation experiments have shown that they have non-zero mass. [20]

These shortcomings of SM combined with its successes leads to the wide belief that it is a low energy approximation of a more complete theory. Many *Beyond the Standard Model* (**BSM**) theories arose as proposed extensions to SM with solutions to one or more of the above open questions, as well as attempting to unify all of the different interactions into one complete theory.

1.3 Beyond the Standard Model

The phrase "BSM Physics" covers a wide range of theories, as well as experimental observations that cannot be explained by the SM, including gravity. On the theoretical side it can represent any extensions to the SM, regardless of whether it includes any proposed solutions to the unresolved questions left by the SM. It can also refer to any deeper explanations on observations that SM already accommodates, but only with ad hoc parametrizations such as the Yukawa couplings.

While the "theoretical space" that these BSM theories have created for new particles and new interactions is very vast, signatures of new physics from some of these models are at the TeV scale range, which is achievable in the current generation of particle colliding experiments.

1.3.1 Supersymmetry

Supersymmetry (**SUSY**) [21] is a very popular concept that many proposed theories are built on, as an extension of the Standard Model. It suggests the existence of individual super-partners (sparticles) for all particles in SM, where they differ by a half-integer in spin from the respective original SM particle. These super-partners are predicted to have the same mass as their SM partners in theories with unbroken supersymmetry, however none of these have been seen in experiments with their SM partners, as they should if they exist. This implies that if the SM particles all have a respective supersymmetric super-partner, they must be much heavier compared to the SM particle as predicted by theories with spontaneously broken supersymmetry, potentially at the TeV scale.

SUSY models in general contain explanations for matter/antimatter asymmetries with extra CP-violation processes. Contributions from the fermionic super-partners also prevents quadratic divergences on the Higgs boson mass. They also predict the unification of the electroweak and strong gauge couplings at high energies.

While there are many currently existing supersymmetric models, the "Minimal Supersymmetric Standard Model" (**MSSM**) [22] is one of the best studied candidates. It includes only a minimal number of extra particles to extend SM with supersymmetry, while also proposing solutions to the SM open questions in similar ways as all other non-minimal SUSY theories. The MSSM contains a new quantum number called R-parity, where:

$$R = (-1)^{3B+2S+L} \tag{1.1}$$

with B, L and S here denote respectively the baryon number, lepton number and the spin quantum number. This definition of R gives the discrete symmetry between SM and SUSY particles, by yielding $R = +1$ for SM particles and $R =$

-1 for SUSY particles. In versions of MSSM where this quantity is conserved, the Lightest SUSY Particle (**LSP**) in the model is predicted to be stable. The LSP of MSSM is considered one of the most probable candidates for dark matter. [23]

1.3.2 Grand Unified Theories

Grand Unified Theories (**GUT**) [24] denote a class of BSM theories that attempt to unify the strong and electroweak interactions at high energies. This unification of gauge couplings implies that these interactions are subsets of the same gauge symmetry at a larger scale, where there exist only one interaction with one universal gauge coupling. The breaking of this larger gauge symmetry is predicted to be at the energy scale of 10^{16} GeV (also commonly known as the "GUT Scale").

This proposal of a larger underlying universal symmetry naturally predicts the quantized nature of electromagnetic charges in SM, as well as the relative strengths of the currently observed fundamental interactions. This idea of a larger underlying symmetry that is broken at lower energies is also present in SUSY, hence it is worth noting that GUT and SUSY are not mutually exclusive from each other.

Direct observations of some massive particles that are predicted in GUT theories are beyond the reach of foreseeable particle colliding experiments. Observations of proton decay, neutrinos properties as well as electric dipole moments of SM particles may be used as indirect probes to the presence of such particles.

1.4 Phenomenology of Leptoquarks

The quarks and leptons despite being a representation of fields that are independent of each other, unexplained symmetries can be interpreted between their generation structure. An important indication is the cancellation of the quarks' and leptons' contribution to the triangle anomalies of gauged currents, which are

key contributions to the renormalization and consistency of SM [25]. This remarkable balance between the contributions from leptons and quarks implies that these two particle types are part of a symmetry in a more fundamental theory.

Leptoquarks (LQ) are proposed particles that are responsible for the related interactions between leptons and quarks. They are colour-triplet gauge bosons and carry fractional electric charge, as well as both lepton and baryon numbers [26]. They can be either scalar or vector bosons, and they are expected to couple directly to lepton-quark pairs, as shown in Figure 1.1. The coupling strength between scalar LQs and the lepton-quark pair depend on a single Yukawa coupling λ_{LQ-l-q}, while the additional magnetic moment and electric quadrupole moment interactions of vector LQs lead to their coupling strength with lepton-quark pairs being governed by two couplings, κ_G and λ_G [27, 7]. These respective coupling constants for scalar and vector LQs, as well as the branching ratio β into different leptons and quarks are model dependent.

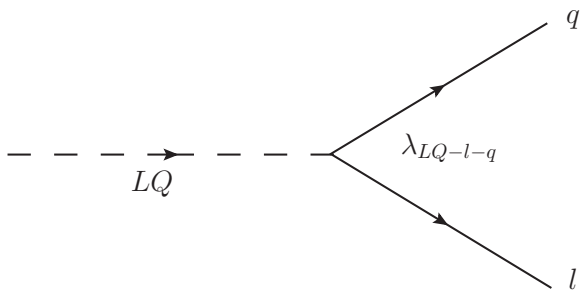

FIGURE 1.1: Feynman diagrams showing the Yukawa coupling λ_{LQ-l-q} between a leptoquark, a lepton and a quark.

In many extensions of the SM such as GUT, E_6 and Technicolor, where leptons and quarks are attempted to be unified under a common framework, interactions between them arise naturally. The GUT-inspired Pati-Salam SU(4) model [28] describes quarks with four colours, with the first three representing the three colours from the SM strong interaction, the forth colour would fulfil the role of lepton number L in the model. This assumes the leptons and quarks are in fact the

same particle in different eigenstates, and LQs are responsible for the interactions between the forth colour and the first three. E_6 is a gauge symmetry group that is present in some of the superstring inspired GUT theories, where it can also break into the SM gauge group [29]. Such theories predict a large number of additional particles and gauge bosons to SM, representing many new interactions including lepton-quark interactions, mediated by LQs.

BSM theories based on the concept of new gauge group called Technicolor [30] introduces new massless fermions (technifermions), assume that the mass for EW gauge bosons in the SM are generated by the condensates of these technifermions after symmetry breaking, without the need of the Higgs mechanism. Related new strong-gauge interactions are asymptotically free at high energies and confined (unobservable) at low energies. The dynamics of chiralities connecting the SM fermions and technifermions generates mass for SM fermions in the extended schemes. Technipions that are composed of technifermions, analogous to SM pions in the strong interaction, takes up the role of LQs in this model.

1.5 The Effective mBRW Model

An effective model developed by Buchmüller, Rückl and Wyler was designed with a model independent approach for searches of LQs at collider experiments [31]. Leptoquarks in this model are required to have interactions that are renormalizable, as well as invariant under SM gauge symmetry group $SU(3)_C \otimes SU(2)_L \otimes U(1)_Y$. They are also required to couple only to SM particles, and are required to conserve lepton and baryon numbers independently to be consistent with the experimentally observed proton stability [32]. Further low energy constraints are imposed in the *minimal* BRW model, where the LQs have pure chiral couplings to SM quarks [33], as well as coupling only to a single quark and a single lepton generation, in order to be consistent with the observed suppression on Flavour Changing Neutral Currents (**FCNC**) from experimental results. This suggests LQs exists in three

generations, LQ_1, LQ_2 and LQ_3, each relating to the generation of lepton that they couple with. This following effective Lagrangian summarizes these imposed constraints on the interaction of LQs:

$$\mathcal{L} = \mathcal{L}_{|F|=0} + \mathcal{L}_{|F|=2} \tag{1.2}$$

where $\mathcal{L}_{|F|=0,2}$ denote the lagrangian responsible for respective interactions of LQs with fermion number $F = 3B + L$, with B and L denoting baryon and lepton number respectively. $\mathcal{L}_{|F|=0,2}$ respectively has the flavour diagonal form:

$$\begin{aligned}\mathcal{L}_{|F|=0} = &(h_{2L}\bar{u}_R\ell_L)R_2 + \tilde{h}_{2L}\bar{d}_R\ell_L\tilde{R}_2 \\ &+ (h_{1L}\bar{q}_L\gamma^\mu\ell_L)U_{1\mu} \\ &+ \tilde{h}_{1R}\bar{u}_R\gamma^\mu e_R\widetilde{U}_{1\mu} + h_{3L}\bar{q}_L\tau\gamma^\mu\ell_L U_{3\mu} + c.c.\end{aligned} \tag{1.3}$$

$$\begin{aligned}\mathcal{L}_{|F|=2} = &(g_{1L}\bar{q}^c_L i\tau_2\ell_L + g_{1R}\bar{u}^c_R e_R)S_1 \\ &+ \tilde{g}_{1R}\bar{d}^c_R e_R\widetilde{S}_1 + g_{3L}\bar{q}^c_L i\tau_2\tau\ell_L S_3 \\ &+ (g_{2L}\bar{d}^c_R\gamma^\mu\ell_L + g_{2R}\bar{q}^c_L\gamma^\mu e_R)V_{2\mu} \\ &+ \tilde{g}_{2L}\bar{u}^c_R\gamma^\mu\ell_L\widetilde{V}_{2\mu} + c.c.\end{aligned} \tag{1.4}$$

for the LQ_1 case. where q_L and ℓ_L represent left-handed quark and lepton doublets respectively, e_R, d_R and u_R are the right-handed electron, down and up quark. The charge-conjugated fermion field is represented by $\psi^c = C\bar{\psi}^T$. For the $|F| = 0$ case, R_2, $\widetilde{R}_2$ and $\widetilde{U}_{1\mu}$, $U_{1\mu}$, $U_{3\mu}$ are respectively the scalar (spin = 0) and vector (spin = 1) LQ fields, while S_1, $\widetilde{S}_1$ S_3 and $V_{2\mu}$, $\widetilde{V}_{2\mu}$ are respectively the scalar and vector LQ fields for the $|F| = 2$ case. Yukawa-type couplings between leptons and quarks with LQ for the $|F| = 0$ case are denoted by $h_{2(L,R)}$, $\tilde{h}_{2L}$ and $h_{1(L,R)}$, $\tilde{h}_{1R}$, h_{3L} respectively for the scalar and vector LQs, while $g_{1(L,R)}$, $\tilde{g}_{1R}$, g_{3L} and $g_{2(L,R)}$, g_{2L} are respectively the couplings for scalar and vector LQs for the $|F| = 2$ case. The properties of these different LQs are listed in Table 1.4. Global substitution in

this lagrangian for the corresponding second and third generation fermions in the place of first generation fermions gives the lagrangian form for LQ_2 and LQ_3.

Leptoquark	Spin	$F = 3B + L$	$SU(3)_C$	$SU(2)_L$	$U(1)_Y$
R_2	0	0	3	2	$\frac{7}{6}$
$\widetilde{R}_2$	0	0	3	2	$\frac{1}{6}$
U_1	1	0	3	1	$\frac{2}{3}$
$\widetilde{U}_1$	1	0	3	1	$\frac{5}{3}$
U_3	1	0	3	3	$\frac{2}{3}$
S_1	0	-2	$\bar{3}$	1	$\frac{1}{3}$
$\widetilde{S}_1$	0	-2	$\bar{3}$	1	$\frac{4}{3}$
S_3	0	-2	$\bar{3}$	3	$\frac{1}{3}$
V_2	1	-2	$\bar{3}$	2	$\frac{5}{6}$
$\widetilde{V}_2$	1	-2	$\bar{3}$	2	$-\frac{1}{6}$

TABLE 1.4: Scalar and Vector Leptoquarks in the mBRW model and their associated quantum numbers [31].

1.6 Experimental Achievements to date

Direct searches for LQs at particle collider experiments have been common, as it is one of the many signatures of BSM physics. New particle colliders with higher and higher centre of mass collision energy ($\sqrt{s}$) have been built over the years, expanding the LQ mass range where the searches can probe. No presence of LQs have been observed to date, and the accumulation of these experimental achievements create bounds on the production cross section and mass of leptoquarks.

1.6.1 Pre-LHC Experimental Achievements

Searches for Leptoquarks at the H1 experiment of HERA, an Electron-Proton (ep) collider with collision energy of $\sqrt{s}$ = 319 GeV, have been performed with their entire set of collected data which is equivalent to the integrated luminosity of $\mathscr{L}_{int}$ = 446 fb^{-1}. Electron-Proton colliders naturally provides a much higher sensitivity for the single production of 1st generation leptoquarks. With the assumption on the value of the electromagnetic strength at $\lambda = 0.3$, LQ_1s were excluded with 95% confidence level with $M_{LQ} < 800$ GeV [34]. Searches LQ_2 and LQ_3 via lepton flavour-violating processes were also carried out, with the same assumption of $\lambda = 0.3$. Exclusion limits at 95% confidence level were obtained at $M_{LQ} \leq 712$ GeV and $M_{LQ} \leq 419$ GeV, respectively for LQ_2 and LQ_3 [35].

The **CDF** and **D**Ø experiments at Tevatron, a $p\bar{p}$ collider with collision energy of $\sqrt{s}$ = 1.96 TeV, were good platforms to search for pair-produced LQs. There were efforts at **CDF** on the searches for LQ_1 with $\mathscr{L}_{int}$ = 110 pb^{-1} [36] and LQ_2 with $\mathscr{L}_{int}$ = 198 pb^{-1}, and at **D**Ø for LQ_1 with $\mathscr{L}_{int}$ = 5.4 fb^{-1} [37], LQ_2 with $\mathscr{L}_{int}$ = 1.0 fb^{-1} [38], and LQ_3 with $\mathscr{L}_{int}$ = 5.2 fb^{-1} [39]. The LQ_2 result from the **D**Ø experiment for both $\mu\mu qq$[2] and $\mu\nu qq$ final states, are the most relevant to the main work of this thesis. Mass of second generation LQ $M_{LQ} < 316(270)$ GeV were excluded with 95% C.L. at $\beta = 1(0.5)$ (See Figure 1.2).

1.6.2 Leptoquark searches at LHC

Searches for LQs have been carried out at the ATLAS (LQ_1 [40] and LQ_2 [41] with $\mathscr{L}_{int}$ = 1.0 fb^{-1}, and LQ_3 [42] with $\mathscr{L}_{int}$ = 4.7 fb^{-1}) and CMS (LQ_1 and LQ_2 [43] with $\mathscr{L}_{int}$ = 5.0 fb^{-1}, and LQ_3 [44, 45] with $\mathscr{L}_{int}$ = 1.0 fb^{-1}) experiments of the Large Hadron Collider (**LHC**, a pp collider) with collision energy at $\sqrt{s}$ = 7 TeV. The search for LQ_2 at $\sqrt{s}$ = 7 TeV with the ATLAS detector was concluded with

[2]Final states containing quarks (q) appear as hadronic jets in collider experiments, hence they are also commonly denoted with j.

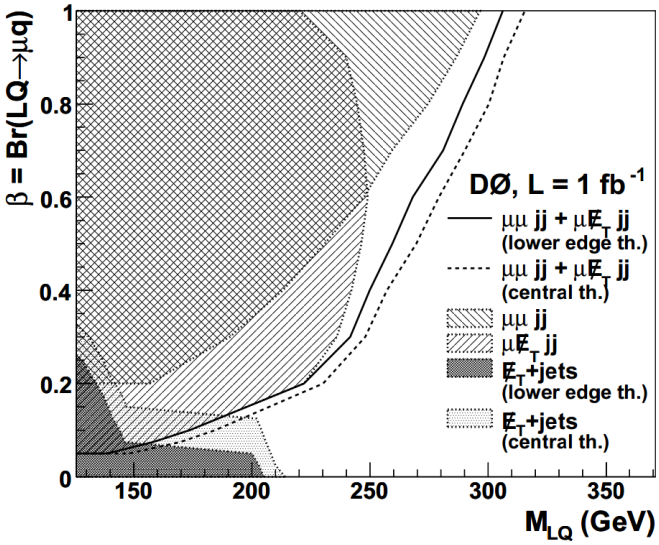

FIGURE 1.2: Results of the LQ searches in the $\mu\mu jj$ ($\beta = 1$) and $\mu\nu jj$ ($\beta = 0.5$) final states from the **D**Ø experiment with $L_{int} = 1.0$ fb^{-1} at $\sqrt{s} = 1.96$ TeV. The exclusion regions observed in the β - M_{LQ} plane with 95% C.L. for both decay channels are independently shown, as well as their combination.

an exclusion limit of $M_{LQ} < 685$ GeV was excluded with 95% confidence level, as shown in Figure 1.3. Relevant techniques and strategies developed from this search for LQ_2 with $\sqrt{s} = 7$ TeV data were carried over to the search with $\sqrt{s} = 8$ TeV data, with changes that are appropriate for the higher collision energy. The analysis presented from Chapter 5 onwards is dedicated to the search on second generation LQs decaying to $\mu\mu qq$ final state at $\sqrt{s} = 8$ TeV, which includes the application of such refined techniques and strategies.

Both single or paired production of LQs can occur in hadron-hadron collisions. Pair production of LQs as shown in Figure 1.4 are almost independent of λ_{LQ-l-q}, as they are produced through either gluon fusion or quark-antiquark annihilation processes. Single production of LQs on the other hand occur in association with a lepton depends on the unknown Yukawa coupling λ_{LQ-l-q} that is model dependent, as shown in Figure 1.5. The pair production of LQs therefore depend almost entirely on the strong coupling α_s [27], as the production cross section from t-

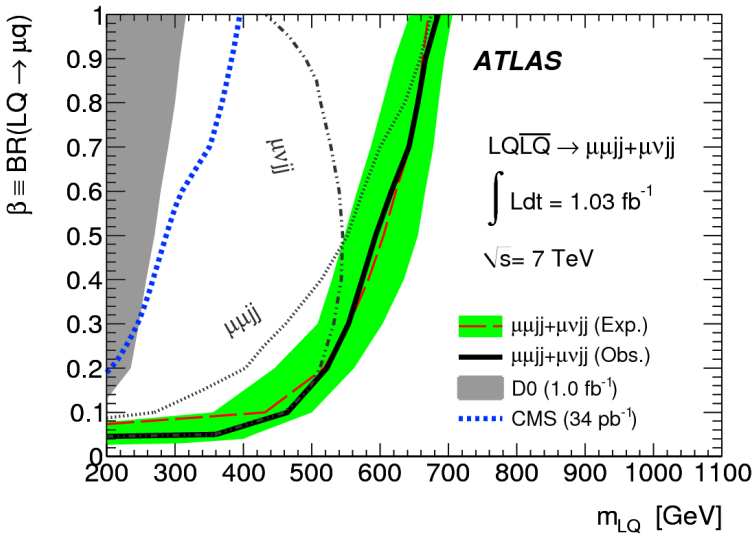

FIGURE 1.3: Results of the LQ searches in the $\mu\mu jj$ ($\beta = 1$) and $\mu\nu jj$ ($\beta = 0.5$) final states from the ATLAS experiment with $\mathscr{L}_{int} = 1.0$ fb^{-1} at $\sqrt{s} = 7$ TeV. The exclusion regions observed in the β - M_{LQ} plane with 95% C.L. for both decay channels are independently shown, as well as their combination.

channel lepton exchange are proportional to λ^2_{LQ-l-q}, which is negligible in this case. The analysis presented in this thesis will only consider the pair production process for its relative model independence.

As discussed earlier in Section 1.4 that the coupling strength between scalar LQs and lepton-quark pairs depend only on a single Yukawa coupling λ_{LQ-l-q}, while the equivalent coupling strength for vector LQs are governed by two couplings, κ_G and λ_G, due to the extra magnetic moment and electric dipole moment interactions of vector LQs. These couplings for vector LQs are model dependent, and their variation between different models can yield cross section values that differ by one to two orders of magnitude. Although the resulting coupling strength for both types of LQs and their decay rates are unknown, the analysis presented in this thesis will only consider scalar leptoquark decays due to its relative model independence.

Calculations for the LO production cross sections for pair-produced scalar LQs

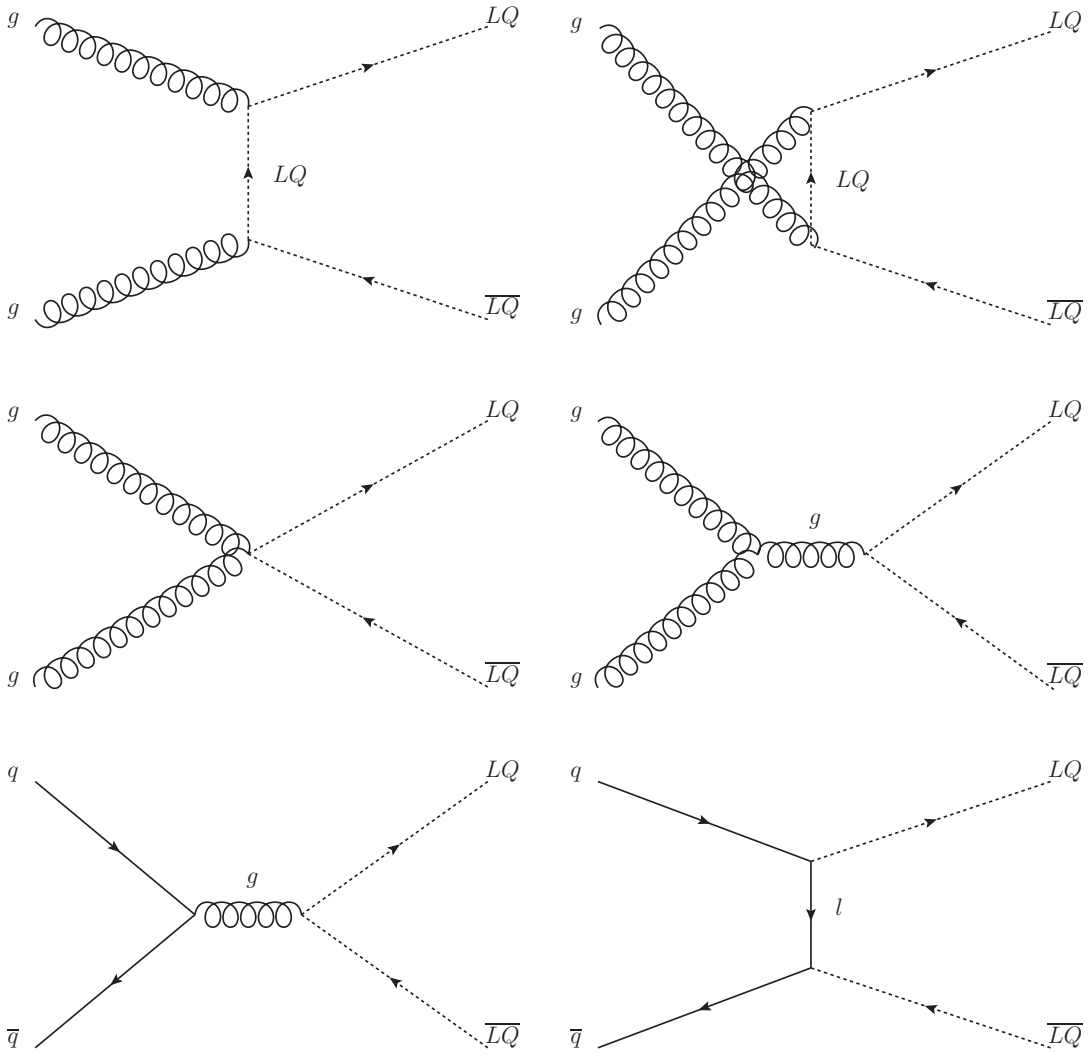

FIGURE 1.4: Leading order Feynman Diagrams representing LQ pair-production from gluon-gluon fusion and quark-antiquark annihilation.

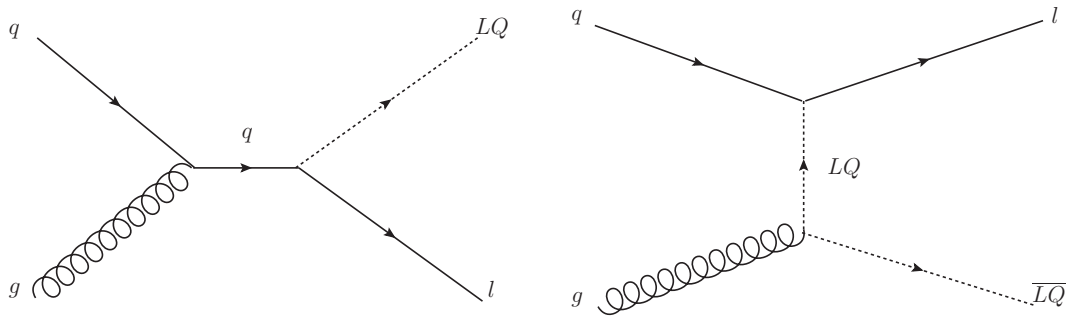

FIGURE 1.5: Leading order Feynman Diagrams representing single LQ production with an associated lepton.

at the LHC has been performed by Krämer et al [46]. The two primary production processes, gluon fusion and quark-antiquark annihilation, are respectively predicted by:

$$\hat{\sigma}_{gg}^{LO} = \frac{\alpha_s^2 \pi}{96\hat{s}} \Big[\beta\big(41 - 31\beta^2\big) + \big(18\beta^2 - \beta^4 - 17\big) \log \frac{1+\beta}{1-\beta} \Big] \tag{1.5}$$

$$\hat{\sigma}_{q\bar{q}}^{LO} = \frac{\alpha_s^2 \pi}{\hat{s}} \frac{2}{27} \beta^3 \tag{1.6}$$

where $\beta = \big(1 - \frac{4M_{LQ}^2}{\hat{s}}\big)^{\frac{1}{2}}$ denotes the velocity of the LQ, with $\hat{s}$ being the collision energy squared. Production at low LQ mass values are dominated by the gluon fusion mechanism, while the contribution from quark-antiquark annihilation becomes significant at higher LQ mass values, up to 30% at $M_{LQ} = 1.5$ TeV. QCD radiative corrections can strongly affect the parton cross sections around the production threshold, and can be expressed as:

$$\sigma\big[pp \to LQ + \overline{LQ}\big] = \sigma_{gg} + \sigma_{gq} + \sigma_{q\bar{q}} \tag{1.7}$$

which include virtual corrections, gluon bremsstrahlung as well as contributions from quark-gluon collisions. The perturbative expansion of the total partonic

production cross section can be written as:

$$\hat{\sigma}_{ij} = \frac{\alpha_s^2(M_{LQ}^2)}{M_{LQ}^2}\Big\{f_{ij}^B(\beta) + 4\pi\alpha_s(M_{LQ}^2)\Big[f_{ij}^{V+S}(\beta) + f_{ij}^H(\beta)\Big]\Big\} \tag{1.8}$$

where i, j denotes g, q, while f^B and $f^{V+S,H}$ respectively represents the Born cross section term for parton subprocesses, and the virtual+soft and hard gluon corrections. These scaling functions have dependence on $\sqrt{\hat{s}}$ through β, and can be expressed as follows near the productions threshold with $\beta \ll 1$:

$$f_{gg}^B = \frac{7\pi\beta}{384} \qquad f_{q\bar{q}}^B = \frac{\pi\beta^3}{54}$$

$$f_{gg}^{V+S} = f_{gg}^B\Big[\frac{11}{336\beta}\Big] \qquad f_{q\bar{q}}^{V+S} = -f_{q\bar{q}}^B\Big[\frac{1}{48\beta}\Big] \tag{1.9}$$

$$f_{gg}^H = f_{gg}^B\Big[\frac{3}{2\pi^2}\log^2(8\beta^2) - \frac{183}{28\pi^2}\log^2(8\beta^2)\Big] \quad f_{q\bar{q}}^{V+S} = f_{q\bar{q}}^B\Big[\frac{2}{3\pi^2}\log^2(8\beta^2) - \frac{107}{36\pi^2}\log^2(8\beta^2)\Big]$$

by choosing M_{LQ} as the renormalization and factorization scale. The dependence of these functions on the scale reduces greatly when these next-to-leading order (**NLO**) terms are included, which in turn enhances the production of Leptoquarks. Figure 1.6 displays the corresponding NLO values for $\sqrt{s} = 8$ TeV at the LHC.

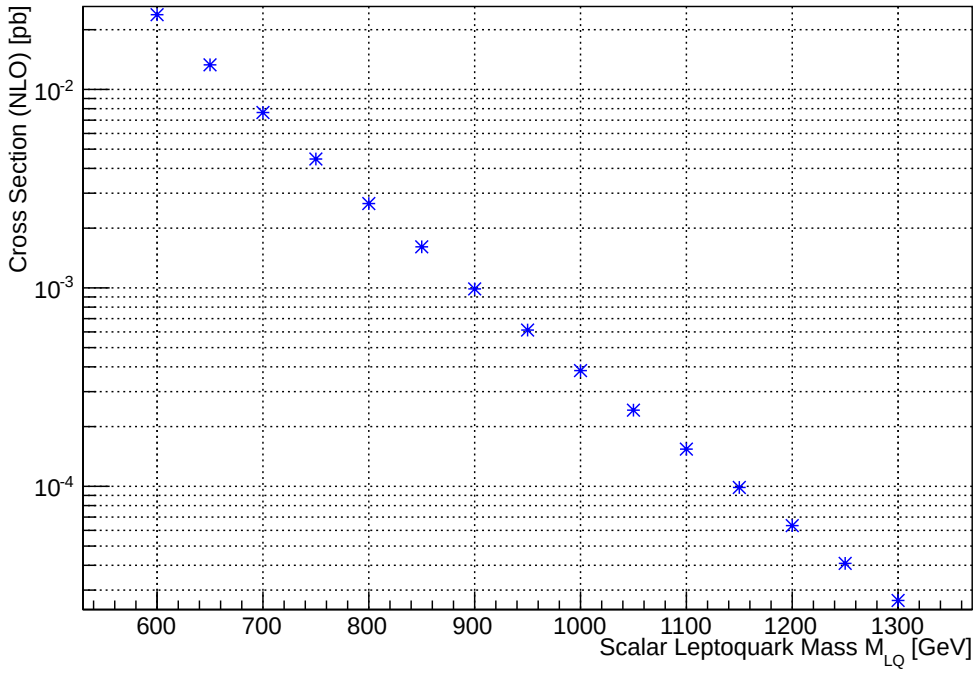

FIGURE 1.6: NLO Cross sections for pair production of scalar Leptoquarks at pp collisions with center of mass energy of $\sqrt{s} = 8$ TeV, as a function of Leptoquark mass M_{LQ} [46].

Chapter 2

ATLAS at the LHC

High energy collisions of subatomic particles have been a major advancing direction for the field of Experimental Particle Physics. Studies of unstable particles with high masses as well as particle interactions at shorter ranges can gradually be achieved by continually increasing the Centre of Mass (**CM**) energy of particle collisions. This expansion of energy range that particle physicists can experimentally probe permits the observation of potential new BSM physics that exist only in environments at higher energies. The Large Hadron Collider [47] operated by the European Organization of Nuclear Research (**CERN**, historical reasons for this special abbreviation) [48] is currently the particle accelerator with the highest CM collision energy in the world. It is located in a circular tunnel approximately 27 kilometres long, 100 metres underground on average, crossing the French-Swiss boarder near Geneva, Switzerland. It is designed to primarily collide protons at CM energy of $\sqrt{s} = 14$ TeV with an instantaneous luminosity of $\mathscr{L} = 10^{34}\text{cm}^{-2}\text{s}^{-1}$, at its peak performance. It is also capable to collide heavy lead ions in dedicated periods with CM energy up to $\sqrt{s} = 5.5$ TeV per nucleon pair at $\mathscr{L} = 10^{27}\text{cm}^{-2}\text{s}^{-1}$. The LHC began its operation on 10th September 2008, however a magnetic quench occurred [49] after a mere 9 days since the circulation of the first proton beam [50], causing severe damage to the infrastructure. Operation began again in November 2009 over a 26 day testing period with only 1.18 TeV per proton beam circulating the LHC, as a precautionary measure. First proton-proton collisions at $\sqrt{s} = 7$ TeV came on 10th March 2010, for which this CM energy were maintained for the rest of 2010 data taking periods. Further upgrades were planned along with gradual increase of beam energy, to ensure the safety of components at maximum LHC energy eventually by 2015.

2.1 Production of pp collisions

Collision of particles at high energies provide windows where potential BSM physics can be probed. CERN has been a platform for collaboration of physicists around the world for many years, where their efforts are combined to push particle collisions to higher energies in the search of new physics, as well as better understanding of our current knowledge. Colliding protons with the LHC is possible from the accumulation of technological efforts from past experiments at CERN, for which many of them have been upgraded to support the operation of the LHC.

2.1.1 The CERN Accelerator Complex

Connected to the LHC are a chain of smaller machines and particle accelerators, as shown in Figure 2.1. They are responsible for producing proton beams, as well as accelerating them at successive stages before the injection into the LHC. Protons are initially produced in a hot plasma inside a machine called Duoplasmatron [51], where electrons are detached from hydrogen molecules, leaving the proton to be injected into Linac2 for acceleration to 50 MeV. The protons are then accelerated to 1.4 GeV by the Proton Synchrotron Booster (**PSB**), before being accelerated further by the Proton Synchrotron (**PS**) to 25 GeV. The Super Proton Synchrotron (**SPS**) then accelerates the protons to 450 GeV, before finally injecting the protons into the LHC ring for the last phase of acceleration up to the required collision energy [52].

2.1.2 Large Hadron Collider

The LHC is designed to control two particle beams, of either protons or heavy lead ions, to stay in circulation around the machine. The two beams circulate in opposite directions in separate beam pipes. The proton beam used for physics

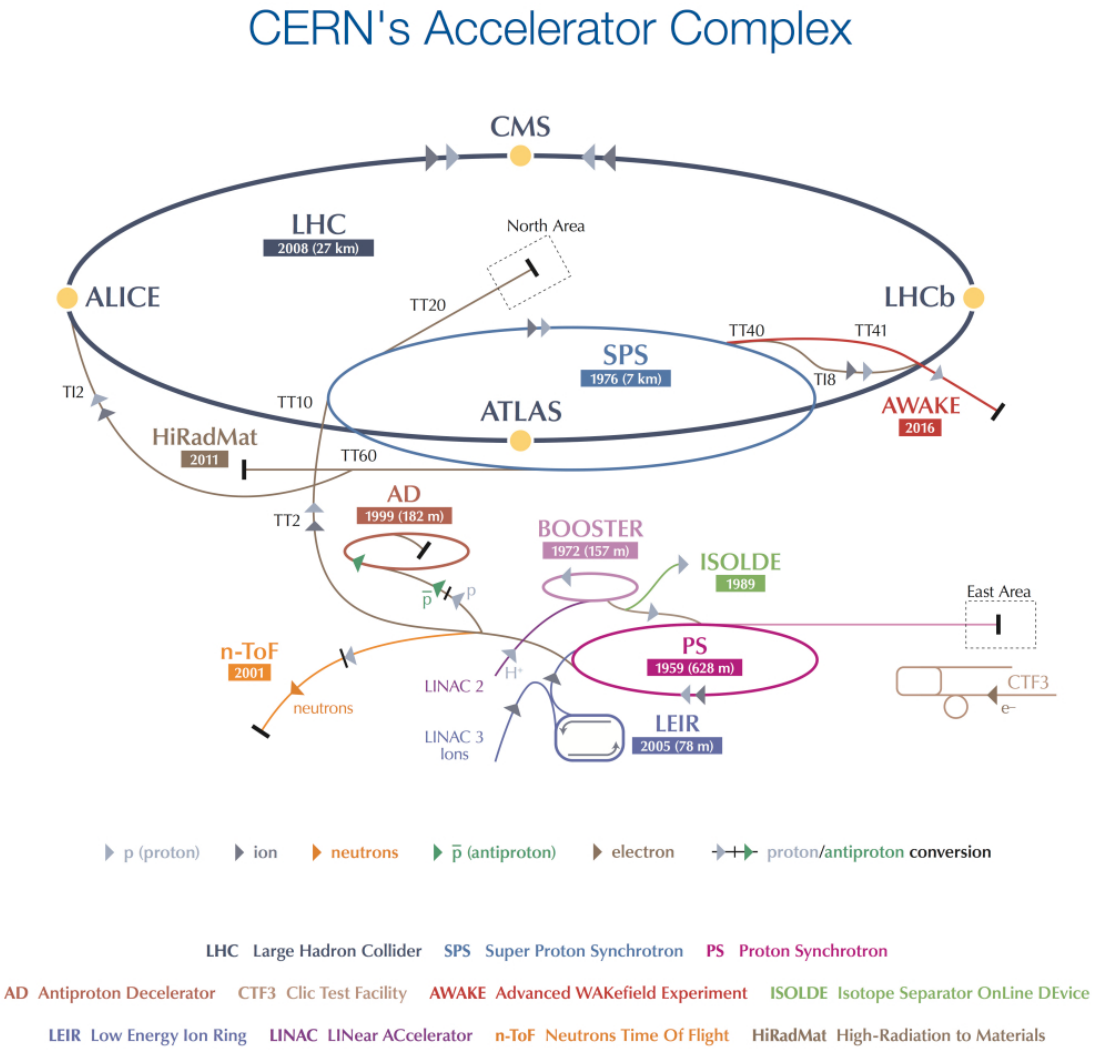

FIGURE 2.1: CERN Accelerator Complex (Not to Scale) © CERN 2013

analysis in the LHC are structured in bunches separated typically with 50[1] ns gaps, containing approximately 1.15×10^{11} protons per bunch [54]. Gaps bigger than 25 ns are also created in the bunch pattern to allow safe beam dumping, leaving 1380[2] bunches per LHC ring out of the possible 3564 bunch positions. This bunch structure of the proton beams, along with its acceleration up to collision energy is achieved by Radio Frequency (**RF**) cavities. The RF cavities are also responsible for maintaining the accelerated beam at collision energy, as well as keeping the proton much tightly together.

The two counter circulating beams are guided around in high vacuum tubes by 1232 dipole magnets operating below 2 Kelvin, and 392 quadruple magnets are installed to further focus the beams. The proton beams cross at four *interaction points* (**IPs**, numbered according to their respective octant number) as shown in Figure 2.2, with each of these surrounded by a detector: ATLAS (IP1) [55] and CMS (IP5) [56] are sets of detectors independently designed from each other, with the same goal of achieving high sensitivity in a wide range of physics, while ALICE (IP2) [57] and LHCb (IP8) [58] are designed to focus specifically on the study of quark-gluon plasma and b-physics, respectively. Further details on the LHC's specifications can be found in [59].

Luminosity $\mathscr{L}$ is a quantity used to measure the ability of a particle collider such as the LHC, to produce events. The rate of events produced, $\frac{d\mathscr{N}}{dt}$ is given by:

$$\frac{d\mathscr{N}}{dt} = \mathscr{L} \times \sigma \tag{2.1}$$

where σ is the production cross section of the observed event. For head on collisions of unequal Gaussian bunched beams, the luminosity is determined by:

[1] 25 ns by design, 50 ns was used from June 2012 [53].
[2] 2808 by design.

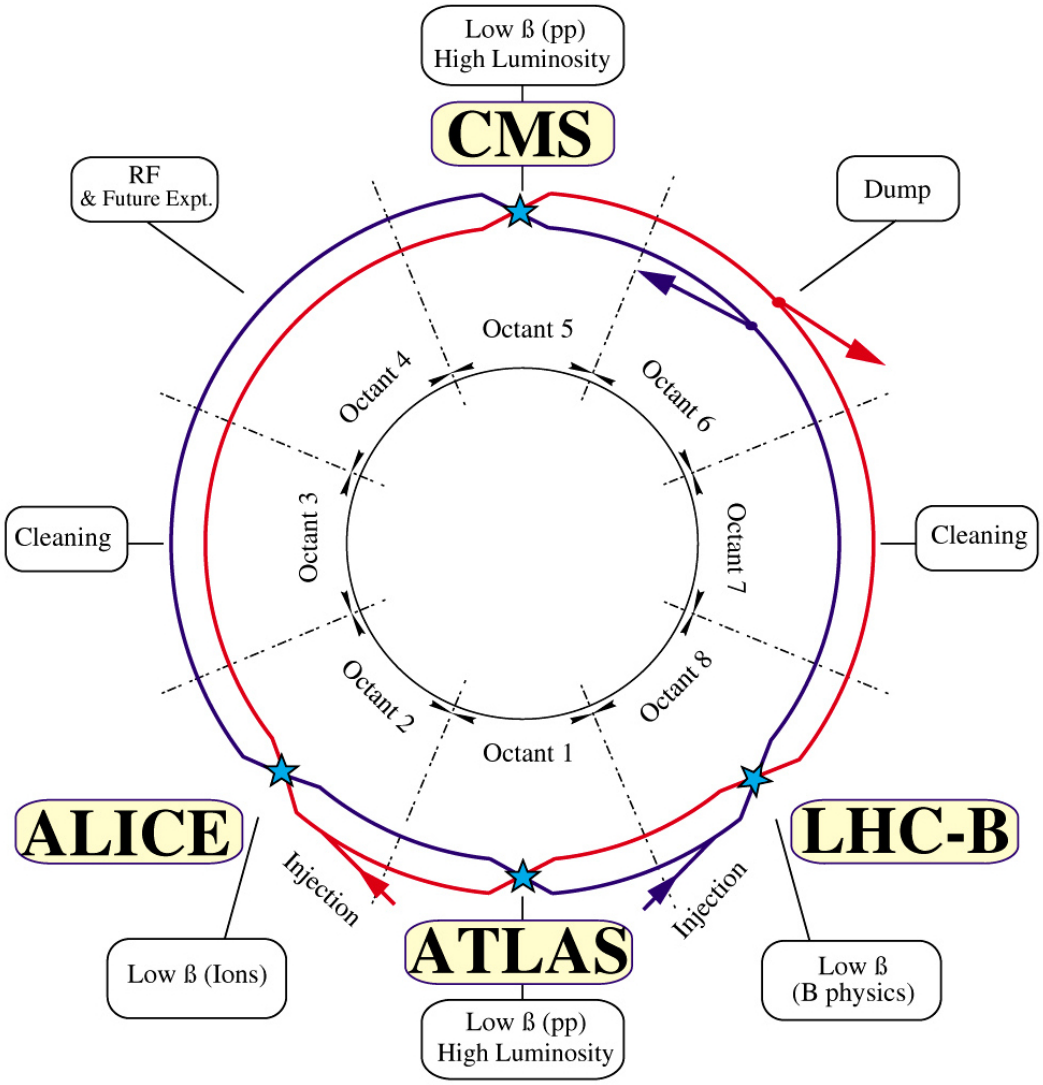

FIGURE 2.2: Schematic layout of the LHC showing the four experiments at their interaction points. The amplitude function β is a measure of how tightly squeezed the particle beam is, and this is typically kept as low as possible by quadruple magnets at interaction points. [60] (Not to Scale) © CERN 1997

$$\mathscr{L} = \frac{\mathcal{N}_1 \mathcal{N}_2 \mathcal{N}_b f}{2\pi\sqrt{\sigma_{1x}^2 + \sigma_{2x}^2}\sqrt{\sigma_{1y}^2 + \sigma_{2y}^2}} F \tag{2.2}$$

where $\mathcal{N}_1$ and $\mathcal{N}_2$ are the intensities[3] of the two bunches, $\mathcal{N}_b$ is the number of colliding bunches and f is the circulating frequency. A factor accounting for geometrical effects such as the non-zero crossing angles of the beams are represented by F, while σ_{1x}, σ_{1y}, σ_{1y} and σ_{2y} represent the beam profiles in the x and y transverse directions at the interaction point. A more detail description of how the luminosity is determined for the LHC can be found in [61] and [62].

During the 2012 pp run the LHC has delivered an integrated luminosity of $\mathscr{L}_{int}$ = 22.2 fb^{-1} with a peak luminosity of $\mathscr{L}$ = 7.73×10^{33}cm^{-2}s^{-1}, while ATLAS recorded $\mathscr{L}_{int}$ = 21.3 fb^{-1} in total under stable beam and good detector conditions for physics analysis. These are shown in Figure 2.3 for the entire 2012 pp run.

2.2 The ATLAS Detector

ATLAS (acronym for **A** **T**oroidal **L**HC **A**pparatu**S**) is a detector that is built around one of the interaction points in the LHC ring, for observing head-on collisions of protons as closely as technologically possible[4]. It is designed to be sensitive in the widest possible range of potential new physics, as well as a platform to extend the understanding of our current knowledge. ATLAS is also the name of the collaboration, consisting more than 3000 scientists from 174 institutions in 38 countries.

Figure 2.4 shows the internal structure of the ATLAS detector. It is cylindrically shaped containing many geometrical symmetries, with its central axis aligned with

[3]Measured in No. of protons per bunch (**ppb**).

[4]Information used in this section for the description of various components of the ATLAS detector are based on the ATLAS Technical Design Report [64], unless otherwise stated.

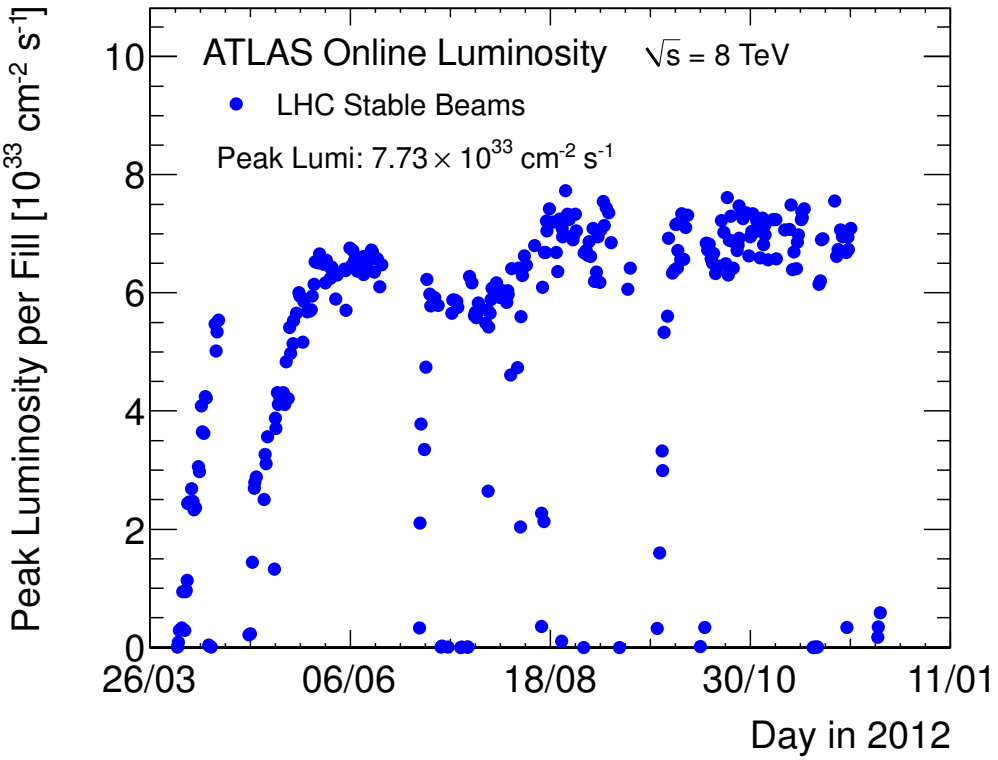

(A)

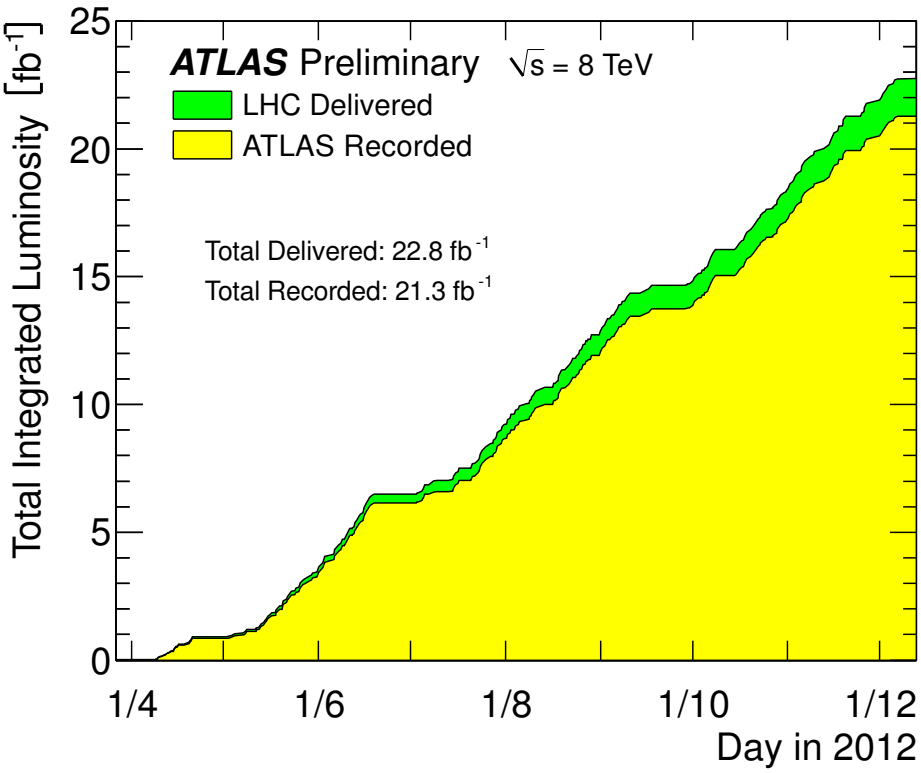

(B)

FIGURE 2.3: Instantaneous (2.3a) and total integrated luminosity (2.3b) delivered by the LHC and recorded by ATLAS over the entire 2012 pp run with CM energy $\sqrt{s} = 8$ TeV. [63]

the direction of the circulating beams. ATLAS is approximately 25 meters in diameter, 46 metres in length and weighs about 7000 tonnes. It is designed with an concentric onion shell structure, surrounding the circulating beams and centred at the IP. Several components described in Section 2.2.2 are installed in different parts of the detector to create magnetic fields for the study of charged particles. The Inner Detector (**ID**) described in Section 2.2.3 that is embedded immediately inside the Central Solenoid Magnet (**CSM**) surrounds the IP in the inner most layer, this combination provide momentum measurements of charged particles [65]. The Electromagnetic Calorimeters (**ECAL**) and the Hadronic Calorimeters (**HCAL**) described in Section 2.2.4 are the next outer layers, responsible for measuring the energy carried by corresponding particles. The Muon Spectrometer (**MS**) that is described in Section 2.2.5 sits on the outer most layer, for measuring out going muons that can penetrate through the ID and calorimeters more easily compared to other particles. Forward Detectors described in 2.2.6 are installed beyond the endcap regions from the collision point to measure elastic scattering at very forward angles, primarily for more accurate measurements on beam luminosities.

2.2.1 Co-ordinate System

ATLAS has established a Cartesian coordinate system centred around the nominal IP to maintain consistency on the view of the collisions from different detector systems [66]. The positive X axis points toward the centre of the LHC ring, while the positive Y axis points upwards (radially outwards from the centre of the Earth). The positive Z axis is aligned with the beam, pointing in the counter-clockwise direction of the LHC ring as view from above. The X-Y plane that is orthogonal to the beam/Z axis is used to calculate transverse quantities for momentum (p_T), energy (E_T) and other similar important variables, where potential interesting physics would be shown. The azimuthal angle ϕ is also defined in this transverse plane, where $\phi = 0$ points along the positive X axis. The scattering angle θ is measured from the Z axis, however an equivalent quantity called *psuedorapidity*

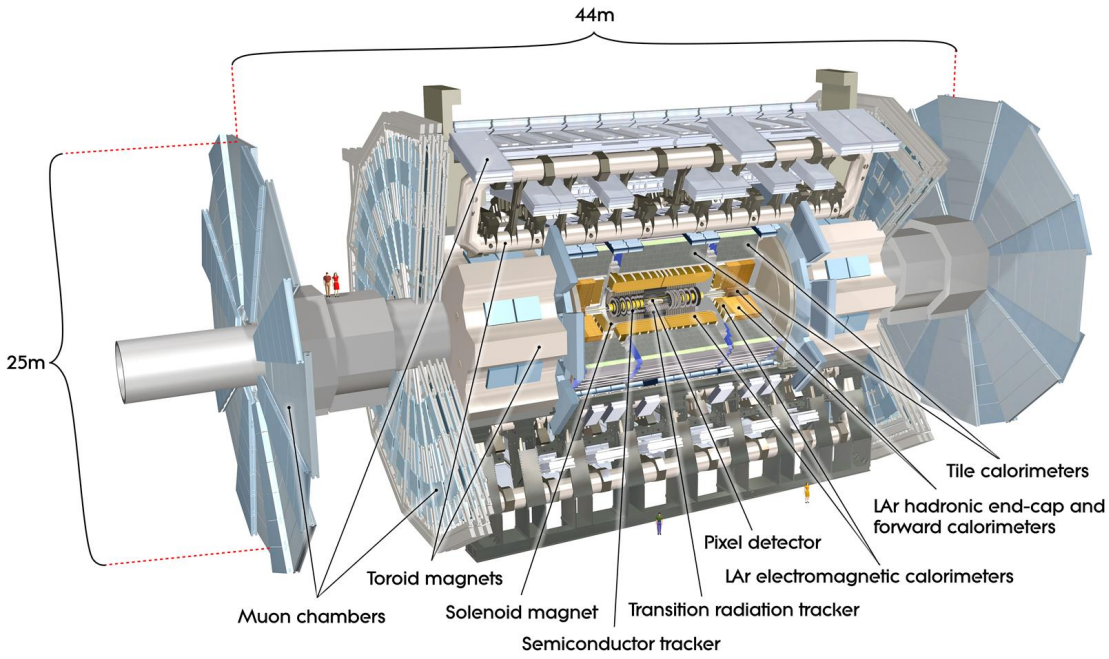

FIGURE 2.4: A cut-open view of the ATLAS detector showing its various components. Two avatars of average human size are put near the centre left for size comparison, © CERN 2013.

$\eta = -\ln[\frac{tan(\theta)}{2}]$ is more commonly used. Distances between particles and hadronic jets resulting from the pp collisions are usually quantified in the $\eta - \phi$ space with ΔR defined as $\Delta R = \sqrt{(\Delta\eta)^2 + (\Delta\phi)^2}$.

2.2.2 Magnet System

The ATLAS detector contains a superconducting magnet system to allow momentum measurements of charge particles, by creating magnetic fields that induce curvatures on their outgoing trajectories [67]. The magnet system consists of a Central Solenoid (**CS**), a Barrel Toroid (**BT**) and two End-Cap Toroids (**ECT**), as shown in Figure 2.5. The resulting bending power is described by $\int Bdl$, where B is the field component orthogonal to the direction of the muon, and the integral

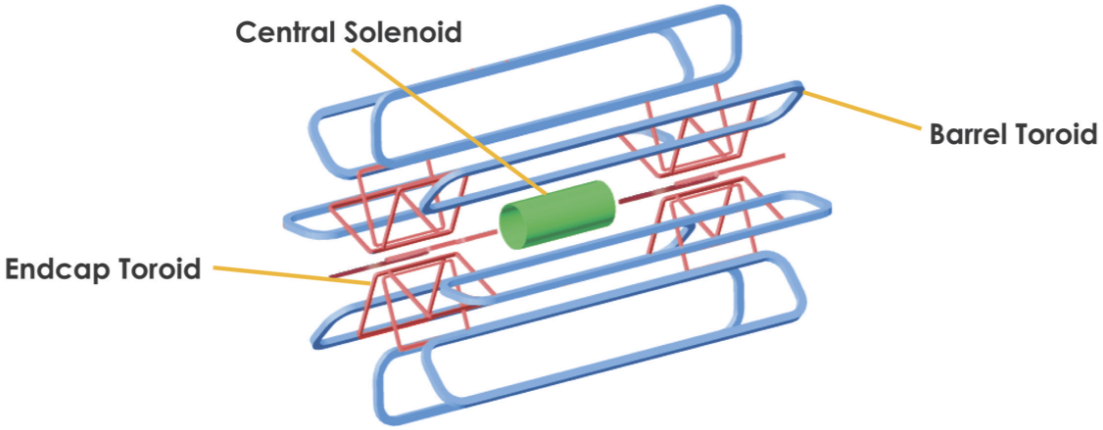

FIGURE 2.5: Magnet System of the ATLAS detector, © CERN 2013.

is taken on the straight line trajectory from the inner to the outer radius of the toroid. The BT covers the range 0.0 - 1.3 in η space, while the ET covers the range 1.6 - 2.7. The range $1.3 < \eta < 1.6$ is a transition region of these two toroids, they are overlapped in this region and the bending power is subsequently weaker.

The Central Solenoid is located in the immediate outer layer of the ID, to provide the required magnetic field for the ID to perform momentum measurements on charged particles. It creates a magnetic field strength of 2 T in the central field, and a peak of 2.6 T on the superconductor itself. It is 5.3 metres in length and 2.63 metres in diameter, with a bore in the middle that is 2.44 meters in diameter.

Both the BT and ECT consist of eight coils, assembled radially with a cylindrical symmetry around the beam axis, to provide magnetic fields for the MS in the outer layers of both the barrel and endcap regions. The Barrel Toroid consists of eight flat racetrack type coils with two double-pancake windings. They are made of 20.5 kA NbTi superconductor that is aluminium stabilized. It is 25.3 metres in length, with a inner(outer) radius of 9.4(20.1) metres, and produces a peak magnetic field of 3.9 T. The windings are placed inside aluminium-alloy casings, while each coil of the BT are placed in individual cryostats. The eight cryostats are connected with linking elements called voussiors and struts, and this entire structure provides the

mechanical stability for the coils against the internal forces between the coils.

The two End-Cap Toroids are each inserted at each cylindrical end of the BT and it is aligned with CS. Each are 5 metres in length, with an inner(outer) radius of 1.65(10.7) metres, and produces a peak magnetic field of 4.1 T. Its configuration of the eight toroids are at an rotational offset of 22.5 degrees with respect to the BT coil system, to optimize the bending power with radial overlap. Unlike the design for the BT, each ECT is assembled as one mass unit and placed inside a large cryostat. The internal forces are taken up by the supporting structure between the coils.

Tubes are welded on the casing of the windings with forced flows of helium at 4.5 K, for indirect cooling of the magnets. The CS is cooled by a dewar coupled to a refrigerator, while the ECT and BT additionally have helium pumps for guaranteed cooling with the forced helium flows.

2.2.3 Inner Detector

The Inner Detector is a detector system placed closest to the nominal interaction point [68]. It is completely contained inside the Central Solenoid, and consists of high resolution pixel detectors in the inner radii and tracking elements in the outer radii. This is achieved by a Semiconductor Tracker (**SCT**) that uses silicon microstrips, along with semiconductor pixel technologies near the vertex region that provide the highest granularities. Transition Radiation Trackers (**TRT**) on the outer parts of ID are comprised of straw tube trackers, as this design provides a low amount of detector material per tracking point, which subsequently helps greatly to reduce costs. Their relatively lower precision per point compared to the SCT in the inner radius is compensated by a large number of tracking points (typically 36 points per track) at a higher radius, and provide significant contributions to particle track reconstruction. This combination of the SCT in the inner part and the TRT on the outer part of the ID provides high precision and excellent

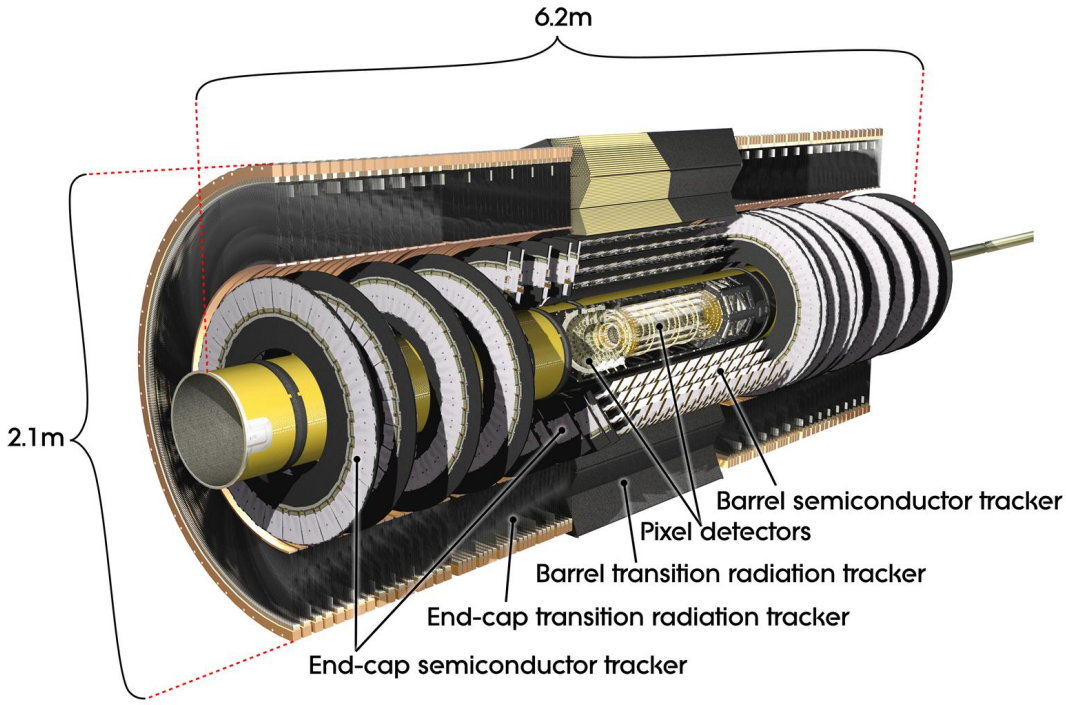

FIGURE 2.6: Cut-open view of the Inner Detector displaying the barrel and end-cap components of different sub-detectors and tracking elements, © CERN 2013

pattern recognition over ϕ and z ranges, as shown in Figure 2.6. This configuration also enables a good match between the precision of the measurements, as no one single measurement will dominate the momentum resolution.

The ID is assembled with three main parts. The barrel region stretches cylindrically over the range of ± 80 cm from the IP, and the remaining cylindrical parts comprise of two identical end-cap components that are installed on each end. The barrel region consists of high precision layers that are arranged concentrically around the beam. Precision tracking elements are placed within the radius <56 cm in this region, while continuous tracking and general support components make up the remaining outer parts. The pixel elements in the central part are segmented in units of R, ϕ and z, while the SCT use stereo strips at small angles

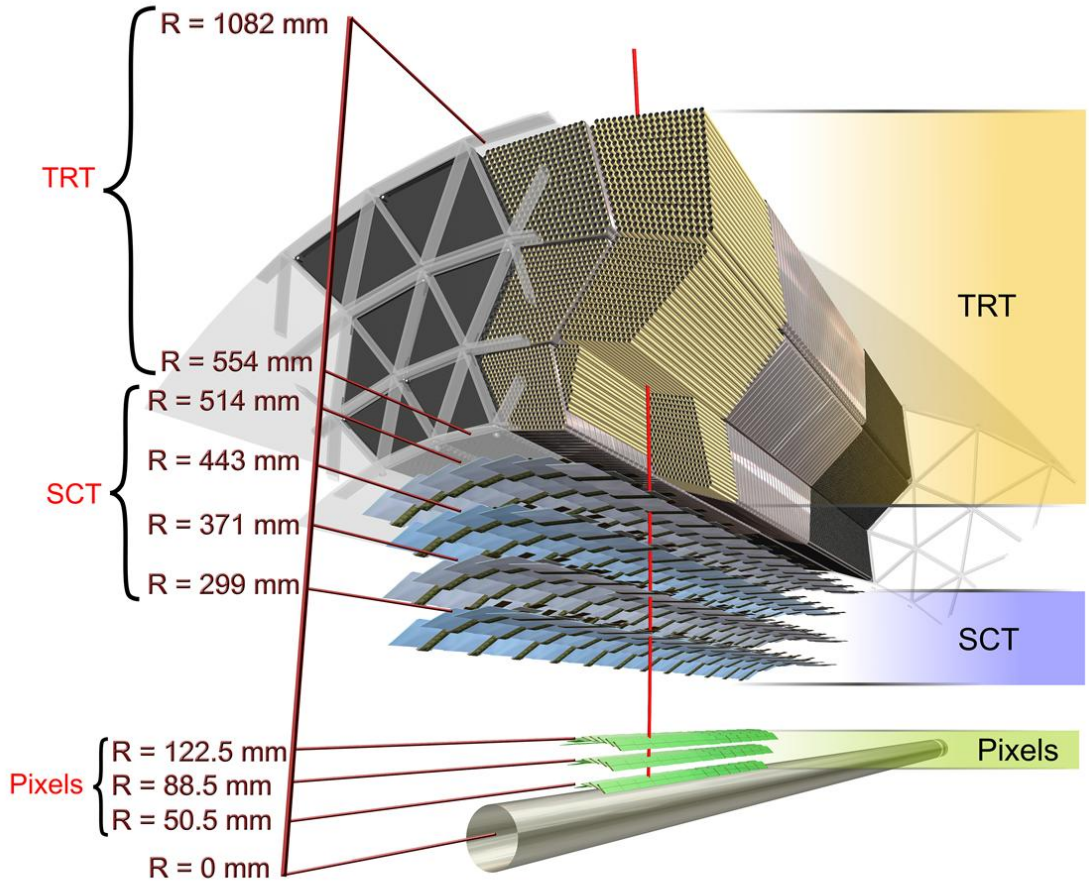

(A)

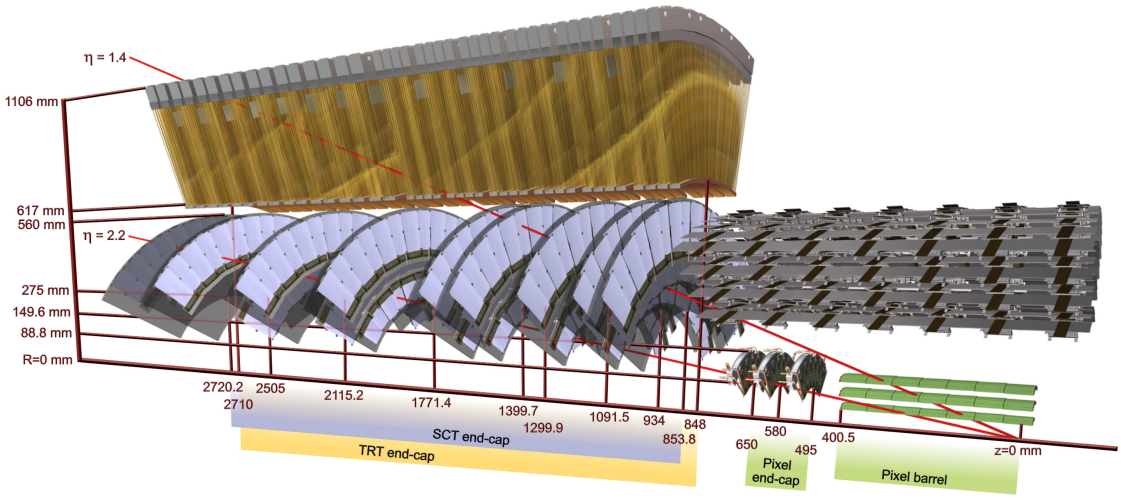

(B)

FIGURE 2.7: Structure of Inner Detector, displaying the two different configuration of modules in the barrel and end-cap region. Particle tracks at different angles show how the different components contribute to particle detection, © CERN 2013.

System	Component	Area (m^2)	Resolution σ (μm)	η Range
Pixel	1 removable barrel layer (B-layer)	0.2	$R\phi$=12, z=66	±2.5
	2 barrel layers	1.4	$R\phi$=12, z=66	±1.7
	5 end-cap disks on each side	0.7	$R\phi$=12, R=77	1.7-2.5
Silicon Strips	4 barrel layers	34.4	$R\phi$=16, z=580	±1.4
	9 end-cap wheels on each side	26.7	$R\phi$=12, R=580	1.4-2.5
TRT	Axial barrel straws		170 per straw	±0.7
	Radial end-cap straws		170 per straw	0.7-2.5
	36 straws per track			

TABLE 2.1: Parameters for the internal components of Inner Detector. Quoted resolutions are typical values, as actual values for each detector depends on the impact angle, as shown in Figure 2.7.

($\approx$ 40 mrad) to measure both R and z, and one set of strips in each layer for measurement in ϕ. The TRT straws in the barrel region are arranged parallel to the beam, and the tracking elements on the end-cap are installed on wheels that are arranged perpendicularly to the beam. To ensure uniform coverage of the η range over full acceptance, the final TRT wheel on the end-caps at high z ranges are extended inwards to a lower radius compared to the other TRT end-cap wheels. These configurations allow full tracking coverage over $|\eta| < 2.5$, which includes measurements of impact parameters as well as vertexing for τ and heavy flavour tagging. Technical parameters for these components are listed in Table 2.1.

The innermost layer of pixels are located approximately at a radius of 4 cm. Their lifetime is limited by the radiation damage that they suffer, and the exact time is dependent on the luminosity profile. Replacement after a few years of running is required to ensure adequate performance.

Pixel Detector

The Pixel Detector is located at the core of the inner detector, closest to the nominal interaction point. It is designed to provide high granularity and high precision measurements as close to the interaction point as practically possible. It provides three precision measurements over full acceptance, which mostly determines the resolution of impact parameters. It also determines the ID's ability to detect short lived particles such as B hadrons and τ leptons.

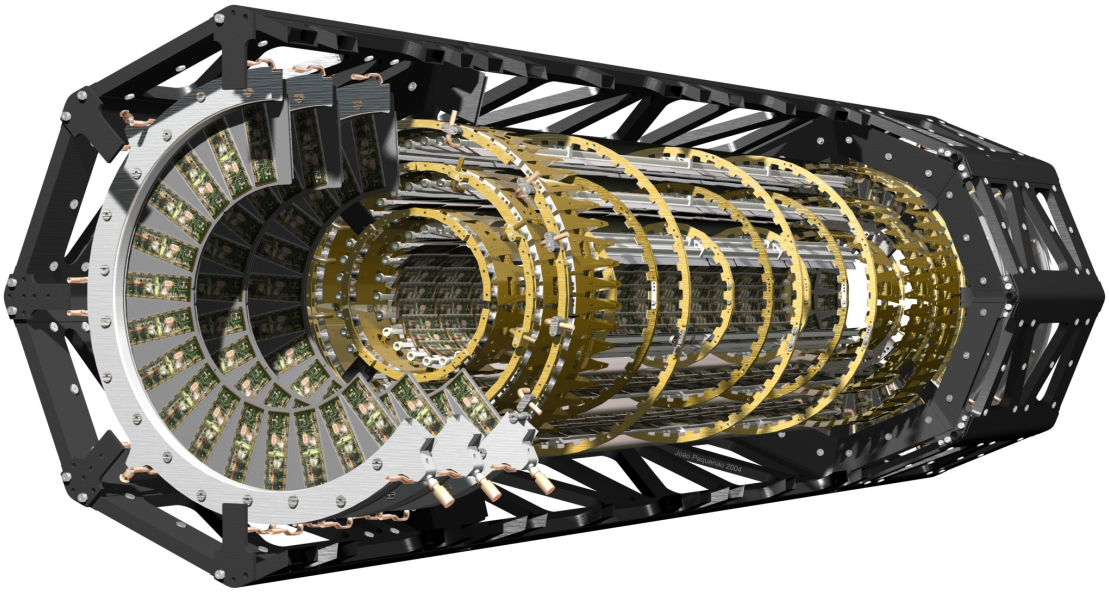

FIGURE 2.8: Cut-open view of the Pixel Detector showing its internal configuration, © CERN 2013.

Segment of sensors are arranged in a two dimensional configuration. This provides space points without the disadvantages of crossed striped geometries, however the corresponding interconnections for readout require advanced electrical techniques. The readout chips typically have large areas, and each element are equipped with individual circuits. They are also radiation hardened to withstand over 300 kGy of ionizing radiation, as well as over $5{\times}10^{14}$ neutrons per square centimetre over 10 years of operation. There are a total of 140 million detector elements in this

system, with each element being 50 μm in $R\phi$ direction and 300 mm in z. This high level of construction complexity as shown in Figure 2.8 is significant to the performance on pattern recognition.

The system comprises three barrels with average radii of approximately 4 cm, 10 cm and 13 cm, along with five disks of radii between 11-20 cm on each cylindrical end for complete angular coverage. The system is also designed to be highly modular, containing approximately 1500 barrel modules and 700 end-cap modules. Thickness of each module layer is approximately 1.7% of the radiation length, with each module being 62.4 mm long and 21.4 mm wide. Each module has 61440 pixel elements readout by 16 chips, and contain an array of 24 $\times$ 160 pixels. Both the barrel and end-cap modules are designed to be identical, and arranged with overlaps for hermetic coverage.

Semiconductor Tracker

The SCT system is designed to contribute towards measurements of momentum, impact parameters, as well as vertex position by providing eight measurements per track in the intermediate radial range. The surface area of the system is larger by an order of magnitude compared to previous generations of silicon microstrip trackers, and its high granularity provides excellent performance in pattern recognition. Additionally, the level of radiation that the silicon microstrip trackers in this system encounter in the LHC environment will alter the fundamental characteristics of the silicon wafers, unlike any that the previous generations have faced.

The barrel component of the SCT provide precision points in the $R-\phi$ and z spaces using eight layers of silicon microstrip detectors, with the z measurement obtained by small angle stereo. Each silicon detector has a surface area of 6.34$\times$6.40 cm^2, with 768 readout strips and 80 μm pitch. Each module has four single sided p-on-n silicon detectors, and each side of the module has a strip 128 cm in length, formed by connecting two detectors together with wire. Two of these units are

glued together with a back-to-back configuration, separated by a heat transport plate and an angle of 40 mrad. The readout chain has a front-end amplifier and a discriminator, and the electronics are mounted above on a hybrid. The end-cap modules use tapered strips instead as well has having one set aligned radially, but otherwise are very similar in design. The strips at the outer radii of the end-cap modules are $\approx$ 12 cm in length, and are $\approx$ 6 - 7 cm long at the innermost radius for optimal η coverage across all end-cap wheels.

The SCT has a spatial resolution of 16 μm in $R-\phi$ space and 580 μm in z space, and each module provides one measurement in each of R, ϕ and z. The system contains 61 m^2 of silicon detectors with 6.2 million readout channels, and can distinguish tracks that are separated by more than 200 μm.

The barrel SCT modules are mounted on carbon-fibre cylinders that carry the cooling system. The four barrels at different layers with radii approximately at 30.0, 37.3, 44.7 and 52.0 cm are connected together. The end-cap modules are installed up to three rings on each of the nine wheels, and are connected by a space frame. The configuration of these end-cap modules on the wheels are arranged accordingly for a coverage of $| \eta | \leq 2.5$.

Both the Pixel Detector and the SCT are designed using materials with the lowest possible coefficient of thermal expansion, to account for issues such as operation in cryogenic temperatures, removal of heat generated by electronics as well as detector leakage current. Prior to the LHC operation, prototypes of these modules have been tested in magnetic fields with test beam conditions, and have successfully demonstrated the required performance in resolution, signal to noise as well as speed. Modules containing detectors and their corresponding electronics have also been tested with the expected level of radiation during LHC operation over ten years, and have shown to perform successfully within specifications.

Transition Radiation Tracker

The Transition Radiation Tracker is operated by straw detectors with small diameter, each containing a sense wire in the middle and filled with gas mixtures. The diameter of each straw is 4 mm, and located inside is a $W - Re$ sense wire that is 30 μm in diameter and plated in gold. The straws are filled with a non-flammable gas mixture composed of 70% Xe, 20% CO_2 and 10 % CF_4, totalling to a volume of 3 m^2. This configuration enables the system to operate in the expected high rate environment of the LHC, with fast response as well as good mechanical and electrical properties. The detector is intrinsically radiation hard, and allows a large amount of measurements (typically 36) for every track.

The barrel component of the TRT contains 50 000 straws that are parallel to the beam. Each of them are divided in the middle into two identical parts to reduce occupancy, with the readout at each end. Alternatively the 320 000 straws in the end-cap component are arranged perpendicularly to the beam, with the readout designed at the outer radius. There are a total of 420 000 total electrical channels, with each channel providing a single drift time measurement. This gives a spatial resolution of 170 μm per straw with two independent thresholds. This arrangement allows the detector to distinguish between tracking hits that pass a lower threshold, and the transition radiation hits that pass at a higher threshold. The inclusion of xenon in the gas mixtures provides electron identification ability, as xenon gas can be used to detect transition radiation photons created in the radiator between the straws.

Each barrel module is built with either 329 or 793 axial straws, providing coverage over a radial range of 56 - 107 cm. The first six radial layers provide coverage for the region between the barrel and end-cap components, and are inactive over the central 80 cm of their length for the reduction of occupancy. There are 9 wheels in each of the two end-caps, with the 14 wheels that are closest to the IP covering the radius range of 64 - 103 cm. The two wheels that are furthest from the IP on each end extend to an inner radius of 48 cm, for keeping a constant number of

crossed straws at full acceptance. The other 6 wheels on each end-cap contain only half the amount of straws per cm in z coordinate compared to the other wheels, to avoid unnecessary gain in the number of crossed straws.

Priority of the TRT system design is to obtain good occupancy and counting rate performance. Hit rates above the lower threshold in the barrel region varies with radius from 6 - 18 MHz, while the rates in the end-caps varies with z from 7 - 19 MHz. The maximum rate above the transition radiation threshold is approximately 1 MHz. Occupancy within a single drift-time bin is approximately one third of the entire active time window. Tests with an average counting rate of 12 MHz have been performed, and a position accuracy of approximately 170 μm have been achieved. Due to shadowing effects, only about 70% of the straws provide a correct drift time at this rate. This weakness is compensated by the large number of straws hits available per track, which the accuracy of the combined measurement at the expected luminosity of the LHC is assured to be better than 50 μm when averaged over all straws, with a systematic error of approximately 30 μm.

The continuous tracking component of the TRT detector assures a good performance on pattern recognition. Spacing of straws are optimized for tracking within the available radial space, and the straws are distributed over maximum possible path lengths. This reduces the effect of loopers and interactions that can saturate small regions of the detector as well as enhancing the performance of pattern recognition. However this configuration does not provide optimal performance for electron identification, but is compensated by a larger path length through the radiator material and fewer straw detectors.

2.2.4 Calorimetric System

The calorimetric system of the ATLAS detector is constructed with the purpose of measuring the energy of outgoing particles from the pp collisions, by stopping them from passing through (not including muons and neutrinos) [69]. There are Elec-

tromagnetic Calorimeters (**ECAL**), Hadronic Calorimeters (**HCAL**) and Forward Calorimeters (**FCAL**) in the immediate outer layer from the Central Solenoid embedding the Inner Detector (see Section 2.2.3 and 2.2.2). The ECAL covers the range η range of $\mid \eta \mid < 3.2$, while the HCAL covers $\mid \eta \mid < 1.7$ with its barrel component and $1.5 < \mid \eta \mid < 3.2$ with its end-cap component, along with the FCAL covering $3.1 < \mid \eta \mid < 4.9$. One barrel and two end-cap cryostats are used to house the calorimeters that are closest to the beam. The barrel cryostat contain the barrel component of the Electromagnetic Calorimeters, while the two end-cap cryostats contain the Electromagnetic End-cap calorimeter (**EMEC**), the Hadronic End-cap Calorimeter (**HEC**) and the FCAL. All of these detectors utilize Liquid Argon (**LAr**) and are placed near the beam line, where cryogenically liquefied argon are used as the active detector medium. This design is chosen for its high level of radiation tolerance, as well as its linear and stable behaviour. The barrel component of the HCAL is divided in the central barrel part which wraps around the barrel part of ECAL, and the extended barrel part enclose the end-cap LAr calorimeters, as shown in Figure 2.9. These parts of HCAL utilizes plastic scintillator plates that are embedded in iron absorbers, where the iron absorbers also act as the flux return for the main solenoid.

Electromagnetic Calorimeter

The barrel component of the Electromagnetic Calorimeter has complete symmetry in ϕ without any azimuthal gaps, and is responsible for $\mid \eta \mid < 1.475$. Two identical halves are separated at $z = 0$ by a thin gap of 6 mm, totalling to an axial length of 6.4 metres with an inner(outer) radius of 1.4(2.0) metres. The two identical end-cap components at each end contain two coaxial wheels, with an overall inner and outer radii of 0.33 and 2.1 metres, respectively. The outer wheel covers the range $1.375 < \mid \eta \mid < 2.5$ while the inner wheel covers $2.5 < \mid \eta \mid < 3.2$. The barrel component and the outer wheel provide precision measurements, while the inner wheel makes lower resolution measurements at high η ranges. The primary design is based on array configurations of lead absorbers, with liquid argon filling

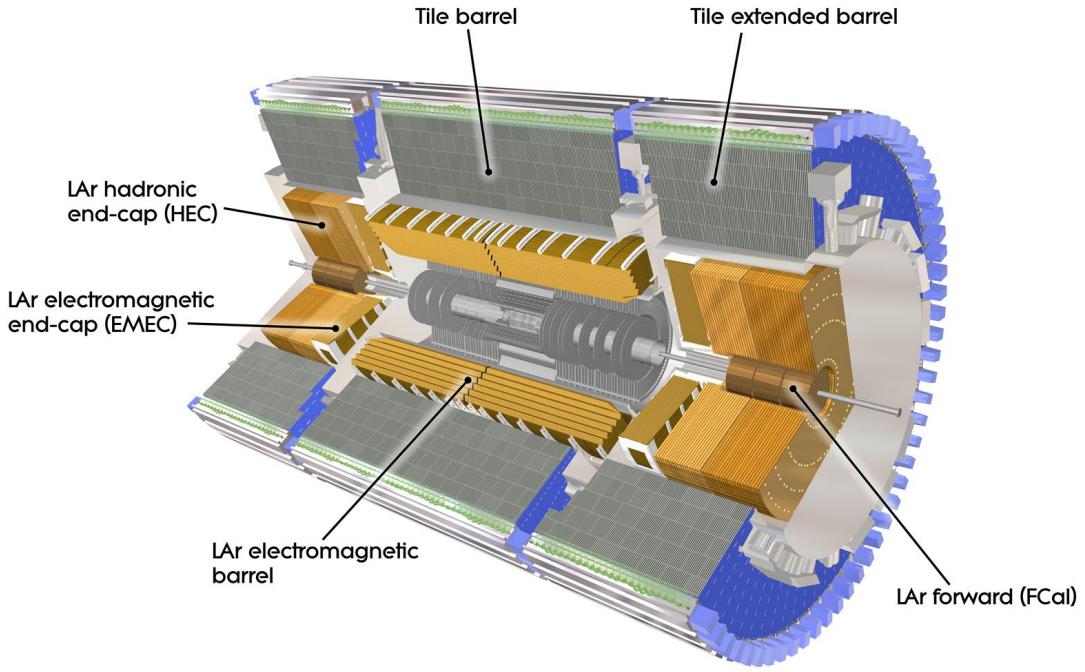

FIGURE 2.9: Cut-open view of the Calorimetric system showing its internal configuration, © CERN 2013.

the in between gaps. In the barrel region, the thickness of the lead absorbers are optimized as a function of η for energy resolution performance, while all LAr gaps are at 2.1 mm. The lead absorbers in the end-caps have constant thickness, with the size of LAr gaps increasing with radius.

Cascades of EM particles are induced by these lead absorbers, creating "Electromagnetic showers" that are characterized by *radiation length* X_0. Incident electrons primarily lose energy in these lead absorbers via emission of bremsstrahlung photons, while the incident photons lose energy via e^+e^- pair production. The LAr sampling layers are sandwiched between the lead absorber layers, where the liquid argon is ionized by the electrons from the EM shower. The resulting charged current is collected by the accordion shaped electrodes for shaping and digitization by other electronic components.

As shown in Figure 2.10, the calorimeter is divided into three radial layers that are made of accordion shaped electrodes and lead absorber plates. The innermost layer (often referred to as the $|\eta|$ strip layer) is designed with fine segmentation for high precision measurements, while the middle layer is the thickest for absorbing most of the deposited energy. The outermost layer is much coarser in granularity with the primary purpose of absorbing high energy tails of EM showers, in order to minimize leakage into the Hadronic calorimeters.

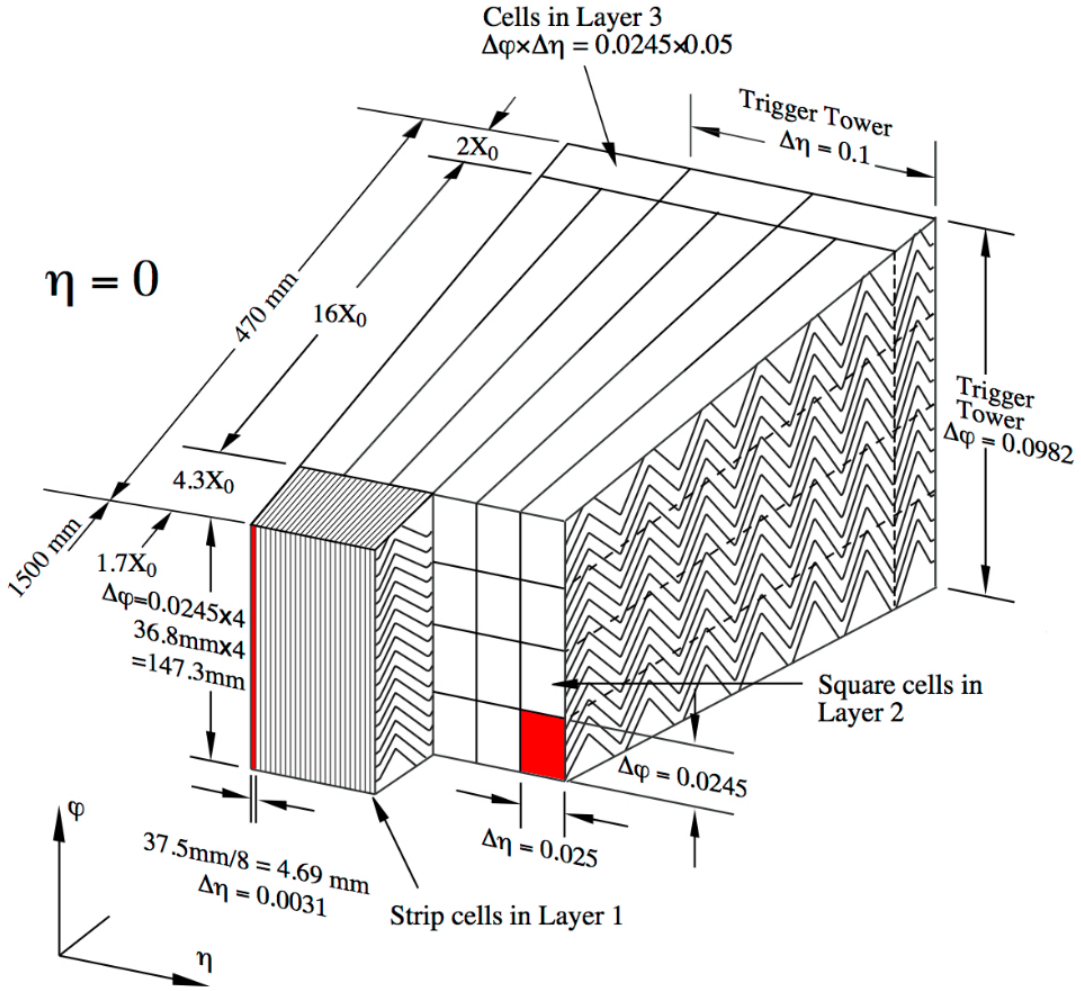

FIGURE 2.10: Structural view of Electromagnetic Calorimeter barrel component, showing the granularity in η and ϕ as well as their differences in the three radial layers [62].

Hadronic Calorimeters

Successive inelastic collisions with the nuclei in matter causes hadrons to lose energy while passing through the material. The resulting "Hadronic shower" from large amounts of incident hadrons are characterized by the mean path between these inelastic collisions, referred to as the *interaction length* λ_0. The Hadronic End-cap Calorimeter is installed close to the beam line, immediately beyond the EMECs. They also use the LAr technology for its ability to tolerate high levels of radiation. Tile Calorimeters utilizing plastic scintillators are used as the barrel part of HCAL, and it is installed at greater radial distance from the beam line.

Each HEC is constructed with two independent coaxial wheels with an inner(outer) radius of 0.475(2.03) metres, and they are responsible for detection in the range of $1.5 < | \eta | < 3.2$. Thin copper plates are separated by 8.5 mm gaps in this detector, where electrodes are placed to collect signals from ionized LAr. The copper plates are typically 25 mm thick in the wheel closer to the interaction point, and are 50 mm thick in the outer wheel.

The Tile calorimeters are installed in the immediate outer radial layer from the LAr calorimeters. The barrel part of HCAL is 5.8 metres in length and embeds the EM barrel calorimeter, while the extended barrel is each 2.6 metres long and enclose the end-cap calorimeters, as shown in Figure 2.10. They both have an inner(outer) radius of 2.28(4.25) metres, and respectively cover the range $| \eta | < 1.0$ and $0.8 < | \eta | < 1.7$. The barrel and extended barrels contain a total of 64 modules, and are longitudinally divided into three layers, respectively with approximately 1.4, 4.0 and 1.8 λ_0 at $\eta = 0$. As radiation tolerance is a relatively smaller concern compared to the overall cost, steel is used as passive absorbers interleaved with scintillating plastic tiles that are used as active medium. Wavelength-shifting fibres are connected on both sides of the scintillating tiles to separate photomultiplier tubes, where the photons from scintillation are guided to front end electronics.

Forward Calorimeters

The Forward calorimeter is installed inside the cavity of the HEC surrounding the beam. Is is approximately 4.7 metres from the IP, covering $3.1 < | \eta | < 4.9$. It is divided into three cylindrical modules, where the module closest to the IP uses copper for EM detection, while the outer two use tungsten for hadronic measurements. The calorimeter uses a metal matrix configuration of tubes containing rods, with 250 μm gaps in between that is filled with LAr as an active medium.

2.2.5 Muon Spectrometer

The main purpose of the Muon Spectrometer is to provide high precision momentum measurements of muons, with the help of the magnetic field generated by the toroids (as described in Section 2.2.2) to curve the muon trajectories [70]. The Barrel Toroid provides magnetic field for the $| \eta | < 1$ region, while the End-cap toroids are responsible for the $1.4 < | \eta | < 2.7$ region. The transition region of $1.0 < | \eta | < 1.4$ is covered by the combination of the barrel and end-cap toroids. The created magnetic fields are mostly orthogonal to the muon trajectories, to optimize the measurement resolution due to multiple scattering.

Chambers in the barrel region are installed in three cylindrical parallel layers (stations) around the beam, at the immediate greater radial distance from the calorimetric system, as shown in Figure 2.11. Gaps between large chambers in this region are filled with smaller chambers to complete the coverage in ϕ. Alternatively the chambers in the transition and end-cap regions are installed in four different layers that are orthogonal to the beam. This arrangement in the end-caps ensures quality muons to register hits in at least three stations in the greatest possible range in η, which will be described more in detail in Section 5.3.1. Muon Drift Tubes (**MDT**) are typically used as high precision tracking chambers for muons over most of the η range, while Cathode-Strip Chambers (**CSC**) with higher granularity and radiation tolerance are used closed to the IP at high η range of $2 < | \eta | < 2.7$. The

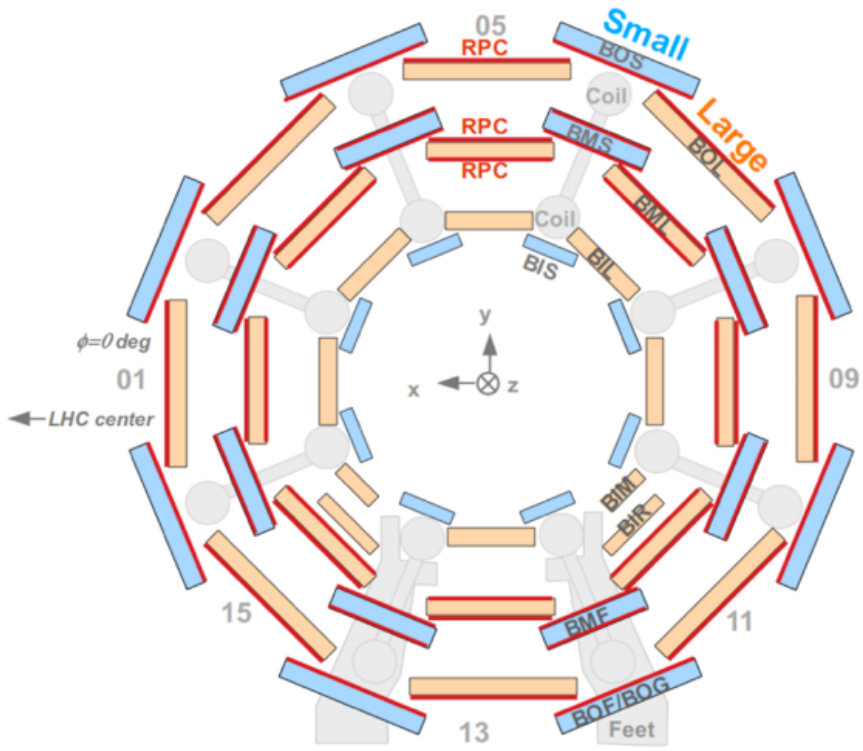

(A)

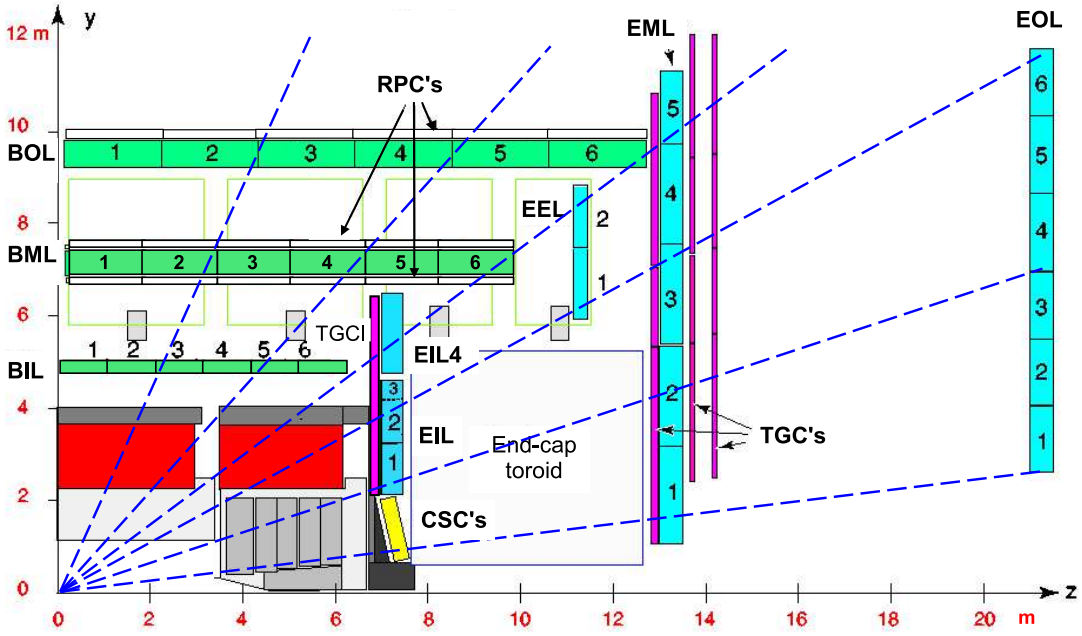

(B)

FIGURE 2.11: Different cross-sectional views of the Muon Spectrometer. The cross-sectional view of the barrel part in the x-y plane in shown in Figure 2.11a, with small sectors of MDTs are shown in light blue, while large sectors are shown in orange. Arrangement of RPCs around each MDT sector are also shown in red. Figure 2.11b displays a quadrant of the cross-sectional view in the y-z plane, displaying the barrel MDT chambers in green, and the end-cap chambers in light blue [71].

mechanical accuracy of these tracking chambers are ensured by specially designed optical alignment systems [72, 73].

The Resistive Plate Chambers (**RPC**) and Thin Gap Chambers (**TGC**) are used as trigger systems respectively in the barrel and end-cap regions. They are installed for providing bunch crossing identification and well defined p_T thresholds for triggering, as well as measurement in the coordinate that is orthogonal to the measurement made by the precision chambers.

Precision Chambers

Muon Drift Tubes chambers located in the barrel, transition and end-cap regions are all composed of aluminium tubes 30 mm in diameter with 400 μm in thickness. The tube lengths vary from 70 to 630 cm in chambers of different sizes, and all contain a *W-Re* sense wire of 50 μm diameter in the middle. These tubes are filled with a non-flammable gas mixture consisting 93% Argon and 7% CO_2 at an absolute pressure of 3 bar. Individual tubes are enclosed on both ends with plugs for accurate positioning of the anode wires, control and maintaining the wire tension as well as gas and electrical connections (See Figure 2.12a). The gas mixture is ionized when a muon is passed through, resulting electrons are drifted towards the anode wire in the middle, as shown in Figure 2.12b. Electrons accelerated by the electric field towards the anode wire can cause additional ionizations near the anode wire, resulting in exponential growth of electrons. The repulsive force this avalanche of electrons near the anode wire ($\approx$ a few diameters of the wire) can displace electrons from the anode wire. The resulting current in the anode wire from the displacement of electrons are detected by an electronic sensor [74].

Individual tubes are typically arranged in the MDT chambers with multiple monolayers on both side of rigid support structures, as shown in Figure 2.12. MDT chambers in the inner stations are constructed with 2×4 layers of drift tubes, while the middle and outer stations uses a 2×3 configuration, as shown in Figures

2.12c and 2.12d. These support structures (also referred to as spacer frames) are designed with slight bends accordingly, to account for the sagging of wires. Optical systems are also installed to monitor mechanical deformations due to temperature and gravity effects.

The Cathode Strip Chambers are installed near the beam line and close to the IP to provide precision measurements of muon tracks. Radially oriented parallel anode wires at 1900V are arranged orthogonally between cathode read-out trips inside the chambers, which are filled with a non-flammable gas mixture consisting 30% Argon, 50% CO_2 and 20% CF_4. These multiwire proportional chambers provide a high spatial and time resolution as well as excellent radiation tolerance and low neutron sensitivity. Avalanches are formed by the anode wire when a muon is passed through, and the induced charge on the segmented cathodes are used to obtain a precision measurement, as shown in Figure 2.13a. The CSC system that is made of an end-cap wheel at each end are composed of large and small sectors (See Figure 2.13b), where the CSCs are arranged in 2×4 layers around the support structure, similar to the MDTs.

Trigger Chambers

RPCs and TGCs combine to form the trigger system for muons. They provide a well defined p_T threshold for triggering, as well as measurements of muon tracks in the non-bending (ϕ) plane.

RPCs are gas detectors that gives an excellent space time resolution of 1 cm × 1 ns with digital readout. It uses a gas mixture primarily consist of tetrafluoroethane ($C_2H_2F_4$), with a small amount of SF_6. The basic unit is built with two parallel resistive plates, separated with a small gap by two insulating spacers, where the gas mixture is filled. A uniform electric potential of typically 4.5 kV/mm is applied in the gap, to induce electron avalanches when a muon is passed through. Signals are readout by capatitativly-coupled metal strips at both sides. These metal strips

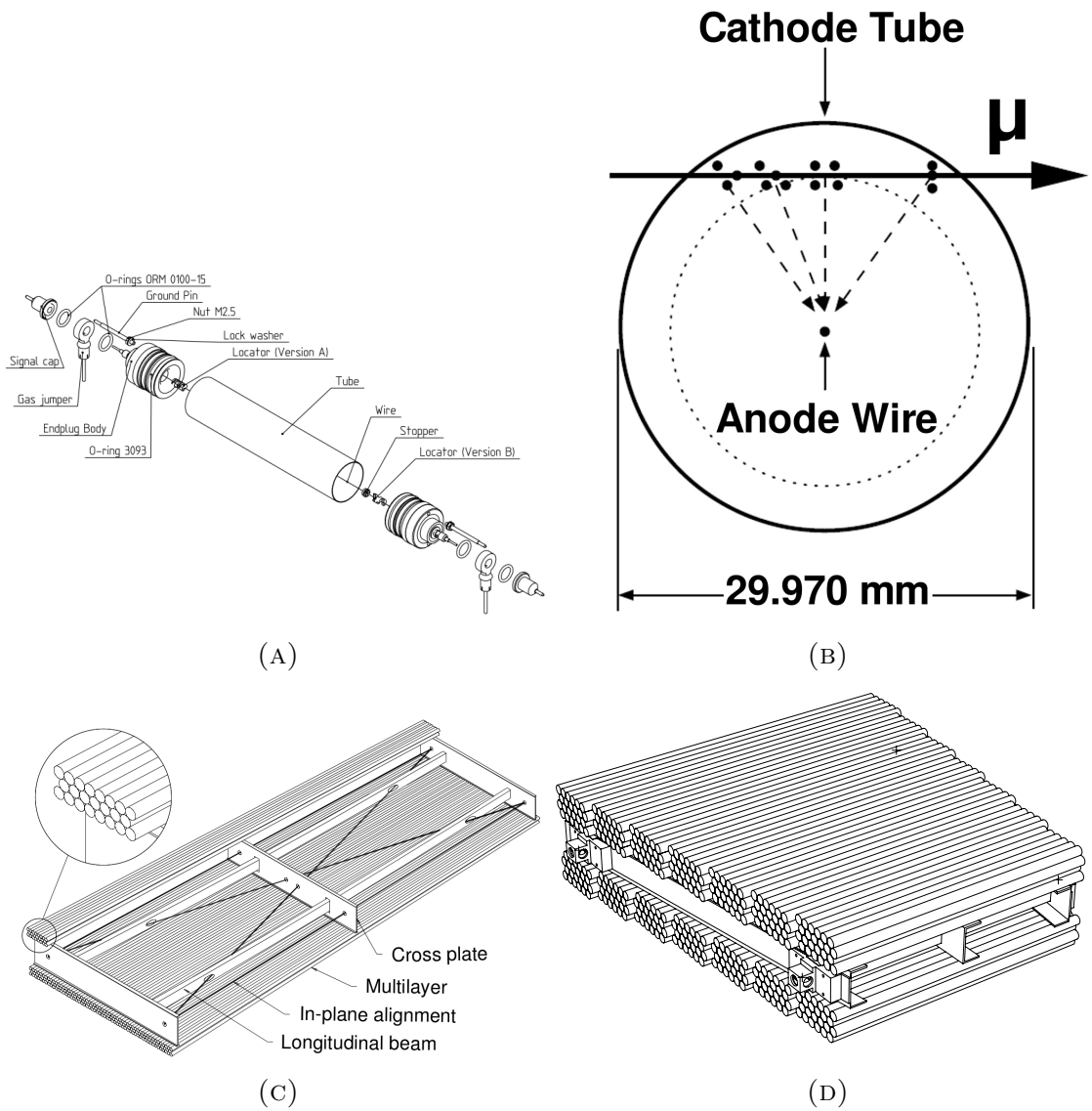

(A) (B)

(C) (D)

FIGURE 2.12: Figure 2.12a shows the components of a single Muon Drift Tube, while Figure 2.12b shows the cross section of the wire. Figure 2.12c shows the associated support structure and its optical alignment system, and Figure 2.12d is a schematic of one complete chamber [62, 75].

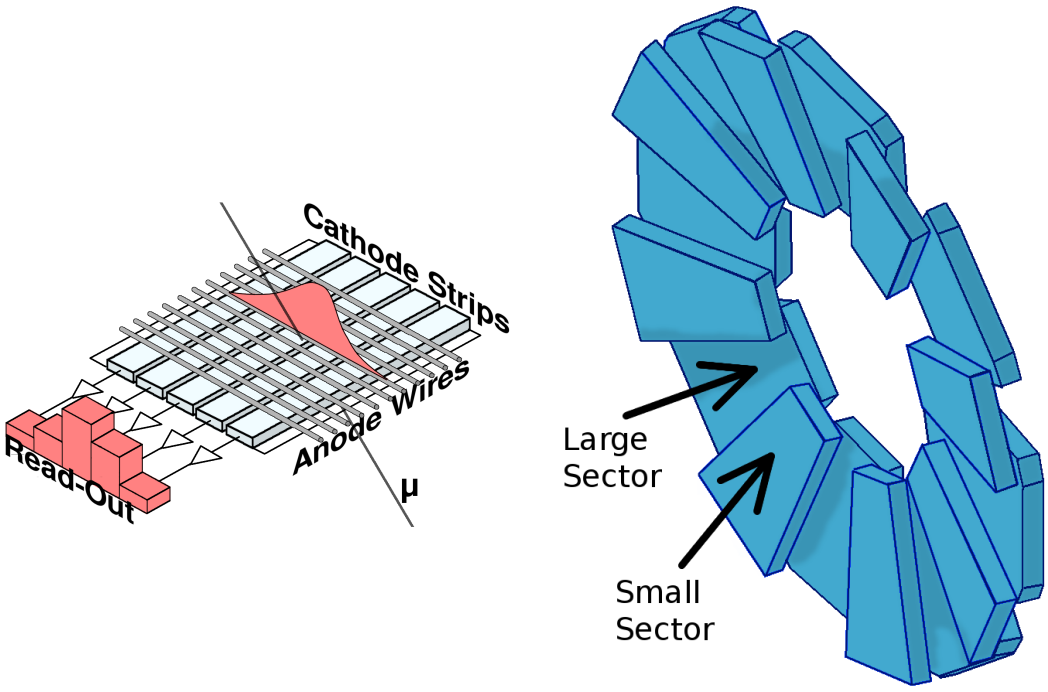

(A) (B)

FIGURE 2.13: Figure 2.13a shows the CSC configuration of Cathode readout strips with perpendicular anode wires. Figure 2.13b shows the arrangement of large and small sectors on the CSC end-cap wheel [62, 76].

are arranged in two series orthogonal to each other respectively in η and ϕ planes, to provide measurements from orthogonal coordinates. Further structural details are shown in Figure 2.14a.

TGCs in the end-cap region are also multiwire proportional chambers, similar to the CSCs. Unlike the CSCs where the cathode-anode distance is the same as the anode wire pitch, the anode wire pitch for TGCs are greater than the cathode-anode distance. Anode wires are arranged parallel to the MDT, and orthogonal to the cathode readout strips. Two G-10 fibre class plates with graphite coating that act as cathodes sandwiches the anode wires in the thin gap between them, where it is filled with a gas mixture consisting 55% CO_2 and 45% n-pentane (n-C_5H_{12}).

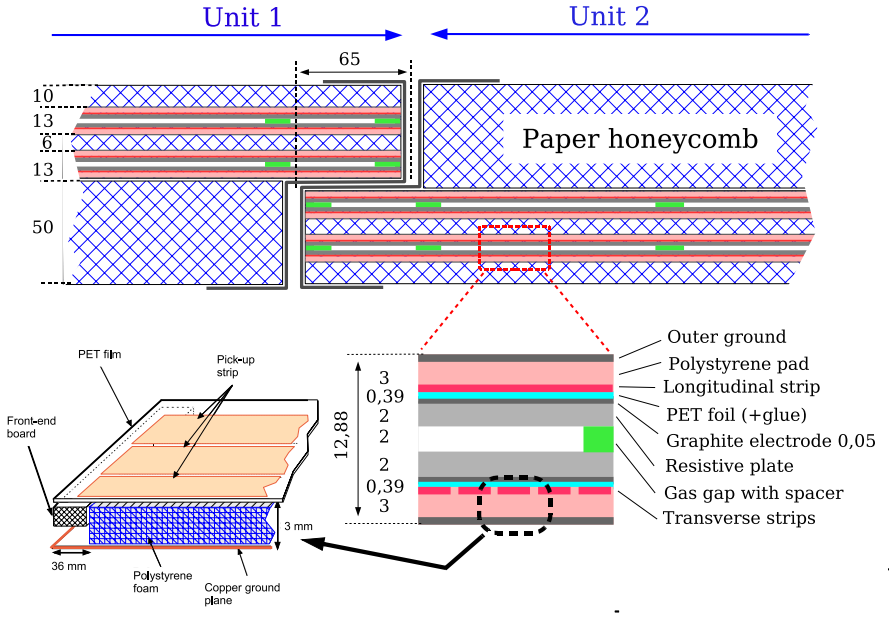

(A)

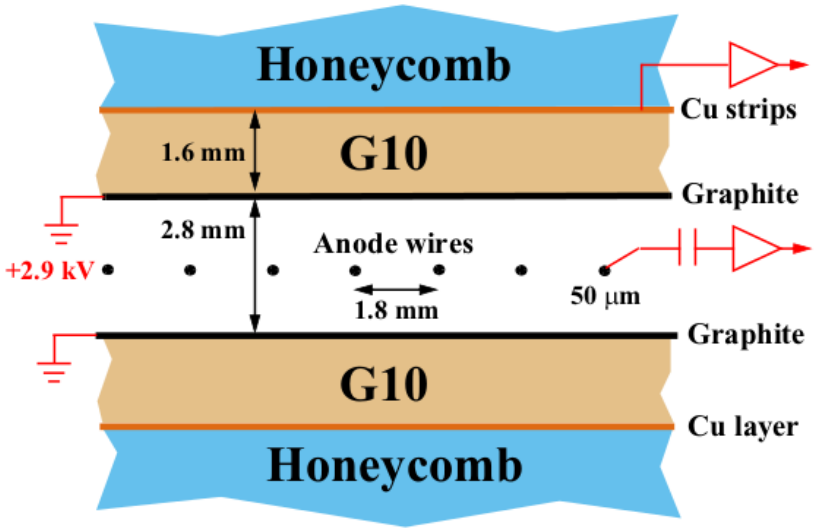

(B)

FIGURE 2.14: Figure 2.14a Schematic of the RPC internal structure, all dimensions are in millimetres. Figure 2.14b Schematic of a single element of the TGC, showing its internal configuration [62, 75].

They are arranged in doublet and triplet layers and installed on circular disks. Internal structure on an element with dimensions are shown in Figure 2.14b.

2.2.6 Forward Detectors

LUCID (**LU**minosity measurement using **C**herenkov **I**ntegrating **D**etector) [77], ZDC (**Z**ero **D**egree **C**alorimeter) [78] and ALFA (**A**bsolute **L**uminosity **F**or **A**TLAS) [79] are three forward detectors of ATLAS that are installed respectively at ± 17 m, ± 140 m and ± 240 m from the IP. LUCID uses aluminium tubes filled with C_4F_{10}, to indirectly provide measurement for integrated luminosity, as well as online monitoring of instantaneous luminosity. ZDC uses quartz strips between tungsten and steel layers for the detection of neutral particles, for the measurement of *centrality* of Heavy-Ion collision events. ALFA uses its ability to detect small angle elastic scattering with modules of scintillating fibres.

2.2.7 Data Acquisition and Triggering

Similar to the other experiments around the LHC ring, ATLAS utilizes the circulating proton beams to search for new physics, and only the collision data collected during intended conditions can be used for physics analysis. Primary requirement for this is to have collisions of stable beams in the IP of ATLAS. Once the LHC machine declares that stable beams conditions have been achieved, the various detectors within ATLAS will be ramped up from a safe idle state to an operation state where it is optimal to collect data for physics analysis.

ATLAS divides the operation time of data taking into runs, which can be as long as a few hours. Each run is also divided into smaller units called luminosity blocks that are on average 1 minute each, where the collision data collected is stored along with other important information such as detector status. This division of data enables catergorization of data in smaller portions, and the collected collision data

within each luminosity block is labelled with either good or bad quality, depending on the associated beam and/or detector conditions. Luminosity blocks with good beam and detector conditions are used for physics analysis, while some of the other runs may only include parts of the detector in operational state, dedicated for detector studies and calibration purposes.

In the 2012 data taking period, the LHC provides beams with 50 ns bunch spacing, allowing a collision rate of 20 MHz in the ATLAS detector. With each event requiring 1.5 MB to store, it is still technically impossible to store all events which equates to 60 TB of data every second. Interesting physics resulting from head on particle collisions are usually extracted from the transverse component of kinematic quantities, hence a three level trigger system, namely Level 1 (**LVL1**), Level 2 (**LVL2**) and Event Filter (**EF**), are used to select events with high transverse quantity objects for physics analysis. A schematic of the Trigger and Data Acquisition (**TDAQ**) system is shown in Figure 2.15.

The LVL1 trigger is the pure hardware, first trigger at low level that decides whether an event should be kept. The detector readout is temporarily stored in the pipeline memories during the required 2 μs of decision making. Results from L1Muon (RPCs and TGCs as described in Section 2.2.5) and L1Calo (Calorimetric System described in Section 2.2.4) selects muons, electrons, photons and hadronic jets with high transverse momentum p_T, as well as large total and missing transverse energy at a reduced granularity level. Trigger "menus" with various combinations of threshold values in the Central Trigger Processor are used to identify interesting events, from the multiplicities of objects passing different thresholds. Regions of Interest (**RoI**) are then created with η and ϕ coordinates as well as the p_T threshold of the object the LVL1 trigger has labelled "interesting". This reduces the event rate from 40 MHz to approximately 75 kHz.

The LVL2 and EF are software triggers that refines the selection of events in parallel, and are combined to take the label High Level Triggers (**HLT**). The LVL2 trigger analyses event information provided by the RoIs at a full detector resolu-

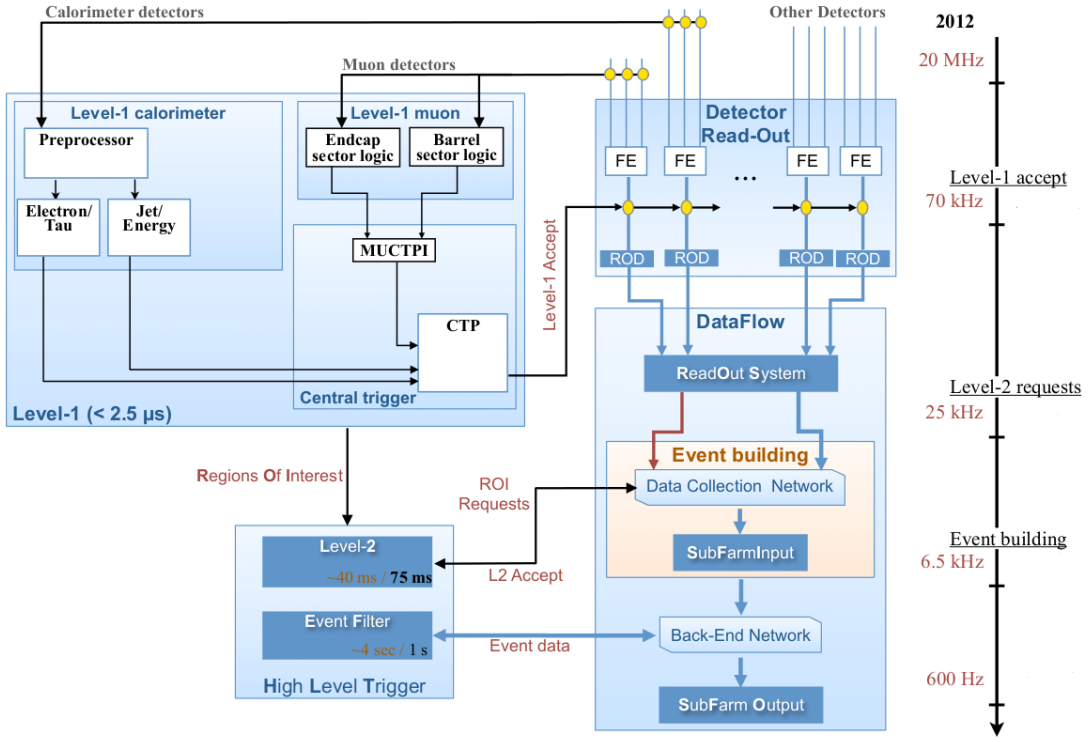

FIGURE 2.15: Schematic diagram of the TDAQ system [80]

tion level, for better object identifications such as track matching and calorimeter shower shape to distinguish electrons and photons. This process requires about 40 ms and the rate is reduced to 6.5 kHz. The EF then completes the reconstruction of full event using approximately four seconds, providing a final event rate of approximately 600 Hz for long term storage. This process from LVL1 to EF is referred to as the "trigger chain", and events that pass the entire chain without further screening after LVL1 trigger are referred to as unprescaled events. Lower event rates are also controlled with prescale factors to produce *prescaled events*, as required by some physics studies such as QCD. they are otherwise prescaled. Dedicated trigger chains also enables the EF to classify the events into `Muon`, `Egamma` and `JetTauEtmiss` streams, depending on the triggers fired by the events. The streams are then sent to CERN's central data recording facility for long term storage, and subsequently for physics analysis focusing on different aspects.

Chapter 3

Generation of Monte-Carlo Simulated Events

Since the beginning of its stable operation in late 2009, the LHC have had data-taking schedules for pp collisions for most of the year from 2010 to 2012, progressively increasing instantaneous luminosity and CM energy. Even only with a record rate of 600 Hz compared to the collision rate of 20 MHz, a very large amount of data is still available for physics analysis. As the presence of new physics would only deviate from the SM predictions by a very small amount, this platform with high level of statistics permits their observations. This also means that predictions of SM *backgrounds* and new physics *signals* at high levels of accuracies are needed for comparison with data, in order to estimate their contribution to the total detector output. Monte-Carlo (**MC**) event samples for various background and signal processes are produced via the combination of event simulations and its resulting detector response, for comparisons with detector read out from real collisions. A computing framework called ATHENA [81] provides the platform for the necessary tasks described in this chapter to be carried out.

3.1 Event Generation

Theoretical predictions of interactions between constituent partons carry central importance to the generation of events during hadron-hadron collisions in ATLAS. The momentum transfer Q^2 during hadron scattering interactions is used to classify whether it is a "hard" or "soft" process. The accelerated colour-charged particles

from the hard processes emits QCD radiation, the resulting parton multiplication phenomenon referred to as "showering" of partons, which are low Q^2 (soft) interactions and are modelled with Parton Showering algorithms. A process called Hadronization would then occur, where the remnants of quarks and gluons would form colourless hadronic bound states. Both Parton Showering and Hadronization are dominantly (soft) interactions with lower Q^2 values where perturbative QCD do not provide stable solutions, and other techniques are instead employed. Short descriptions of each common MC generator used in the analysis presented in this thesis are given in Appendix A.

3.1.1 Hard Processes

The ability to accurately describe the internal structure of the colliding protons is also crucial for the modelling of hadron scattering interactions. The prediction on properties of the constituent partons however, require the use of Factorization theorem along with Parton Distribution Functions (**PDF**) evaluated from internal structure parametrization. These PDFs describe the distribution of contributions from its constituent partons to the total momentum of the proton at the energy scale Q^2. The cross section for two colliding protons, p_1 and p_2, emerging in a final state with X particles, is given by [82]:

$$\sigma_{p_1 p_2 \to X} = \sum_{ab} \int_0^1 dx_a dx_b f_a^{p_1}(x_a, Q^2) f_b^{p_2}(x_b, Q^2) \hat{\sigma}_{(ab \to X)} \tag{3.1}$$

where $f_a^{p_1}(x_a, Q^2)$ and $f_b^{p_2}(x_b, Q^2)$ are the PDFs of p_1 and p_2 respectively. They are hadronic matrix elements regularized for the inclusive distribution of constituent partons a and b to carry momentum fraction x, renormalized at the factorization scale Q^2. The parton level cross section for a and b to produce X is represented by $\hat{\sigma}_{(ab \to X)}$, and its value (leading order) is obtained by integrating the differential cross section over phase space:

$$\hat{\sigma}_{(ab\to X)} = \int d\hat{\sigma}_{(ab\to X)} = \int \left[\prod_{i=1}^{X} \frac{d^3p_i}{(2\pi)^3 2E_i}\right] \delta^4\left(p_a + p_b - \sum_{i}^{X} p_i\right) \mid \mathscr{M}_{ab\to X} \mid^2 \quad (3.2)$$

where p_a and p_b (p_i) are momenta of initial (final) state partons. The matrix element $\mathscr{M}_{ab\to X}$ represent sum of the contributions from Feynman diagrams to the final state, and it is evaluated with perturbative expansion in powers of the strong coupling constant α_s. The expansion is typically limited at leading order, as the higher order loop calculations require much more complicated processes such as renormalization. This does not imply calculations at the leading order level are trivial, as the number of associated Feynman Diagrams increase approximately factorially to the number of final state particles. The task of integrating over many dimensions of phase space is hence done by Monte-Carlo (MC) methods, as it provide excellent approximation with relative simplicity. The basic idea involves using a random number generator to obtain a value for each degree of freedom in the candidate events. Candidate events occur with the probability that is directly related to the differential cross section $d\sigma$, which is also referred to as the *event weight*. Averaging over high statistics of candidate event weights provides a good approximation to the phase space integral $\int d\sigma$, as well as converging to the actual cross section and eventually the corresponding detector response.

3.1.2 Parton Showering

The constituent partons of hadrons involved in hard scattering can accelerate colour-charged particles, which would emit QCD radiation (gluons), in a analogous way to the emission of QED radiation (photons) when electrically charged particles are accelerated. While the photons are electrically neutral, the gluons would behave differently as they are also colour-charged themselves, would cause further gluon emission. This phenomenon referred to as "Parton Showering", oc-

curs from the scales of hard scattering down to the hadronization level of typically a few GeV.

PDFs for cross section calculation needs to be known at a given scale. In reality they are often obtained at a different scale, and transformed with a set of evolution equations [82]. Similar types of equations can also be used to describe the underlying physics of parton showers, which can be applied recursively starting with resulting partons from hard scattering, evolving to the final colourless hadronic bound state. The basic pattern starts with a parton a produced at scale t' evolving to a new scale t, where $t < t'$ is the point which it decays into partons b and c, with certain kinematic properties and flavour. The probability for a each possible occurrence can be expressed as:

$$dP_a(x,t) = \frac{dt}{t}\frac{\alpha_s}{2\pi}P_{ca}(x)dx \tag{3.3}$$

where x is the momentum fraction of parton a carried by parton c, and P_{ca} is the branching function. The partial cross section for the exclusive process is given by the initial hard process LO cross section multiplied by $dP_a(x,t)$ for the corresponding branching. The probabilities for all possible branchings sum up to one, as the partial cross section of the subprocesses conserve with the LO cross section of the initial hard process.

The term "scale" is this context is used as a general representative term, as it can take different forms in various types of parton showers. They can have representations such as the angle between partons or the relative transverse momentum, but are all proportional to the branching invariant mass. Repeated occurrence of this process results in a parton branching cascade that is governed by QCD. The cutoff scale at the hadronization level defines a point where no more resolvable branchings can occur. The resulting final partons from successive branchings that propagate in similar directions are grouped into "jets", which is the point where hadronization occurs.

3.1.3 Hadronization

As coloured charged particles have yet been observed to exist isolated in nature [83], a suitable mechanism needs to be put in place to convert these loose coloured particles into colour-neutral hadronic bound states. This process referred to as hadronization, is long distance with low momentum transfers, where non-perturbative QCD effects become important. As there are currently no analytical descriptions of the mechanism that provide qualitative results, only phenomenological models are used in the simulation of these transitions. They are usually based on qualitative ideas such as *Local parton-hadron duality*, which define the approximate model boundaries. The finer details are all described by parameters set from extensive comparison with experimental data. There are two main types of models used [84]:

- **Cluster Model**: Based on ideas of $Preconfinement$ [85]. Remnant gluons from the parton shower form $q\bar{q}$ pairs, and form colour neutral clusters along with other remnant quarks. These clusters typically have invariant mass at the hadronization scale, and they either transform into final state hadrons or decay isotropically into lighter hadrons.

- **String Model**: Based on ideas of $Linear\ confinement$. Quark-antiquark pairs are considered to be confined with a connected string, and increasing linear separation will increase the potential to the string, analogous to rubber bands. The string breaks up into hadrons when the separation becomes more energetically favourable for a $q\bar{q}$ pair to be created, via quantum tunnelling somewhere along the string, resulting in two $q\bar{q}$ pairs connected by string.

and their basic concepts are shown in Figure 3.1.

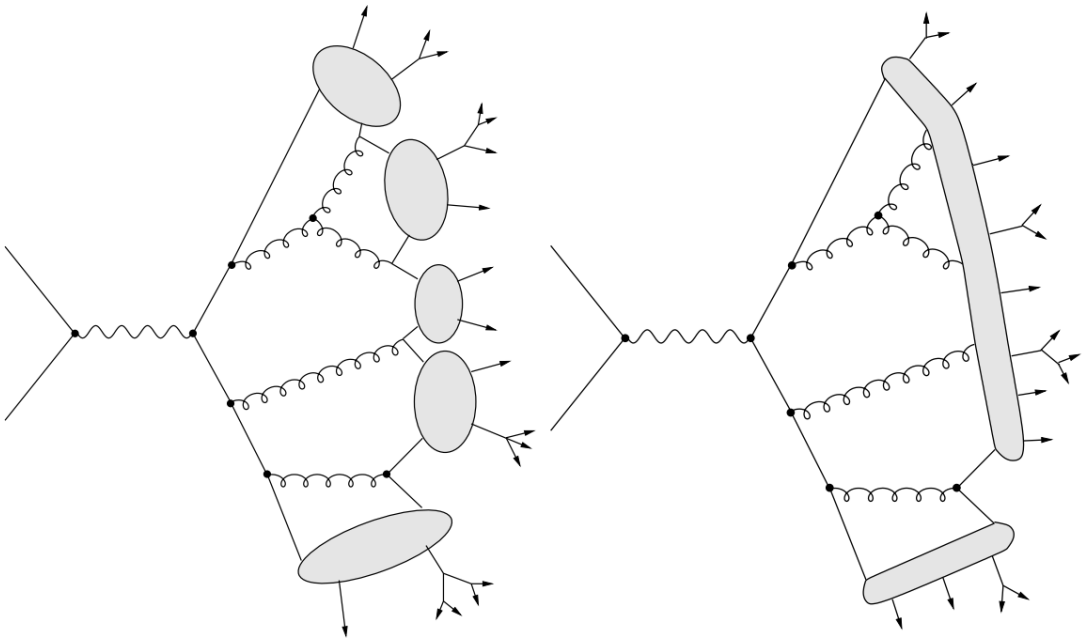

FIGURE 3.1: Illustrations of the concepts behind the Cluster (left) and the String (right) models [84]

Independent of the models, most hadrons emerged from hadronization will experience further decays. Whether a particle is considered stable or not is usually defined by the experiment, using a certain mean lifetime as the definition threshold. Particles with mean lifetime below the threshold typically decay before exiting the detector, and hence require consideration in Monte-Carlo event samples. As the hadronic bound states and their various subsequent decays have a very high level of complexity, full evaluations of all matrix elements and integration over phase spaces is not possible. Phenomenological methods utilizing tables of particle decays and branching ratios from [86] are very common, to set occurrence rates of various final states containing different stable particles that are observable by the detector. It is also necessary to evaluate each observable final state independently, hence separate MC samples with each dedicated to a particular final state are generated for comparison with data.

3.1.4 Underlying Events

Undrelying Events are activities additional to primary hard scattering processes and its subsequent parton showering or hadronization during hadron-hadron collisions. They are assumed to originate mostly from Multiple Parton Interactions (**MPI**) of beam remnants, which are in general softer than the primary scattering process [82]. Their presence subsquently leads to an overall increase of measured activity, which may include larger sum of transverse energies. Reconstruction algorithms for identification of objects can also be affected, as these effects can occasionally lead to additional reconstructed jets.

The understanding of such activities are also important, and is currently estimated with phemenological models that are tuned to data. The average number of parton-parton collisions, which is proportional to the presence of underlying events, are both estimated in Event Generators in the evolution of the event.

3.2 Simulation and Detector Response

Along with the ability of event generators to simulate subatomic processes with properties and occurrence frequencies similar to nature, it is also important to predict the responsiveness of the detectors to the corresponding decay products. The GEANT4 (**GE**ometry **A**nd **T**racking) [87] toolkit is a software package within the ATHENA framework that is dedicated for simulating detector responses of various particles. It is utilized with a detail geometric model of the ATLAS detector to predict their interactions with the various detector materials, as well as the paths of outgoing particles through different detectors.

Four vectors of the particles resulting from the collisions are tracked through the entire detector system. Detector components in the geometric model of the detector are labelled as "active", and recording of information such as $\frac{dE}{dx}$ deposited in

different detectors are taken place. Particles also deposit energy in other "inactive" components such as the cryostats, which is also of great interest and is often cross checked using jet energy and E_T^{miss} distributions.

Simulated energy deposits from various detectors are converted to corresponding detectors outputs as expected from real collisions, via a process called *Digitisation*. The resulting output is equivalent to detector read out collected from real collisions, and is interfaced with the reconstruction algorithms discussed in the next Chapter. Such algorithms for reconstructing various physics objects such as leptons, hadronic jets and subsequently events, are applied on detector readouts both from simulation and collected from real collisions.

3.3 Data Formats

Information such as time of hits and the energy deposited from the detector read outs of are stored in Raw Data Object (**RDO**) formats. For Monte Carlo simulations, the information on truth objects as well as their associated simulation data prior to the detector read out stage are also stored. These information are absent in the equivalent real data files, which subsequently are much smaller in size per event. These RDOs are progressively saved to smaller formats of Event Summary Data (**ESD**), then to Analysis Object Data (**AOD**). ESDs and AODs are typically used for calibration purposes and physics analyses that require specific details of events. Derived Physics Data (**DPD**) formats that are further smaller in size are also produced from AODs by various physics analysis groups, for which only information relevant to the corresponding analyses are saved. These D3PDs[1] can be processed using ROOT [88] outside of the ATHENA framework. Various physics performance groups develop updated tools of different functions for these ROOT based analyses, such as applying calibration corrections as well as estimating systematic and statistical uncertainties.

[1] "3" represents the files are the third interpretation instance of the detector read out

Chapter 4

Reconstruction of Events

An event within the physics analysis framework of ATLAS represent a single collision of two particles, each colliding with the other from the oppositely circulating beam, as well as its evolution to the corresponding final state particles that are observed by the detectors. Reconstruction of such events include the task of identifying various physics objects such as leptons and hadronic jets from the detector read out information. This needs to be done with high level of accuracy, for understanding the collected data from real collisions via comparisons with MC simulations. For optimal consistency, such algorithms are applied on detector read outs from real collisions as well as MC simulations with full detector effects taken into account, including digitization. Identification algorithms described in this chapter do not represent the complete list. These selected algorithms reconstruct physics objects that are used for the analysis presented in this thesis.

4.1 Tracks

Tracks for various particles are reconstructed in the Inner Detector from the recorded hits at different space-time points, via a sequence of different algorithms [89]. High efficiency and accuracy for this task are important as the result provide momentum and charge information for physics analyses.

The *inside-out* tracking approach is a baseline algorithm designed to reconstruct the primary charged particles efficiently. Primary particles are defined as particles that are either directly produced from a pp interaction and have a mean lifetime

greater than 3×10^{-11} s, or produced either from subsequent decays or interaction of particles with a lifetime smaller than 3×10^{-11} s [90]. Their reconstructed tracks are also required to have $p_T > 400$ MeV. The reconstruction algorithm starts with the creation of global three dimensional representations, referred to as *SpacePoints*, using the two-dimensional local measurements from the Pixel Detector and SCT. Successful creation of three such points are used as seeds, and recorded hits are added to the track along the trajectory outward from the IP using a combinatorial Kalman filter [91]. The track fit is progressively updated with each additional hit, which enables the corresponding track extrapolation to locate the next expected hit along the trajectory more efficiently. Ambiguities of the resulting track candidates, which includes fake and partial tracks, are resolved by ranking them using their likelihood of being an actual trajectory of a particle, via evaluation of quality cuts [92]. The resolved tracks are then extended into the TRT for matching with possible compatible segments, without further progressive track fitting.

An *outside-in* approach is applied in the next stage. Segments reconstructed in TRT are extended inwards by adding hits recorded in the silicon detectors. This back tracking approach is powerful in locating additional track segments that are not discovered by the *inside-out* approach, possibly due to the lack of appropriate initial seeds. These reconstructed tracks are typically the trajectories of secondary particles, which are defined as particle produced from interactions of the primary particles. A global fit is applied in the final stage with information from all three detector layers. Hits from bad fits on the silicon detector track candidates are stored as outliers, along with reconstructed TRT segments with no corresponding matches in the silicon detectors.

Additional nearby hits due to pile-up effects can confuse the pattern recognition algorithms, which subsequently leads to increased fake tracks that cannot be associated with any primary or secondary particles. Quality fitting requirements to minimize the selection of muons reconstructed from fake tracks are described in Section 5.3.1.

4.2 Vertices

Reconstructed Vertices in the particle collision environment represent the spatial positions of particle interactions, which result in the creation of new particles. *Primary vertices* are defined as interactions of hadron collisions directly from the proton beams, whereas *Secondary vertices* are interactions of particles produced from primary vertices. Quality reconstruction of both vertex types are important for physics analyses, as their information coupled with reconstructed tracks contribute significantly in describing the evolutionary process from initial collisions to final state particles.

Primary vertices are reconstructed using a two stage iterative approach [93]: A primary vertex finding algorithm dedicated to match associated tracks to vertex candidates is first applied, then a primary vertex fitting algorithm is used to reconstruct the vertex position and its corresponding error matrix. These two stages can be summarized in the following steps:

- Preselecting reconstructed tracks that are compatible with an origin from the interaction region[1]
- Each track carries a weight that represents its compatibility with the fitted vertex, which depends on the χ^2 of the fit.
- Vertices are matched to interactions by the sum of weights from the associated tracks, which are also matched to the interaction.
- z coordinates of tracks are grouped into a distribution, and its global maximum is used as the vertex seed.
- The vertex seed position and its surrounding tracks are used as inputs to the *adaptive fitting algorithm* [94] to determine the vertex position. The

[1] Also referred as the *Beam Spot*. It represents the central luminous region where the hadron-hadron collisions take place. It is in the shape of a thin hair along the beam axis, stretching a few cms in length, whereas its dimensions in the transverse plane are in the order of μm.

algorithm is a χ^2 based fitting algorithm that progressively down weights the contributions from the outlying tracks to the χ^2 of the overall vertex.

- Tracks that are incompatible with a vertex by more than 7 σ are to seek a new vertex, and the entire process is repeated until no further vertices are found.

Additionally a very loose constraint of $\chi^2 < 49$ is imposed to prevent single vertices splitting into two due to nearby outlying tracks. The *Beam Spot* is also used as a constraint to reduce vertices with very few associated tracks, as direct hadron-hadron interactions typically have more associated tracks and high transverse momenta.

Pile-up effects can also lead to reconstruction of fake vertices from fake tracks, where a fake vertex is defined as vertices with leading contributions from fake tracks [90]. As luminosity increases, so do the average number of visible pp interactions per bunch crossing, denoted as μ. These multiple interactions are typically spaced longitudinally along the beam axis, as shown in Figure 4.1. If two interactions are spatially too close, they can confuse the algorithm and only a single vertex is reconstructed. This effect can become significant as μ increases, the vertex reconstruction efficiency can decrease down to $\approx 50\%$ at $\mu = 40$. To compensate for these effects in the collected data, distributions of μ from the MC samples are fitted to data by performance groups for physics analyses.

Secondary vertices represent interactions such as heavy flavour decays, long-lived hadron decays or photon conversions. They are typically reconstructed by imposing kinematic constraints, such as mass values of the parent and decay particles for such interactions from hypothesis, on the fitting between displaced tracks and the vertex candidate [95]. Direct constraints on track parameters derived from variables such as angular separation are used in the case of converted photons.

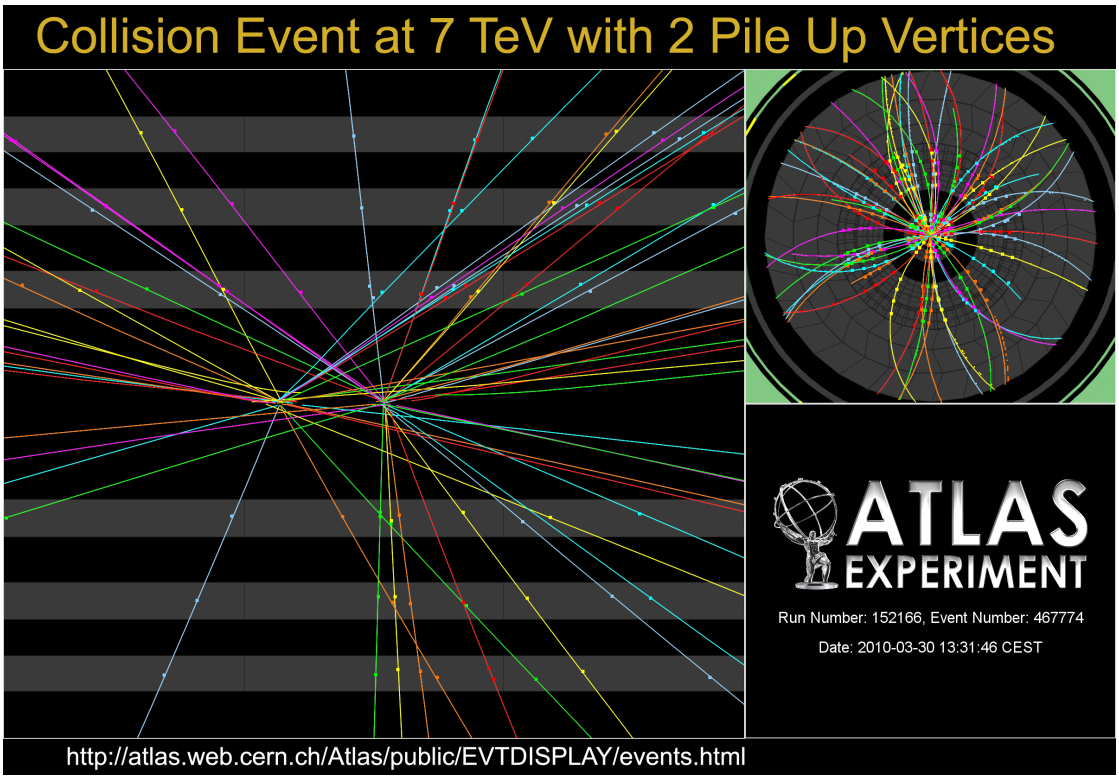

FIGURE 4.1: A pileup event recorded by the ATLAS detector on 30th March, 2010 with two reconstructed vertices, © CERN 2013.

4.3 Muons

Muons can emerge as one or multiple of final state particles from many interactions that are possible from the hadron-hadron collisions inside ATLAS. Multiple detectors installed in ATLAS were designed with the ability to detect muons. Different algorithms are used to reconstruct muon tracks in corresponding systems, as well as combining measurements from multiple detectors. Muons reconstructed with different measurements can be categorized into these types [96, 97]:

- **Standalone muons**: Trajectories are reconstructed using hits recorded only in the MS. The associated impact parameter as well as the direction of flight are determined by extrapolating the track back to the beam line. Momen-

tum values measured are corrected to determine the initial momentum at the interaction point by considering the parametrized energy loss in the calorimeters.

- **Combined muons**: Tracks of standalone muons are combined with compatible tracks from the Inner Detector.
- **Segment tagged muons**: Inner Detector tracks are extrapolated into the Muon Spectrometer, they are identified as a muon track if a compatible segment in the precision muon chambers is found.
- **Calorimeter tagged muons**: A reconstructed track in the Inner Detector is considered to be a trajectory of a muon if its extrapolation into the calorimeters matches an associated energy deposit that is compatible with the hypothesized minimum-ionizing particle.

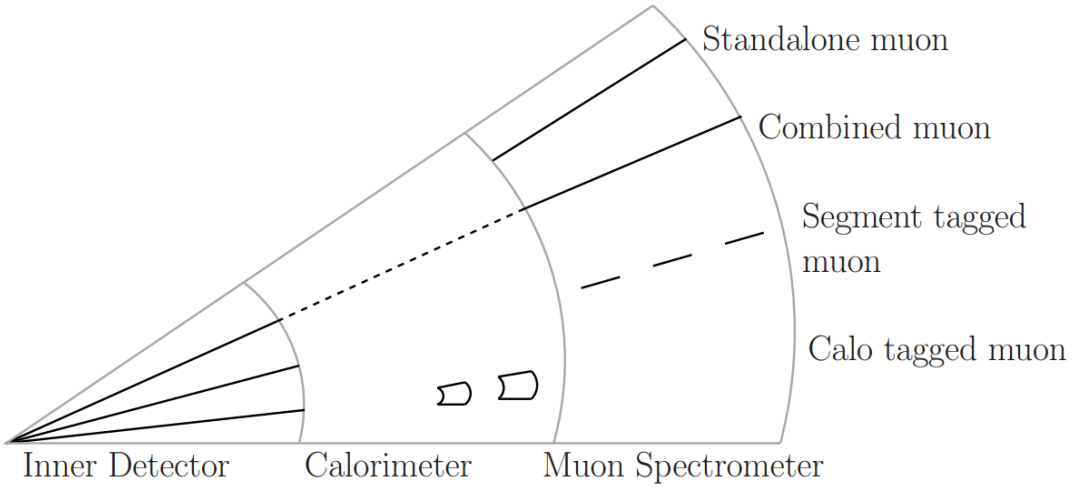

FIGURE 4.2: Different types of reconstructed muons: Standalone, Combined, Segment-tagged and Calorimeter-tagged [98].

These different types of muons are shown schematically in Figure 4.2. Algorithms used for reconstructing these types of muon objects can be categorized into two families with very similar performance in efficiency and resolution: `STACO` (STAtistical COmbination) and `MuID` (Muon ID). There is a dedicated algorithm from

each family to reconstruct each of the four different muon object types. The STACO algorithm will be explored more in detail in this section, as it is used in this analysis [92].

Standalone muons in the MS are reconstructed by first using the information from the RPC and TGC chambers to identify "regions of activity", which are typically in units of $\delta\eta \times \delta\phi \approx 0.4 \times 0.4$. Nearby trigger chambers provide the ϕ coordinate of hits when reconstruction initiates in the precision chambers. Straight line track segments are fitted when pairs of hits from either the same or adjacent chambers are found. These straight track approximations are good at this scale, and are kept if they contain sufficient hits as well as pointing approximately at the IP. They are then extrapolated to adjacent stations, and matched to compatible segments if they are consistent with momentum hypotheses in toroidal magnetic fields. Tracks with at least two segments are globally refitted with the initial measurements that produced the straight track approximation. Track candidates with a good χ^2 value are considered to be reconstructed muons, and are back-tracked towards the IP.

Combined muons are reconstructed via statistically matching Standalone muons from the MS with compatible ID tracks, by means of their covariance matrices. Each MS and ID track is parametrized into vectors P_1, P_2 and covariance matrices C_1, C_2 for matching. The corresponding vector of the combined track is given by the solution of the following equation:

$$(C_1^{-1} + C_2^{-1}) \times P = C_1^{-1} \times P_1 + C_2^{-1} \times P_2 \tag{4.1}$$

and its covariance matrix is given by:

$$C = (C_1^{-1} + C_2^{-1})^{-1} \tag{4.2}$$

with the corresponding χ^2 value is determined by:

$$\chi^2 = (P - P_1)^T \times C_1^{-1} \times (P - P_1) + (P - P_2)^T \times C_2^{-1} \times (P - P_2) \quad (4.3)$$

Corrections for energy losses in the calorimeters and ID are applied, accounting for multiple scattering. Reasonable combinations of MS-ID track pairs at their closest approach to the beam line in the $\eta - \phi$ plane are collected, and only combined tracks with global χ^2 values below a set threshold ($\chi^2 < 50$ [99]) are accepted. The pair with the best χ^2 value is retained if multiple combinations are possible, and the corresponding tracks of the retained pair are removed from the list of tracks for matching. This process is repeated until there are no more possible combinations [62].

4.4 Jets

Jets are showers of particles emerging from the hard scattering process. They are defined by the output of the algorithms that are designed to categorize them, which the algorithms take energy depositions from the calorimeters in the ID as inputs. They represent final state hadronic particles that are produced from the hadron-hadron collisions. The "anti-kt" algorithm [100] is used in ATLAS by default for reconstructing jets, as the resulting jets provides good approximation of the original parton's momentum. It also has good performance in providing "Collinear Stability[2]" and "Infrared Stability[3]" during the reconstruction process.

The topological cluster algorithm [101] is used to identify energy deposited from passing particles in the calorimeter over the background noise from electronic read-outs, which appear as energy clusters. The identified clusters are used as inputs to the anti-kt algorithm, in which two important distances are defined:

[2] *Collinear Stability*: The output is still stable if any constituent in the jet are replaced with two objects with the same momentum direction and half the initial energy.

[3] *Infrared Stability*: The output is still stable if very soft radiation are emitted between jets.

$$d_{iB} = k_{T_i}^{2p} \tag{4.4}$$

$$d_{ij} = min(k_{T_i}^{2p}, k_{T_j}^{2p}) \frac{\Delta R_{ij}^2}{R_C^2} \tag{4.5}$$

where $\Delta R_{ij} = \sqrt{\Delta\eta_{ij}^2 + \Delta\eta_{ij}^2}$ represents the distance in $\eta - \phi$ space between the objects i and j, and k_{T_i} is the transverse momentum of the object i. The parameter p is a measure of the relative power of the energy against the geometrical scales (ΔR_{ij}), and the anti-kt algorithm uses p = -1. The *Characteristic Radius* R_C determines the final size of reconstructed jets, with typical values of either 0.4 or 0.6 used in ATLAS. These defined quantities d_{ij} and d_{iB} represent the distance between the object i and j, and between object i and the beam, respectively. Figure 4.3 shows an example of jet clusters reconstructed by the anti-kt algorithm.

The algorithm then determines the smallest value of all calculated distances. Object i and j are combined into a single object and the distance is re-calculated if d_{ij} is the smallest. Object i is identified to be a *jet* if d_{iB} is the smallest value, and object i is removed from the searching loop over the remaining objects. This process continues until all objects are identified as jets.

4.5 Electrons

The standard reconstruction of electrons in the central region $\mid \eta \mid < 2.47$ begins with identifying energy clusters of longitudinal towers in the middle layer of the EM calorimeter by the *sliding-window algorithm* [102]. Clusters with transverse energy $>$ 2.5 GeV are used as seed, and a compatible track that is not created by photon conversion is searched for in the ID. Such tracks in the ID are extrapolated back to the EM calorimeter, and must match the cluster within a window of 3×5 in

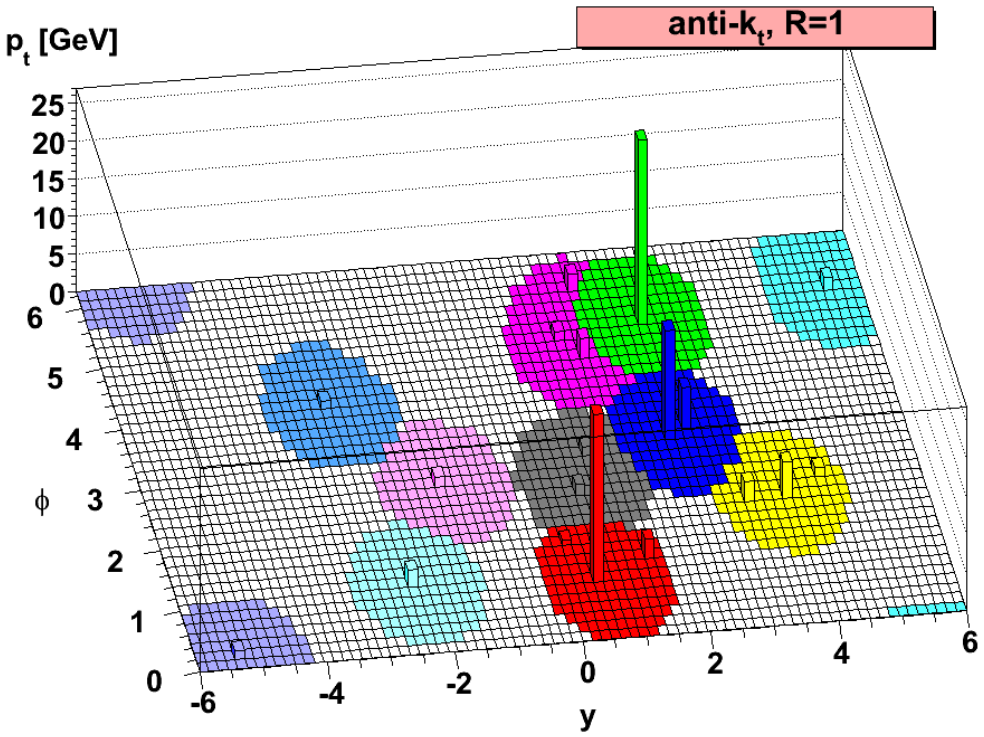

FIGURE 4.3: Jet clusters reconstructed in a MC simulation event using the anti-kt algorithm with $R_C = 1$. Few clusters with high p_T as well as a few softer clusters, distributed in the rapidity y and azimuthal angle ϕ [100].

units of $\Delta\eta \times \Delta\phi = 0.25 \times 0.25$. An electron is reconstructed if at least one track is compatible with the identified cluster. Tracks with silicon hits are given priority if multiple tracks are compatible, and the track with the smallest ΔR value between the track candidate and the cluster is chosen.

The electron cluster is then rebuilt with $3\times7(5\times5)$ units of cells in the barrel (endcap) region, and the cluster energy is determined by combining these four contributions:

- Estimated energy deposition in the material before the EM calorimeter
- Measured energy deposition in the cluster

- Estimated energy deposition outside of the cluster, commonly referred to as *lateral leakage*
- Estimated energy deposition beyond the EM calorimeter, commonly referred to as *longitudinal leakage*

The four momentum of the reconstructed electrons are determined using information from the best matched track and the final rebuilt cluster. The cluster energy is used as the electron's energy, and the η and ϕ directions are determined using parameters from the associated vertex.

Electrons are identified using three cut-based definitions involving calorimeter and tracking variables, in order to separate isolated and non-isolated signal electrons, background electrons from photon conversions and fake signals caused by jets. The three definitions of *loose*, *medium* and *tight* with increasing rejection criteria are used for different tasks. More detailed information on these definitions are listed in [102].

4.6 Missing Transverse Energy

Despite the success of the ATLAS detector system, there are still particles in nature such as neutrinos (as well as many theorized particles) that can escape without leaving any traces in the detector, due to their incredibly small interacting cross sections. They are accounted for by constructing the *Missing Transverse Energy* E_T^{miss} quantity of the event, for which the task is based on the conservation of transverse momentum. From the momentum convervation principle, the sum of momentum vectors from all physics objects in the transverse plane for each event should theoretically be zero, any momentum imbalance measured is regarded as the presence of neutrinos. There are also potential contributions from the imperfect measurements of particles in various detectors.

The E_T^{miss} quantity of the event is constructed with contributions from the calorimeters and the Muon Spectrometer. Its value and azimuthal angle are defined as [103]:

$$E_T^{miss} = \sqrt{(E_x^{miss})^2 + (E_y^{miss})^2}, \qquad \phi_T^{miss} = arctan\Big(\frac{E_y^{miss}}{E_x^{miss}}\Big) \tag{4.6}$$

where $E_{x(y)}^{miss} = (E_{x(y)}^{miss,calo}) + (E_{x(y)}^{miss,\mu})$ are the orthogonal components of E_T^{miss} in the transverse plane. The calorimeter terms are defined as:

$$E_x^{miss,calo} = -\sum_{i=1}^{N_{cell}} E_i sin\theta_i cos\phi_i, \qquad E_y^{miss,calo} = -\sum_{i=1}^{N_{cell}} E_i sin\theta_i sin\phi_i \tag{4.7}$$

where E_i, θ_i and ϕ_i are respectively the energy, polar and azimuthal angle of cell i over the range $\mid \eta \mid < 4.5$. In order to supress contributions from noise, the E_T^{miss} sum only includes cells from topological clusters to minimize the background noise, where the topological clusters are seeded by cells with $\mid E_i \mid > 4\sigma_{noise}$[4]. The sum from these clusters are calibrated according to the high p_T reconstructed physics objects that they are each associated to. Cells in topological clusters that are not associated with any physics objects are included with a global calibration.

The muon terms ($E_{x(y)}^{miss,MS}$) are determined with muon tracks recorded within the range of $\mid \eta \mid < 2.7$:

$$E_{x(y)}^{miss,\mu} = -\sum_{selected\ muons} p_{x(y)}^{\mu} \tag{4.8}$$

[4] σ_{noise} is the Gaussian width of the cell energy distribution away from the clusters, measured in randomly triggered events.

To minimize the contribution from fake muon tracks, only MS muon tracks that are matched to ID tracks are considered in the range $| \eta | < 2.5$. The p_T of isolated muons are determined with contributions from both MS and ID, and the energy loss in the calorimeter is not considered to avoid double counting. As the energy deposited in the calorimeter by non-isolated muons cannot be separated from the associated jet, the MS measurement of p_T after energy loss in the calorimeter is used. The combined measurement minus the estimated energy loss in the calorimeter is used instead, if there is a significant mis-match between the MS and combined measurement. For the range $2.5 < | \eta | < 2.7$ which is outside of the ID acceptance, only the MS measurement of p_T is used for both isolated and non-isolated muons. Although the muon contributions do not dominate the resolution of E_T^{miss}, any non-reconstructed, mis-measured or fake objects, including muons and jets, can also lead to large fake E_T^{miss}.

Chapter 5

Searching for Leptoquarks

Second generation scalar leptoquarks are predicted to be produced in pp collisions, and they can decay into a final state of two muons and two quarks, $pp \to LQ\overline{LQ} \to \mu^-\mu^+q\bar{q}$. A search for such leptoquarks with this final state has been performed and is presented of the remainder of this thesis. The general approach starts by selecting the appropriate datasets and simulated samples, and by applying kinematic selection criteria to physics objects and events according to the topology of the final state. Control Regions are also defined for each of the two major backgrounds, to validate their modelling as an orthogonal subset of the main selection. A frequentist approach is used in the end to test the hypothesis.

5.1 Data and Simulated Samples

The presence of pair produced, second generation scalar leptoquarks from a pp collision event would result in a signature of two muons and two hadronic jets detected by the ATLAS system. However many well understood interactions within the SM framework such as the production and decay of Z bosons can also produce the same signature. The production cross sections of such interactions are much larger compared to the production of LQs. This overwhelming presence of fake LQ signatures act as a huge background while analysing the detector responses. In order to understand the data collected by the detectors comprehensively, accurate representations of the contributions from these background processes are needed for extensive comparisons. Monte-Carlo samples (as discussed in Chapter 3) are produced to represent various well understood interactions within the SM, as well

as the production and decay of the LQs for different values of mass.

5.1.1 Data Samples

This analysis uses all of the datasets recorded by the ATLAS detector during the 2012 run of proton-proton collisions at $\sqrt{s} = 8$ TeV. The collected data are divided into Periods A-L, and further into individual runs that are numbered, as described in Section 2.2.7. The run ranges with their respective integrated luminosities are displayed in Table 5.1.

Data Period	Run Range	Integrated Luminosity (pb^{-1})
A	200804 - 201556	794.017
B	202660 - 205113	5094.68
C	206248 - 207397	1406.02
D	207447 - 209025	3288.39
E	209074 - 210308	2526.28
G	211522 - 212272	1274.81
H	212619 - 213359	1444.93
I	213431 - 213819	1016.26
J	213900 - 215091	2596.34
L	215414 - 215643	839.765
TOTAL		20281.4

TABLE 5.1: The data samples used in this analysis are shown in this table in their respective data periods and run ranges when recorded. The integrated luminosities for respective data periods are also shown.

A Good Runs List (**GRL**) is compiled to filter out luminosity blocks or even entire runs that do not meet the data quality requirements [104], keeping only the data recorded when all detectors are operating at nominal conditions for analysis ($\mathscr{L}_{int}$ = 20.3 fb^{-1}). The official general good run list (All_Good)[1] [105] is applied.

[1] `data12_8TeV.periodAllYear_DetStatus-v61-pro14-02_DQDefects-00-01-00_PHYS_StandardGRL_All_Good.xml`

5.1.2 Monte-Carlo Samples

The signal and most of the relevant SM background processes in this analysis are represented by Monte Carlo simulated samples produced with the ATLAS simulation infrastructure [106] within the ATLAS `mc12a` production campaign [107]. The events in the MC samples representing the LQ signals at each LQ mass point (600-1300 GeV, at 50 GeV intervals) are generated using `PYTHIA 8.165` [108] together with the ATLAS Underlying Event Tune `AU2` [109]. This event tune is applied simultaneously to a group of parameters within `PYTHIA` and are validated against data, where they represent the true uncertainties from physics aspects that cannot be obtained from first principles. This same combination of `PYTHIA 8.165` and `AU2` are also used to generate multijet events. The MC samples used to represent the two major backgrounds $Z + jets$ ($Z/\gamma^* \rightarrow \mu\mu$, $Z/\gamma^* \rightarrow \tau\tau$ and Drell-Yan $\rightarrow \mu\mu$) and $t\bar{t}$ processes are all generated with `SHERPA 1.4.1` [110]. In particular the samples generated for the Drell-Yan $\rightarrow \mu\mu$ processes were generated with the massive c, b treatment instead of the conventional massless treatment [111]. MC Samples representing the smaller background contributions from the WW, WZ and ZZ diboson events are generated with `HERWIG 6.52` [112] with the `AUET2` [113] MC tune. Samples of single top-quark events in the Wt and s-channel are generated with `MC@NLO 4.01` [114, 115, 116] with the `AUET2` MC tune, while the hadronization and parton showering in these samples are done by `HERWIG 6.52` coupled with `JIMMY 4.31` [117] for multiple parton interactions. The t-channel samples of the single top-quark events are generated with `AcerMC 3.8` [118] interfaced with `PYTHIA 8` with the `AUET2B` [119] MC tune. The $W + jets$ samples are produced with `ALPGEN 2.14` [120] interfaced with `JIMMY 4.31`, also with the `AUET2` MC tune applied. Choice of Parton Distribution Functions used to produce these MC simulated samples is generator dependent: `AcerMC`, `PYTHIA`, `HERWIG` and `ALPGEN` use `CTEQ6L1` [121], while `MC@NLO` uses `CT10` [122].

Each of the MC samples used in the analysis are produced with a specified high

number of events, with a balance between high statistics for robust analysis and required computation resources. They are scaled appropriately for data comparisons with respect to the total number of events $N_{MC\ Events}$ in the sample, the cross section σ of the corresponding interaction as well as the total integrated luminosity $\mathscr{L}_{int}$ of the collected data it is compared to, in the following way:

$$SF_{MC} = \mathscr{L}_{int} \times \frac{\sigma \times BR \times \epsilon_{Filter}}{N_{MC\ Events}} \tag{5.1}$$

where BR is the branching ratio and ϵ_{Filter} is the filter efficiency of the event. Application of such scale factors to corresponding MC samples transforms their contribution into a representative fraction when compared to collected data, or effective luminosity. Table 5.2 displays a list of samples used with their corresponding values of $\sigma \times BR$, ϵ_{Filter} as well as their effective luminosity. Various adjustments are applied to compensate for differences with data caused by known issues, as described in Section 5.2. Further normalisation scaling are applied to the $Z + jets$ and $t\bar{t}$ samples in defined control regions using well understood SM interactions as described in Section 5.6.3.

5.2 Corrections for MC Simulations

Inadequacies of theoretical models in predicting events (as discussed in Section 3.1) combined with detector effects (such as transformed geometry under stress) leads to differences between MC samples and collected data. Techniques are developed at the software level to appropriately correct for such effects with known causes.

Sample	Request ID	$\sigma \times BR$ (pb)	Event Filter Efficiency	Effective Lumi (fb^{-1})
$\gamma* \to \mu\mu$ (120 GeV $< M_{ll} <$ 180 GeV) + 4 jets	180767	9.95	1	4.28
$\gamma* \to \mu\mu$ (180 GeV $< M_{ll} <$ 250 GeV) + 4 jets	180768	1.6	1	24.91
$\gamma* \to \mu\mu$ (250 GeV $< M_{ll} <$ 400 GeV) + 4 jets	180769	0.57	1	66.87
$\gamma* \to \mu\mu$ (400 GeV $< M_{ll} <$ 600 GeV) + 4 jets	180770	0.09	1	376.89
$\gamma* \to \mu\mu$ (600 GeV $< M_{ll} <$ 800 GeV) + 4 jets	180771	0.02	1	2.06×10^{3}
$\gamma* \to \mu\mu$ (800 GeV $< M_{ll} <$ 1000 GeV) + 4 jets	180772	4.28×10^{-3}	1	7.78×10^{3}
$\gamma* \to \mu\mu$ (1000 GeV $< M_{ll} <$ 1250 GeV) + 4 jets	180773	1.54×10^{-3}	1	2.08×10^{4}
$\gamma* \to \mu\mu$ (1250 GeV $< M_{ll} <$ 1500 GeV) + 4 jets	180774	4.50×10^{-4}	1	7.03×10^{4}
$\gamma* \to \mu\mu$ (1500 GeV $< M_{ll} <$ 1750 GeV) + 4 jets	180775	1.49×10^{-4}	1	2.11×10^{5}
$\gamma* \to \mu\mu$ (1750 GeV $< M_{ll} <$ 2000 GeV) + 4 jets	180776	5.31×10^{-5}	1	5.84×10^{5}
$\gamma* \to \mu\mu$ (2000 GeV $< M_{ll} <$ 2250 GeV) + 4 jets	180777	2.05×10^{-5}	1	1.51×10^{6}
$\gamma* \to \mu\mu$ (2250 GeV $< M_{ll} <$ 2500 GeV) + 4 jets	180778	8.18×10^{-6}	1	3.64×10^{6}
$\gamma* \to \mu\mu$ (2500 GeV $< M_{ll} <$ 2750 GeV) + 4 jets	180779	3.35×10^{-6}	1	9.08×10^{6}
$\gamma* \to \mu\mu$ (2750 GeV $< M_{ll} <$ 3000 GeV) + 4 jets	180780	1.40×10^{-6}	1	2.12×10^{7}
$\gamma* \to \mu\mu$ ($M_{ll} >$3000) + 4 jets	180781	1.01×10^{-6}	1	3.02×10^{7}
$Z/\gamma* \to \mu\mu$ (inclusive)	147771	1.24×10^{3}	1	6.18×10^{3}
$t\bar{t} \to$ LeptLept	117800	11.1	1	160.71
$t\bar{t} \to$ LeptTaulept	117801	11.1	0.35	152.96
$t\bar{t} \to$ TauleptTaulept	117802	2.78	0.12	159.42
$t\bar{t} \to$ LeptHad	117803	69.19	1	126.14
$t\bar{t} \to$ LeptTauhad	117804	11.10	0.65	152.51
$t\bar{t} \to$ TauleptHad	117805	34.76	0.35	146.54
$t\bar{t} \to$ TauleptTauhad	117806	2.78	0.46	157.52
$t\bar{t} \to$ HadHad	117807	108.82	1	50.4
$t\bar{t} \to$ HadTauhad	117808	34.76	0.65	141.67
$t\bar{t} \to$ TauHadTauhad	117809	2.95	0.42	2.41×10^{3}
WW	105985	54.60	0.38	113.68
ZZ	105986	7.27	0.21	161.67
WZ	105987	22.82	0.31	142.72
Single Top (s) $W \to e\nu$	108343	0.61	1	278.23
Single Top (s) $W \to \mu\nu$	108344	0.61	1	278.13
Single Top (s) $W \to \tau\nu$	108345	0.61	1	278.26
Single Top (Wt)	108346	22.37	1	78.76
Single Top (t) e	117360	9.46	1	27.05
Single Top (t) μ	117361	9.46	1	27.06
Single Top (t) τ	117362	9.46	1	26.48
$Z/\gamma* \to \tau\tau$ (inclusive)	147772	1.24×10^{3}	1	2.56×10^{7}
$W\mu\nu$ + 0p	107690	9.54×10^{3}	1	0.36
$W\mu\nu$ + 1p	107691	1.87×10^{3}	1	1.33
$W\mu\nu$ + 2p	107692	566.32	1	6.63
$W\mu\nu$ + 3p	107693	158.85	1	6.34
$W\mu\nu$ + 4p	107694	42.26	1	6.02
$W\mu\nu$ + 5p	107695	12.54	1	1.59
LQ 600 GeV	180366	2.38×10^{-2}	1	209.58
LQ 650 GeV	180367	1.33×10^{-2}	1	375.338
LQ 700 GeV	159798	7.65×10^{-3}	1	652.81
LQ 750 GeV	180368	4.46×10^{-3}	1	1.11×10^{3}
LQ 800 GeV	180369	2.66×10^{-3}	1	1.88×10^{3}
LQ 850 GeV	180370	1.61×10^{-3}	1	3.1×10^{3}
LQ 900 GeV	180371	9.88×10^{-4}	1	5.05×10^{3}
LQ 950 GeV	180372	6.13×10^{-4}	1	8.13×10^{3}
LQ 1000 GeV	180373	3.83×10^{-4}	1	1.30×10^{4}
LQ 1050 GeV	180374	2.42×10^{-4}	1	2.06×10^{4}
LQ 1100 GeV	180375	1.54×10^{-4}	1	3.24×10^{4}
LQ 1150 GeV	180376	9.87×10^{-5}	1	5.04×10^{4}
LQ 1200 GeV	180377	6.34×10^{-5}	1	7.87×10^{4}
LQ 1250 GeV	180378	4.09×10^{-5}	1	1.22×10^{5}
LQ 1300 GeV	180379	2.66×10^{-5}	1	1.83×10^{5}

TABLE 5.2: List of MC simulated samples used to predict the yields from the background and signal processes. Values representing the cross-section × branching ratio for each sample also includes their respective k-factors.

5.2.1 Pile-up Reweighting for Events

The LHC has been progressively increasing the instantaneous luminosity per bunch crossing since its stable operation to allow faster collection of statistics, as shown in Figure 5.1. Pile-up is a subsequent resulting side effect that requires new considerations while analysing the data.

As the instantaneous luminosity increases, the chances of soft interactions between constituent quarks and gluons besides the hard scattering also increases. This leads to two types of pile-up effects:

- *In-time pile-up*: Additional tracks and vertices can be formed to confuse the corresponding reconstruction algorithms.
- *Out of time pile-up*: The proton bunch spacing of 50 ns is shorter than the read out response time of some of the sub-detectors, which gives the probability for the overlapping of energy deposits from neighbouring events.

Both scenarios can affect the performance on the reconstruction of physics objects and events. The recorded event with in-time pile up as previously shown in Figure 4.1, reconstructed tracks from different vertices cross and the corresponding detector will only register a single hit. As the MC samples are often produced before and during data taking periods, information used for reweighting in the production of MC samples are hence only estimated from previous studies. Pile-up effects are studied through out the data taking periods, and reweighting information to additionally apply on MC samples for physics analysis are constantly updated. Reweighting scale factors for each event are calculated using the average number of interactions per bunch crossing $< \mu >$, where its distributions from the MC samples are fitted to data by performance groups for physics analyses.

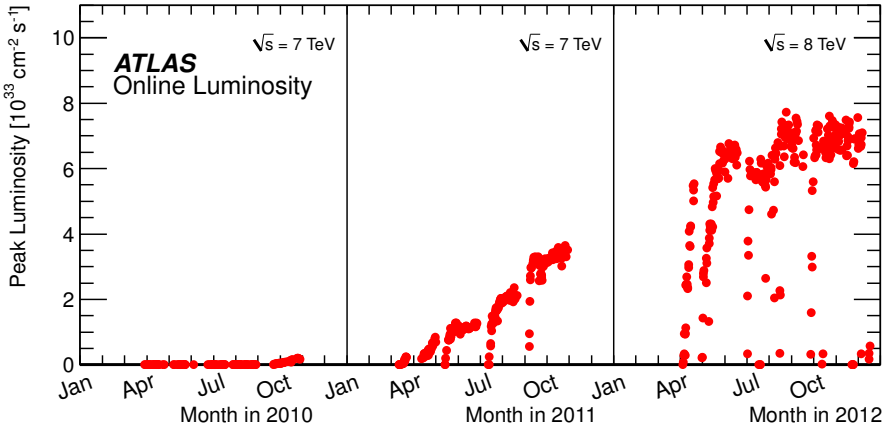

(A)

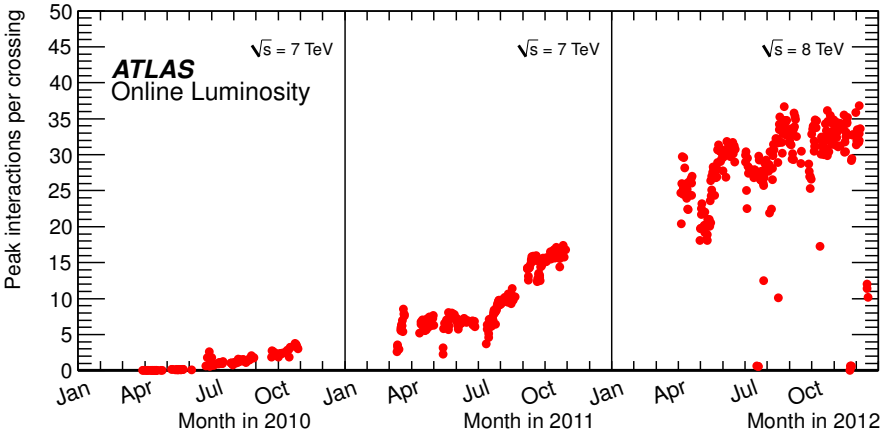

(B)

FIGURE 5.1: Figure 5.1a shows the peak instantaneous luminosity per day over the data taking periods from 2010 to 2012, while Figure 5.1b shows the average number of interactions per beam over the same time period. A positive correlation between the two is clearly visible.

5.2.2 Corrections for Muons

Several techniques have been developed by the Muon Combined Performance group (**MCP**) for various known aspects that can potentially contribute to differences of muon objects between MC samples and data. Each of these corrections independently provides compensation aspects such as imperfect modelling of muon momentum resolution in MC samples, and imperfect efficiencies of the muon trigger components.

Momentum Resolution

The realistic geometry of the ATLAS detector contains small deformations due to weight of the subdetectors installed. Optical alignment components are installed to monitor such effects, and the information is implemented in the geometrical model used to produce the MC samples. Small differences still exist between the real geometry and the MC geometrical model, as the coverage of the alignment system is not complete. Such discrepancies subsequently affects momentum resolution of muons, leading to the resolution modelled in the MC samples is mostly overly optimistic relative to the collected data. This discrepancy is estimated by applying a template fit to the distribution shape of the Z boson distribution that is obtained from MS and ID tracks in MC to match the data. Effect of this correction technique is shown in Figure 5.2.

Reconstruction Efficiency

The effective reconstruction efficiency of the muons is a combination from the independent reconstruction efficiencies in the ID and MS, as well as the matching efficiencies for the combined track using measurements from both components. This is determined using the $Z \to \mu^+\mu^-$ decay as a standard candle, and applying the tag and probe method [123]. Exactly two oppositely charged muon tracks

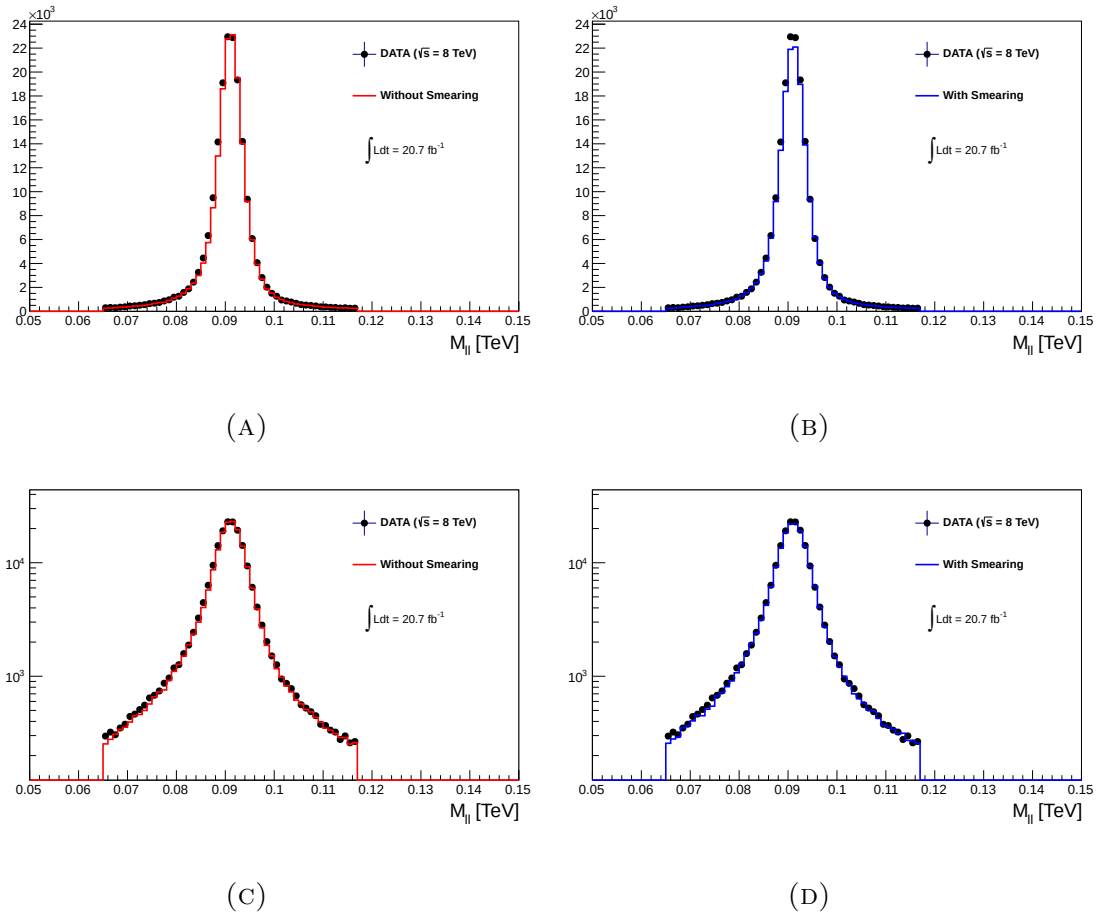

FIGURE 5.2: Dimuon invariant mass distributions in the $Z+jets$ Control Region (described in Section 5.5.1), showing the difference made by the smearing effect on the MC samples compared to data, around the Z boson mass peak.

with a dimuon invariant mass near the value of Z mass are selected. One of the muons is selected to be the "tag" muon, while the other acts as the "probe". The tag muon is required to be a combined muon in this case, and the probe muon has to be either a standalone muon reconstructed with measurements only from MS, or a muon with a track only from ID, depending on which efficiency is to be tested. The reconstruction efficiencies for the ID tracks are defined by the fraction of "MS probes" that can be associated with an ID track, and vice versa for the definition of MS track efficiency. The MCP group provides correction scale factors and associated systematic errors as functions of p_T, and it is at the order of 0.2%.

Trigger Efficiencies

During data taking, the task of detecting muons requires contributions from the muon trigger chambers described in Section 2.2.5, as well as the TDAQ system described in Section 2.2.7. Triggers are fired if the detected hit satisfy the requirements, and contributes to the data recording decision. The recorded hits are then processed *offline* with further tasks such as particle identifications and track reconstructions. Trigger matching is a process that aims to match a reconstructed track with an associate fired trigger. A fake trigger is defined as a trigger that fails to match a reconstructed track, which are understood to be mainly due to secondary particles. Similar to how the reconstruction efficiency is obtained, the tag and probe method with the Z mass distribution is used to determine the efficiency of the trigger [124].

5.2.3 Calibration for Jets

Energy deposited in the calorimeter cells by the particles produced in collisions are used to reconstruct jets. Detector effects such as noise thresholds and dead material in the calorimeter cause signal losses, and hence the energy of jets needs to be calibrated. *In situ* techniques are put in place to calibrate the *Jet Energy Scale* and *Jet Energy Resolution* [125]. Corresponding systematic uncertainties are also derived and will be discussed in Section 5.9.

Jet Energy Scale

Jets are essentially a bunch of particles produced from pp collisions travelling in a similar direction. Information such as the four vectors of the produced particles are stored in the MC samples, for which the simulated detector response can be compared to data. Calibrations are derived to restore the energy of the reconstructed jet in data to the energy at the particle level, referred to as **EM+JES**, as well

as accounting for detector effects. This is achieved by using the jet response in the calorimeter with respect to the truth particle jet in the MC samples, typically with $Z/\gamma^* + jets$ or dijet events. Calibration constants are derived in bins of p_T and η [126].

Jet Energy Resolution

Precise knowledge of jet resolution as well as good agreement between MC and data samples are important in the meansurements of jets. Two in situ techniques, the Di-jet balance method and the Bisector method, are used to measure the jet energy resolution. These methods determine corrections for issues such as particle level imbalance due to soft radiation, as well as track based and jet EM fraction corrections [127]. Uncertainties for both methods are also obtained, and the corresponding overall relative uncertainty is approximately 4% at $p_T = 500$ GeV. The agreement between MC and data are also with 4% up to $p_T = 500$ GeV for both methods [128].

5.3 Event and Object Selections

Recommendations from respective performance groups on selection criteria for quality physics objects that are relevant have been used in this analysis. These *preselected objects* are used to determine candidate events, as well as for studies in the control regions and on various systematic uncertainties. Candidate events are selected with requirements that are tailored to search for potential LQ processes, and only these events are used to derive the final result.

5.3.1 Muon Selection Requirements

The official Muon Combined Performance group (MCP) recommendations [129] for high p_T muons in release 17 and 2012 data was used as object selection criteria for muons, including a few quality requirements on the ID tracks

- Number of hits in the B-layer > 0, unless the track implies the muon has passed through an uninstrumented or dead region.
- Number of pixel hits + number of crossed dead pixel sensors > 0
- Number of SCT hits + number of crossed dead SCT sensors > 4
- Number of pixel holes + number of SCT holes[2]
- Successful extension into TRT in the expected region with η acceptance. Unsuccessful extension into TRT are classified as no associated TRT hit, or the associated hits are all outliers. The requirement is set as:
  - Let n_{TRT}^{hits} denote the number of TRT hits along the muon track, $n_{TRT}^{outliers}$ denote the number of outliers along the muon track, and $n = n_{TRT}^{hits} + n_{TRT}^{outliers}$
  - For $\mid \eta \mid < 1.9$: $n > 5$ and $n_{TRT}^{outliers} < 0.9n$
  - For $\mid \eta \mid > 1.9$: if $n > 5$ then $n_{TRT}^{outliers} < 0.9n$

In addition to the ID track requirements, the candidate muons considered are also required to be combined muons, as described in Section 4.3. The standard recommendation also suggest to have the primary vertex $\mid d0 \mid < 0.2$ mm and $\mid z0 \mid < 1.0$ mm for rejecting cosmic ray muons. Individual muons must have $p_T >$ 40 GeV and also pass the isolation requirement $p_T^{cone20}/p_T < 0.2$, where p_T^{cone20} is

[2] A "hole" is defined as an expected but absent measurement along the track

the sum of p_T of all the tracks within a cone of $\Delta R < 0.2$[3] of the muon track, excluding the contribution from muon p_T.

Recommended selection criteria for high p_T muons are additionally implemented, as muons with $p_T > 500$ GeV are significant in this analysis. Muons are required to register at least 3 hits (in each of the inner, middle and outer) stations of the MS, and at least 1 hit in 2 layers of the trigger chambers for optimal momentum resolution. The hit requirement at the inner station of the forward region corresponds to at least 2 hits in the Cathode Strip Chambers (CSC). These muons have p_T resolution at 1 TeV ranging from 10% to 25%, and are referred to as 3-station muons. For the central region $\mid \eta \mid < 1.05$, muons with at least 5 precision hits in each of the inner and outer stations are also selected in addition to the 3-station muons, and are referred as 2-station muons. These 2-station muons also require at least 1 hit in 1 layer of the trigger chambers, and have slightly worse resolution compared to the 3-station muons. The standalone momentum measurements from the ID and MS for each muon must also satisfy $|(\frac{q}{p})_{ID} - (\frac{q}{p})_{MS}| < 5(3)$ for the 3-station (2-station) muons. The intrinsic position resolution and effects of known misaligned chambers are included in the simulation, and muons passed through them are rejected.

5.3.2 Jet Selection Requirements

Jets are reconstructed from energy clusters detected in the calorimeter using the `AntikT4TopoEM` algorithm [130] and calibrated as described in Section 5.2.3. Jets used must satisfy $p_T > 30$ GeV and $\mid \eta \mid < 2.8$. Jets reconstructed in a cone $\Delta R < 0.4$ around one lepton (electron or muon) are removed. Additional "Jet Cleaning" criterion provided by the JetEtMiss group [131] are also applied to remove jets being identified from detector effects, with definitions for "ugly" and "bad" jets to be excluded from analysis.

[3] $\Delta R = \sqrt{(\Delta\phi)^2 + (\Delta\eta)^2}$

"Ugly" jets refer to real energy depositions in regions where the accuracy of its measurement is inadequate, i.e. the transition region between the barrel and end cap, as well as other problematic calorimeter regions. They are defined as:

- More than half of the energy is deposited in sensors located in the gap between the barrel and end cap components of the Tile calorimeter.
- More than half of the energy is from corrections at cell level for depositions in known regions with dead sensors.

"Bad" jets refer to reconstructed jets that do not associate to in-time energy depositions in the calorimeters. Definitions are set for their three main sources:

- **Noise spikes in the Hadronic Endcap Calorimeter (HEC)**:
  - More than half of the energy is deposited in HEC **AND** more than half of the energy deposited in the HEC cells have a large difference between predicted and measured pulse shape **OR**
  - Negative energy greater than 60 GeV
- **Coherent noise in the Electromagnetic Calorimeter**:
  - 95% of the jet energy is deposited in the EM calorimeter **AND**
  - Large difference between predicted and measured pulse shape for large fraction of the jet energy deposited in the LAr cells **AND**
  - $| \eta | < 2.8$
- **Non-collision backgrounds and cosmics**:
  - Less than 5% of the jet energy is deposited in the EM calorimeter **AND** $| \eta | < 2$ **AND** Less than 5% of the reconstructed tracks are associated with charged particles **OR**

- More than 5% of the jet energy is deposited in the EM calorimeter **AND** $|\eta| \geq 2$ **OR**
- More than 99% of the jet energy is deposited in a single calorimeter layer **AND** $|\eta| < 2$

Any reconstructed jet object that satisfy any one or more of these three definitions are considered as "Bad" jets. "Good" jets used for physics analysis are defined as neither "Bad" nor "Ugly".

5.3.3 Electron Selection Requirements

Electrons are selected by imposing *medium* conditions, similar to those defined in [132]. The electron clusters have to satisfy $E_T > 30$ GeV and $|\eta| < 2.47$. Electrons originating from clusters in the gap between barrel and endcap calorimeters ($1.37 < |\eta| < 1.52$) are also excluded. Electrons are also required to be isolated by imposing $E_T^{cone20} < 0.007 \times E_T + 5\ GeV$, where E_T^{cone20} is the transverse energy measured in the calorimeter within a cone of radius $\Delta R < 0.2$ around the electron direction, and E_T is the electron transverse energy. The term E_T^{cone20} is corrected to account for leakage (i.e. electron energy deposited outside the cluster) and pile-up effects. A smearing factor and a scaling factor are applied to electrons in simulated events, in order to correct discrepancies between real data and simulations.

5.3.4 Event Selection Requirements

Selection requirements for candidate events follow closely from the Second generation LQ results obtained with pp collisions at 7 TeV [41]. Candidate events require exactly 1 pair of opposite signed muons and at least 2 jets, and a primary vertex that has at least 3 associated tracks, with $p_{T,track} > 0.4$ GeV. If there are more than 1 qualified vertex in the event, the vertex with the biggest $p_{T,track}^2$ is used as

the primary vertex. Events must pass either the isolated single muon trigger with threshold $p_T > 24$ GeV or the non-isolated single muon trigger with threshold $p_T > 36$ GeV.

Single muons satisfying the requirements described in Section 5.3.1 are used to compose the pair of muons the event selection requires. If the pair of muons are opposite signed and both passing the 3-station requirement, the event is said to have passed the "tight muon" or "3+3" selection. A pair can be built up from one 3-station muon and one 2-station muon if no "tight muon" pairs are found in the event, these events are said to have passed the "loose muon" or "3+2" selection. A reweighting scale factor respective to each Monte-Carlo (both background and signal) samples due to pile-up corrections is also applied.

5.4 Definitions of Additional Observables

Besides the common kinematic variables such as E_T, p_T, η and ϕ, additionally constructed variables are used at different stages of the analysis. Quantities with large magnitude in events in the presence of massive particles are defined as follows:

- $L_T = p_T^{l_+} + p_T^{l_-}$: Scalar Sum of p_T of the two selected leptons
- $H_T = p_T^{j_1} + p_T^{j_2}$: Scalar Sum of E_T of the two leading jets
- $S_T = L_T + H_T$

Variables related to mass reconstruction are also defined:

- $M_{\mu\mu}$ - Dimuon invariant mass, mass component of the summed 4 vectors belonging to the two selected muons.

- M_{jj} - Di-jet invariant mass, mass component of the summed 4 vectors belonging to the two selected jets.

- $< M_{LQ} >$ - Average Leptoquark mass. Lepton-jet invariant mass values are constructed between the first(second) lepton with the (sub)leading jet. The two values from first lepton are compared with values from the second lepton, and a pair of values consisting one from each lepton, with the smallest difference between pairs with different leptons and jets from all four possible combinations are selected. The average leptoquark mass is the average of the two values in this selected pair.

Comparisons of distributions for these variables between SM background and LQ processes are shown in Figure 5.3. Their differences in shape and peak positions are useful discriminating data points potentially from LQ processes from SM backgrounds.

5.5 Control Regions

Control regions are used to validate the MC simulated representations of dominant backgrounds more closely. A control region for each of the two most dominant backgrounds, $Z + jets$ and $t\bar{t}$, are defined as orthogonal subsets to the main analysis, for validating the modelling in the MC simulated samples representing these SM interactions. Selection criteria on quality objects are chosen to maximize the contribution of the primary background over the others, as well as minimizing the contribution from the LQ signal. Normalisation scale factors for the $Z + jets$ and $t\bar{t}$ MC samples are also derived in their respective control regions, to further optimize their agreements with data. Definitions for each of the two control regions as well as for the nominal analysis are listed in Table 5.3.

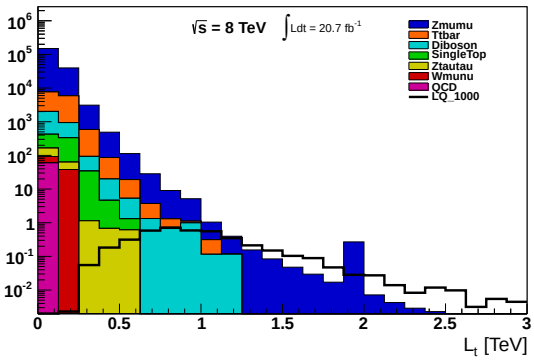

(A) L_T

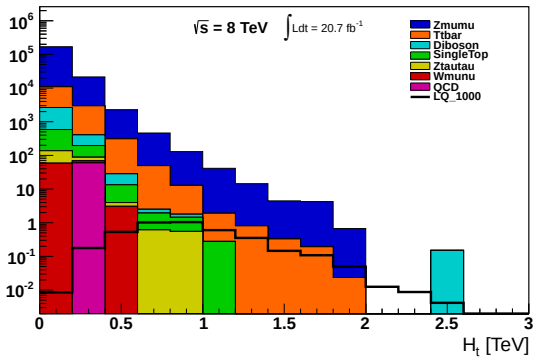

(B) H_T

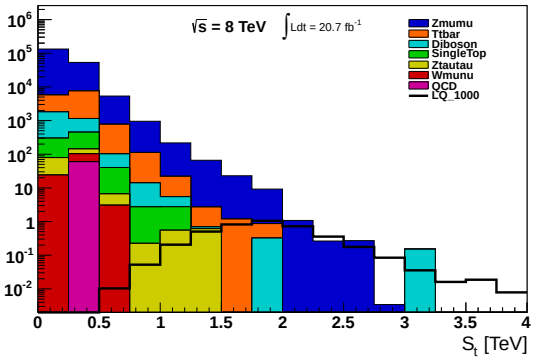

(C) S_T

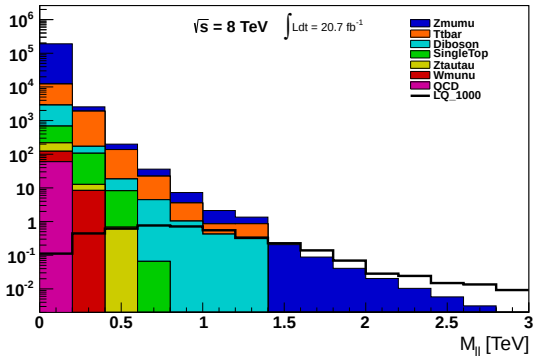

(D) $M_{\mu\mu}$

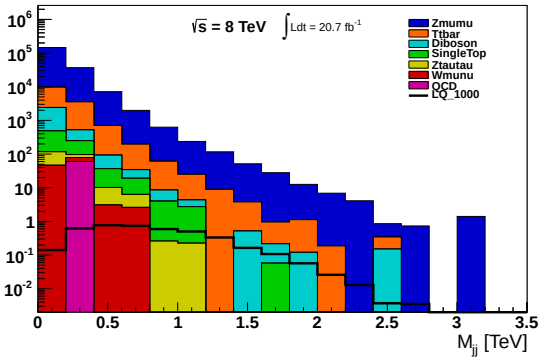

(E) M_{jj}

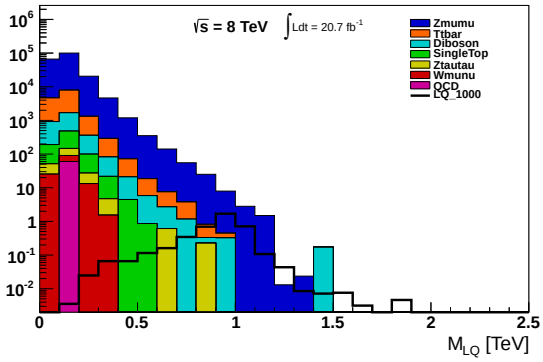

(F) M_{LQ}

FIGURE 5.3: Distributions of different key kinematic variables in the Event Selection region. Comparisons of MC samples between the LQ signal at 1000 GeV and SM background processes are displayed.

Nominal Event Selection	
1 pair of oppositely charged good muons At least 2 good jets At least one primary vertex with at least 3 associated tracks $p_{T,track} > 0.4$ GeV Passes (24 GeV isolated muon trigger) or (36 GeV non-isolated muon trigger)	
$Z + Jets\ CR$	$t\bar{t}\ CR$
$81 < M_{ll} < 101$ GeV	~~1 pair of oppositely charged good muons~~ Exactly 1 muon and 1 electron

TABLE 5.3: Selection criteria for the nominal analysis as well as the $Z + jets$ and $t\bar{t}$ control regions.

5.5.1 $Z + Jets$ Control Region

The $Z + jets$ control region is used to utilize the well understood Standard Model interaction of $Z/\gamma^* \rightarrow \mu\mu$ as an indicator to validate the MC samples with data. The invariant mass variable of two muons, $M_{\mu\mu}$, is hence a key variable for this separation, and its selection criteria are defined as the standard selections with an additional requirement of $81 < M_{\mu\mu} < 101$ GeV. Distributions of different key kinematic variables in this control region are shown in Figure 5.4.

5.5.2 $t\bar{t}$ Control Region

The $t\bar{t}$ control region uses the decay of top-antitop pairs that are produced from the proton-proton collisions. Semi-leptonic decay of the $t\bar{t}$ pair is another major background in this analysis, with the (anti)top quark decaying via the weak interaction into a W boson and a down type (down, strange, bottom) quark [133], and the W boson further decays leptonically into a lepton and a neutrino [86]. The selection criteria are defined as the same as the standard selections, but with exactly one electron and one muon instead of a pair of muons. Distributions of different key kinematic variables in this control region are shown in Figure 5.5.

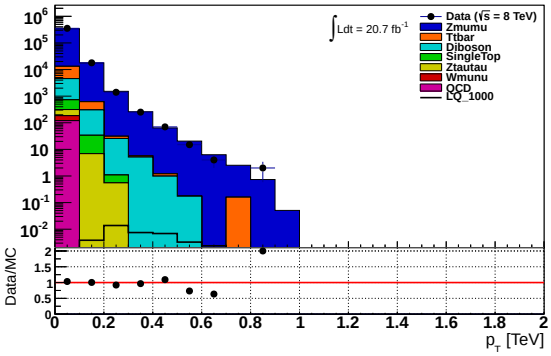

(A) Muon p_T

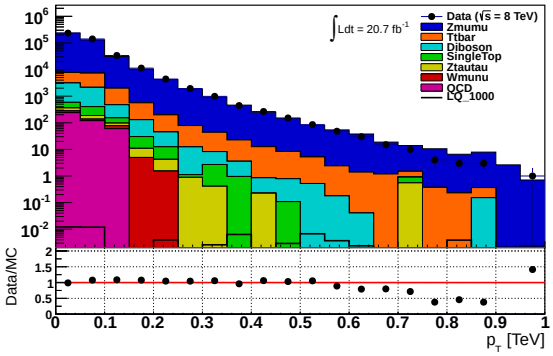

(B) Jet p_T

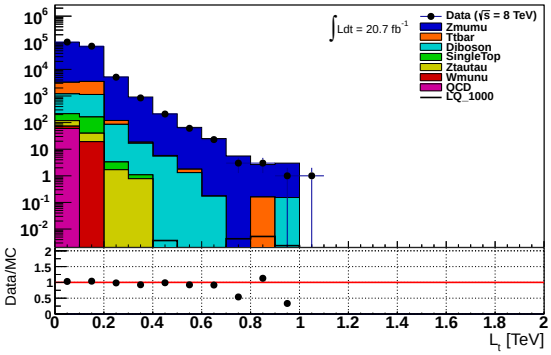

(C) L_T

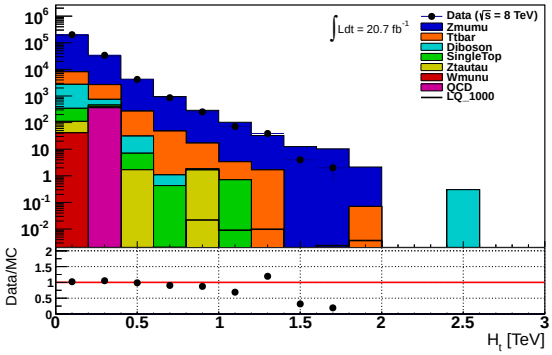

(D) H_T

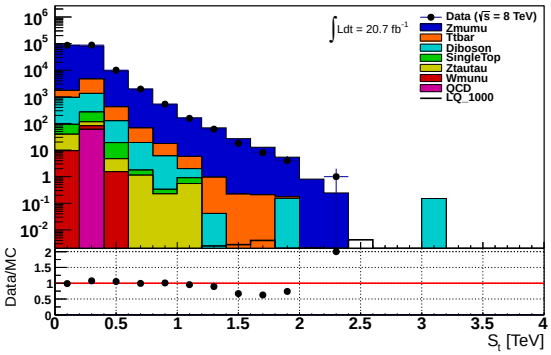

(E) S_T

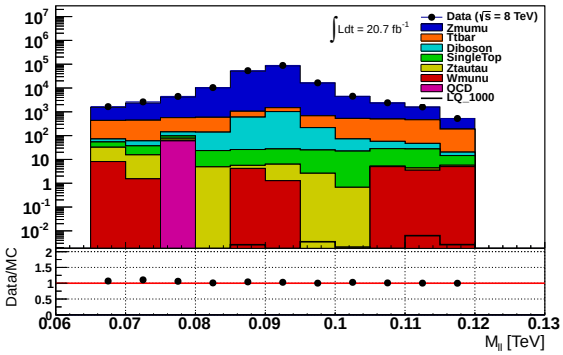

(F) $M_{\mu\mu}$

FIGURE 5.4: Distributions of different key kinematic variables in the $Z + jets$ control region. Disagreements in the high-end tails of the distributions are all statistical effects, at a relative insignificant scale of 10^1.

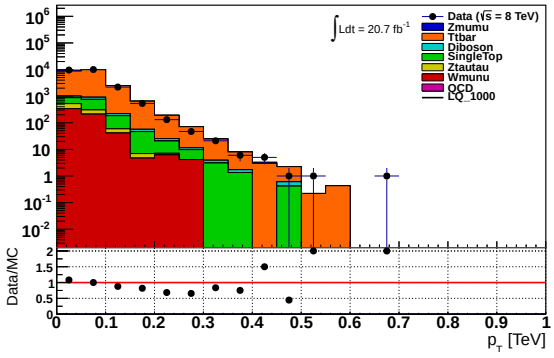

(A) Electron p_T

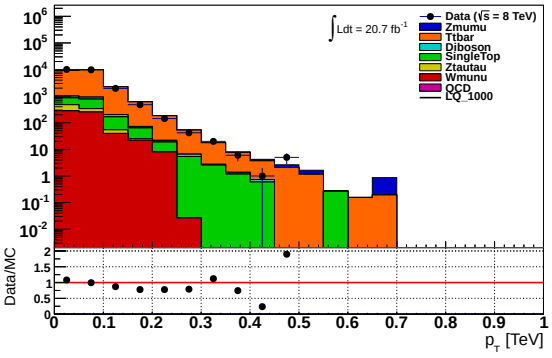

(B) Muon p_T

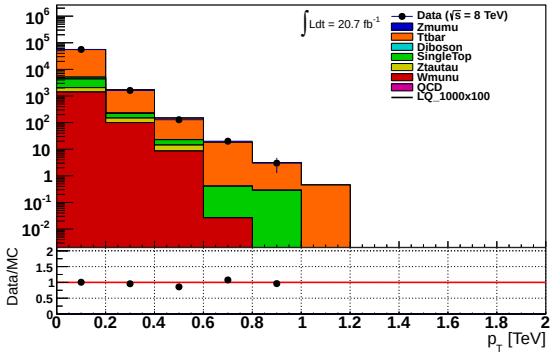

(C) Jet p_T

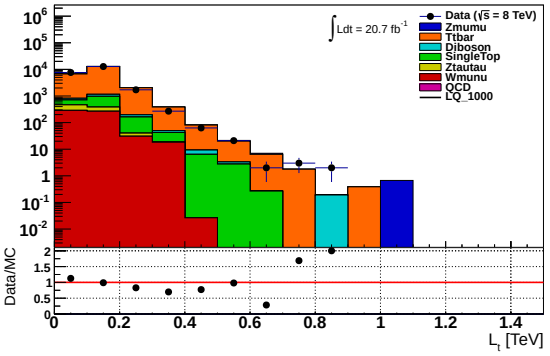

(D) L_T

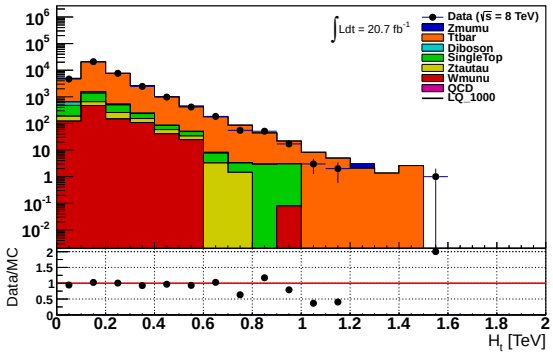

(E) H_T

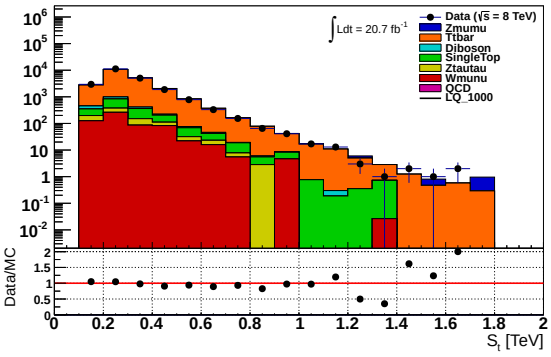

(F) S_T

FIGURE 5.5: Distributions of different key kinematic variables in the $t\bar{t}$ control region. Disagreements in the high-end tails of the distributions are all statistical effects, at a relative insignificant scale of 10^1.

5.6 Determination of Background Yields

Yields from all background processes except the Multijet background are determined using the MC simulated samples described in Section 5.1.2. The final yields are determined after the correction scale factors described in Section 5.2 as well as Section 5.6.3 are applied.

5.6.1 Simulated Backgrounds

The simulated backgrounds used in this analysis are listed in Table 5.2. Their acceptance and yields are determined with all of the analysis requirements listed in Section 5.3 applied to the simulated events, then multiplied by the respective scale factor calculated with Equation 5.1. Normalisation scale factors determined in the control regions described in Section 5.5, respectively for the samples representing the $Z + jets$ and $t\bar{t}$ processes, are also applied as described in Section 5.6.3.

5.6.2 Multijet Background

The contamination of multijet backgrounds for this analysis is determined using the data-driven Matrix Method [134]. This method utilizes Equation 5.2 to determine the probability that the muons selected in the final stage of the analysis being misidentified muons from jets:

$$\begin{bmatrix} N_{TT} \\ N_{TL} \\ N_{LT} \\ N_{LL} \end{bmatrix} = \begin{bmatrix} r_1 r_2 & r_1 f_2 & f_1 r_2 & f_1 f_2 \\ r_1(1-r_2) & r_1(1-f_2) & f_1(1-r_2) & f_1(1-f_2) \\ (1-r_1)r_2 & (1-r_1)f_2 & (1-f_1)r_2 & (1-f_1)f_2 \\ (1-r_1)(1-r_2) & (1-r_1)(1-f_2) & (1-f_1)(1-r_2) & (1-f_1)(1-f_2) \end{bmatrix} \begin{bmatrix} N_{RR} \\ N_{RF} \\ N_{FR} \\ N_{FF} \end{bmatrix} \tag{5.2}$$

Definitions for "Tight" and "Loose" muons are chosen to use this equation for

this analysis. "Tight" muons represent muons that pass all of the analysis requirements, and "Loose" muons represent muons that have failed the isolation requirement, but would otherwise also be "Tight" muons. These definitions allow 4 possibilities of the eventual dimuon final state for each event, leading to the number of events with a leading and/or sub-leading muon(s) being "Tight"("T") or "Loose"("L") (N_{TT}, N_{TL}, N_{LT}, N_{LL}). N_{RR}, N_{RF}, N_{FR} and N_{FF} represent the number of events with a leading and/or sub-leading muon(s) in the final state being a real("R") or fake("F") muon, while the definitions for $r_{1(2)}$ and $f_{1(2)}$ are as follows:

- $r_{1(2)}$ efficiency for a **isolated** (sub)leading lepton to pass the isolation selection cuts
- $f_{1(2)}$ efficiency for a **non isolated** (sub)leading lepton to pass the isolation selection cuts (fake-rate)

A control region where the multijet background dominates is defined to determine the fake efficiency f. This control region is defined by the conditions:

- Exactly 1 muon and at least 1 jet
- Selected muon has $p_T > 40$ GeV
- Transverse mass $M_T < 60$ GeV
- Missing transverse energy $E_T^{miss} < 50$ GeV

The fake efficiency f is determined within the difference between the data and all other MC simulated backgrounds in this control region, which is used as a data-driven estimate of the contribution from multijet backgrounds. The value is given by $N_{muons}^{Iso}/N_{muons}^{NoIso}$, where N_{muons}^{Iso} is the number of selected muons satisfying the isolation requirement, i.e. the number of "Tight" muons. Similarly N_{muons}^{NoIso}

is the number of selected muons without the isolation requirement, i.e. the number of "Tight" muons plus the number of "Loose" muons. The fake efficiency is determined to be $f = 0.2664 \pm 0.0007$.

The real efficiency is determined similarly in the $Z + jets$ control region as described in Section 5.5.1. It is performed in the difference between data and all MC samples except the samples representing the $Z/\gamma^* \rightarrow \mu\mu$ process, which is used to represent a data-driven estimate of the $Z + jets$ backgrounds. The value is again given by $N^{Iso}_{muons}/N^{NoIso}_{muons}$, which is determined to be $r = 0.974 \pm 0.003$. The identical procedure is performed only on the MC samples representing the $Z/\gamma^* \rightarrow \mu\mu$ process as a sanity check, and the efficiency is determined to be $r_{MC} = 0.9931 \pm 0.0001$. Although the acquired values for the real efficiency from the two different approaches do not agree within statistical error, this latter acquired value also shows the real effeciency is very close to one, which is an adequate validation for the former result. The real and fake efficiencies are presented in Figure 5.6 as a function of μ_{p_T}. The relative small variations across the p_T range for both real and fake efficiencies support the representativeness of the determined general values.

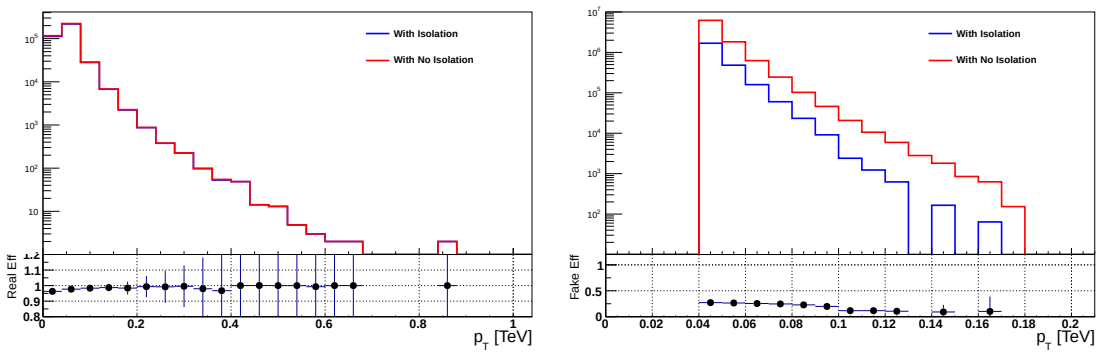

(A) (B)

FIGURE 5.6: Figure 5.6a and 5.6b respectively show the real and fake efficiencies as a function of muon p_T.

The determined values of the real and fake efficiencies are then used in Equation 5.2 along with the values N_{TT}, N_{TL}, N_{LT} and N_{LL} observed in the optimized signal

region for $M_{LQ} = 600$ GeV (described in Section 5.7.1):

$$N_{TT} = 17, \qquad N_{TL} = 1, \qquad N_{LT} = 0, \qquad N_{LL} = 0$$

These determined quantities can be used with Equation 5.2 to solve for the quantities N_{RR}, N_{RF}, N_{FR} and N_{FF}, where they represent the number of events with a leading and/or sub-leading muon(s) in the final state being a real("R") or fake("F") muon. For the observed number of events in the signal regions where both chosen muons pass the "Tight" requirement (N_{TT}), the above values can provide a data-driven estimate of the ratios between the four possibilities of one or both being real/fake:

$$N_{RR} = 16.967, \qquad N_{RF} = 0.201, \qquad N_{FR} = -0.166, \qquad N_{FF} = -0.002$$

The determined values of N_{RF}, N_{FR} and N_{FF} in this result represent the number of events out of the observed N_{TT} events with two selected "Tight" muons, where one (N_{RF}, N_{FR}) and both (N_{FF}) selected muons are in fact fake muon objects. The scenario where one of the two selected muons in the signal region are in fact a mis-identified muon represent the contamination from $W + jets$ background, while the number of events with both muons being fake represent contamination from multijet background. This estimated result via the data-driven approach suggests that the fake contamination from $W + jets$ and multijet backgrounds in all of the determined signal regions are negligible, the small contributions of MC samples representing these processes that have survived the event selection cuts remain as part of the total background for the analysis.

5.6.3 Selected Sample Yields

The yields from background and signal processes are initially determined by implementing the methods described previously in Section 5.6.1 and 5.6.2. Yields from $Z + jets$ and $t\bar{t}$ backgrounds are further refined with data using the control regions described in Section 5.5. The predicted yields for the total backgrounds (N_i^{MC}) are hence given by:

$$N_i^{MC} = s_{ZCR} \times N_i^{Z+jets} + s_{TCR} \times N_i^{t\bar{t}} + N_i^{others} \tag{5.3}$$

where N_i^{Z+jets}, $N_i^{t\bar{t}}$ and N_i^{others} are yields respectively given by the $Z + jets$, $t\bar{t}$ and all other MC simulated samples. s_{ZCR} and s_{TCR} normalizing scale factors used to refine the $Z + jets$ and $t\bar{t}$ background yields. They are determined in their respective control region by:

$$s_{ZCR} = \left(\frac{N_i^{data} - (N_i^{AllMC} - N_i^{Z+jets})}{N_i^{Z+jets}} \right), \quad s_{TCR} = \left(\frac{N_i^{data} - (N_i^{AllMC} - N_i^{t\bar{t}})}{N_i^{t\bar{t}}} \right) \tag{5.4}$$

where N_i^{data} is the yield from data samples, N_i^{AllMC} is the sum of yields from all background MC samples, and N_i^{Z+jets} and $N_i^{t\bar{t}}$ are yields from the $Z + jets$ and $t\bar{t}$ samples respectively. The resulting scale factors are listed in Table 5.4.

Backgrounds	Scale Factors
$Z + jets$	0.943 ± 0.002
$t\bar{t}$	1.102 ± 0.025

TABLE 5.4: Normalisation scale factors determined in the control regions for the $Z + jets$ and $t\bar{t}$ backgrounds

Sample	Start	Vertex Requirement	Trigger	Trigger Matching	3-Station μ Requirement	$2\times\mu$ && $\geq 2\times$Jets
W$\rightarrow\mu\nu$	2.5e+08 ± 1.1e+05	2.4e+08 ± 1.1e+05	9.8e+07 ± 6.7e+04	5.9e+07 ± 5.1e+04	3.2e+02 ± 49	74 ± 19
$t\bar{t}$	5.3e+06 ± 1.2e+03	5.3e+06 ± 1.2e+03	7e+05 ± 3.5e+02	4.6e+05 ± 2.8e+02	1.7e+04 ± 50	1.3e+04 ± 43
Z$\rightarrow\mu\mu$	2.4e+07 ± 4.3e+03	2.3e+07 ± 4.3e+03	1.5e+07 ± 3.5e+03	1.1e+07 ± 3e+03	4.6e+06 ± 1.9e+03	3.8e+05 ± 5.5e+02
Diboson	6e+05 ± 3.1e+02	5.9e+05 ± 3.1e+02	1.7e+05 ± 1.7e+02	1.2e+05 ± 1.4e+02	9e+03 ± 36	2.3e+03 ± 18
SingleTop	1.1e+06 ± 6.9e+02	1.1e+06 ± 6.9e+02	1.7e+05 ± 2.8e+02	1.1e+05 ± 2.3e+02	1.7e+03 ± 20	6.8e+02 ± 13
Z$\rightarrow\tau\tau$	2.4e+07 ± 6.1e+03	2.4e+07 ± 6.1e+03	8.1e+05 ± 1.1e+03	3.5e+05 ± 7.4e+02	2.6e+03 ± 64	4.9e+02 ± 28
TOTAL MC	3e+08 ± 1.1e+05	3e+08 ± 1.1e+05	1.2e+08 ± 6.7e+04	7.2e+07 ± 5.1e+04	4.7e+06 ± 1.9e+03	3.9e+05 ± 5.5e+02
$LQ(600)$	4.8e+02 ± 6.8	4.8e+02 ± 6.8	4.4e+02 ± 6.5	4e+02 ± 6.2	2.6e+02 ± 5	2.5e+02 ± 5
$LQ(650)$	2.7e+02 ± 3.8	2.7e+02 ± 3.8	2.4e+02 ± 3.6	2.2e+02 ± 3.5	1.4e+02 ± 2.8	1.4e+02 ± 2.7
$LQ(700)$	1.6e+02 ± 2.2	1.5e+02 ± 2.2	1.4e+02 ± 2.1	1.3e+02 ± 2	82 ± 1.6	80 ± 1.6
$LQ(750)$	90 ± 1.3	90 ± 1.3	81 ± 1.2	72 ± 1.1	47 ± 0.93	46 ± 0.92
$LQ(800)$	53 ± 0.76	53 ± 0.76	49 ± 0.73	44 ± 0.69	28 ± 0.55	28 ± 0.55
$LQ(850)$	32 ± 0.46	32 ± 0.46	29 ± 0.44	26 ± 0.42	17 ± 0.34	17 ± 0.34
$LQ(900)$	20 ± 0.28	19 ± 0.28	18 ± 0.27	16 ± 0.26	10 ± 0.21	10 ± 0.21
$LQ(950)$	12 ± 0.18	12 ± 0.18	11 ± 0.17	9 ± 0.16	6 ± 0.13	6 ± 0.13
$LQ(1000)$	7 ± 0.11	7 ± 0.11	7 ± 0.1	6 ± 0.099	4 ± 0.079	3 ± 0.079
$LQ(1050)$	4 ± 0.069	4 ± 0.069	4 ± 0.066	3 ± 0.062	2 ± 0.05	2 ± 0.05
$LQ(1100)$	3 ± 0.044	3 ± 0.044	2 ± 0.042	2 ± 0.039	1 ± 0.032	1 ± 0.032
$LQ(1150)$	2 ± 0.028	1 ± 0.028	1 ± 0.027	1 ± 0.025	1 ± 0.021	1 ± 0.02
$LQ(1200)$	1 ± 0.018	1 ± 0.018	1 ± 0.017	1 ± 0.016	0 ± 0.013	0 ± 0.013
$LQ(1250)$	0 ± 0.012	0 ± 0.012	0 ± 0.011	0 ± 0.01	0 ± 0.0083	0 ± 0.0083
$LQ(1300)$	0 ± 0.0077	0 ± 0.0077	0 ± 0.0073	0 ± 0.0069	0 ± 0.0054	0 ± 0.0054

TABLE 5.5: Predicted yields for different background processes at each event selection requirement cut, with all relevant scale factors applied.

Table 5.5 shows the predicted yields from different backgrounds and leptoquark mass values after all of the mentioned scale factors are applied respectively to the MC samples.

5.7 Leptoquark Signal Processes

The combination of the event and object selection criteria is designed to filter out background interactions while maintaining the acceptance of signal processes as high as possible. Further techniques are additionally applied to isolate the LQ processes in the surviving candidate events.

5.7.1 Signal Acceptance

Monte Carlo samples representing the LQ interactions are used to determine the acceptance of the event and object selection criteria. For LQ mass at 700 GeV, it is determined to be ≈52%. This efficiency is used to estimate the number of expected events for LQ at different mass points as shown in Table 5.6.

5.7.2 Definition of Signal Regions

A signal region at each generated LQ mass point is determined by optimizing the statistical significance using Equation 5.5 [135, 136]:

$$Z = \sqrt{2[(s+b)\ln(1+s/b) - s]} \tag{5.5}$$

where s and b are respectively the yields at the preselection stage from the signal sample and all combined backgrounds. This procedure is performed in a three

LQ Mass (GeV)	Before Selection requirements	52% Efficiency	After Selection requirements
600	482 ± 7	251	255 ± 5
650	270 ± 4	140	138 ± 3
700	155 ± 2	81	81 ± 2
750	90 ± 1	47	46.7 ± 0.9
800	54 ± 0.8	28.0	28.1 ± 0.6
850	33 ± 0.5	17.0	17.2 ± 0.3
900	20 ± 0.3	10.4	10.5 ± 0.2
950	12 ± 0.2	6.5	6.4 ± 0.1
1000	7.8 ± 0.1	4.0	3.98 ± 0.08
1050	4.91 ± 0.07	2.55	2.51 ± 0.05
1100	3.12 ± 0.04	1.62	1.59 ± 0.03
1150	2.00 ± 0.03	1.04	1.04 ± 0.02
1200	1.29 ± 0.02	0.67	0.67 ± 0.01
1250	0.83 ± 0.01	0.43	0.414 ± 0.008
1300	0.539 ± 0.008	0.281	0.267 ± 0.005

TABLE 5.6: Number of expected events determined from MC simulated samples with the analysis requirements for each LQ mass point. The effciency of ≈52% for $M_{LQ} = 700$ GeV is shown here to be a good estimate for the selection efficiencies at other mass points.

dimensional phase space constructed by $M_{\mu\mu}$, L_T and H_T, independently for each simulated LQ mass point signal sample. Table 5.7 shows some of the results of this optimization.

Distributions of the average LQ mass $< m_{LQ} >$ from the nominal selection, as well as the alternative distributions from different systematic uncertainties (described in Section 5.9) that are within these signal region definitions are used as input to the Profile likelihood treatment for the final analysis result.

LQ Mass (GeV)	$M_{\mu\mu} >$ (GeV)	$L_T >$ (GeV)	$H_T >$ (GeV)	Significance
600	220	420	380	21.07
650	220	420	395	16.52
700	220	420	395	12.08
750	220	420	455	8.82
800	220	530	390	6.51
850	220	535	470	5.02
900	220	490	580	3.85
950	220	485	650	3.04
1000	220	535	650	2.22
1050	220	495	670	1.65
1100	220	540	665	1.16
1150	220	530	670	0.87
1200	220	550	670	0.62
1250	220	555	670	0.41
1300	220	570	670	0.29

TABLE 5.7: Peak significance values in the three dimensional phase space constructed by $M_{\mu\mu}$, L_T and H_T, as well as their respective values for this peak at selected LQ mass points.

5.8 Consistency Validations

Validations on different components of the analysis were carried out to inspect if related assumptions were within expectations. The results of these validations are used to justify if additional considerations were required, for their respective part of the analysis.

5.8.1 Charm VS Strange Comparison

Leptoquark signal samples of different mass points used in this analysis with a dimuon final state were generated to decay into two muons and two charm quarks. Signal samples decaying alternately into strange quarks instead of charm quarks were produced at $M_{LQ} = 1100\ GeV$. Comparison between the strange and charm

quark signal samples are made at this mass point, to inspect if there are any significant differences that require extra considerations. Distributions of different key kinematic variables are compared between the two samples, as shown in Figure 5.7. No differences beyond the scale of statistical fluctuations are observed. Distributions of additional variables showing their agreement are shown in Appendix B.

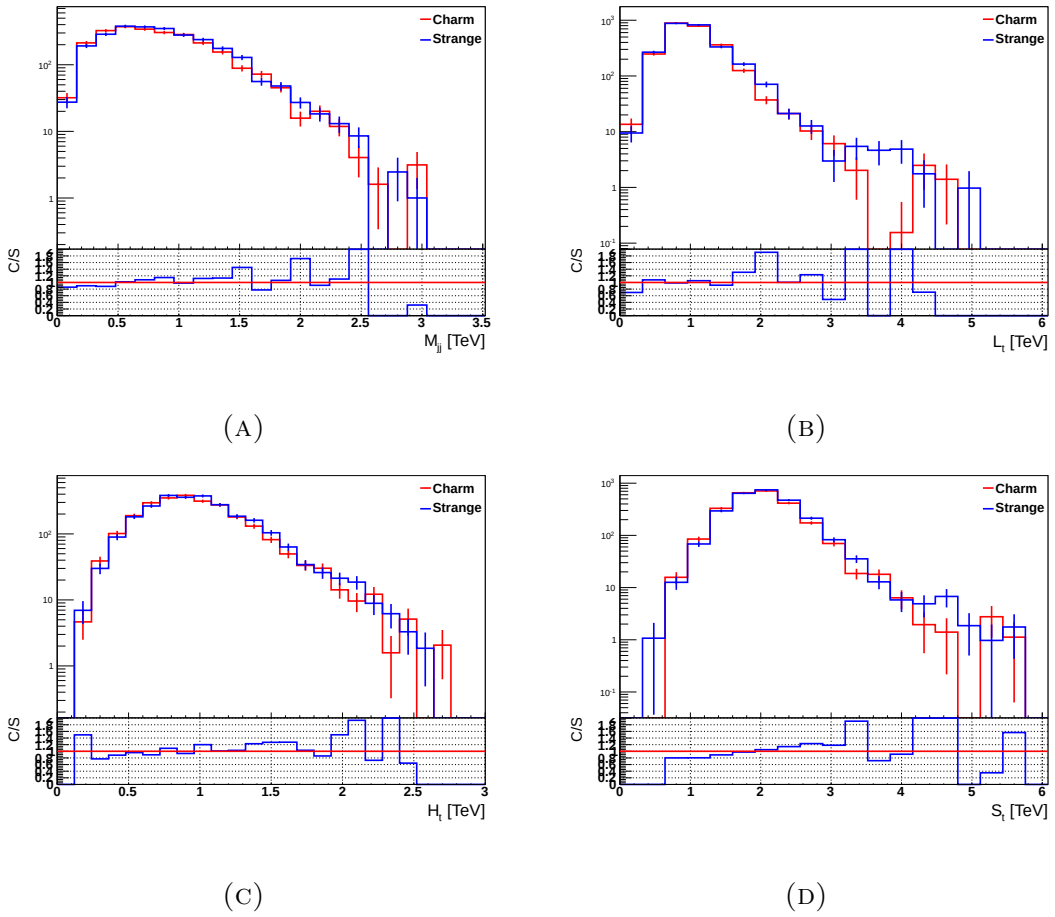

(A) (B)

(C) (D)

FIGURE 5.7: Comparisons of different key kinematic variables between LQ signal samples at $M_{LQ} = 1100$ GeV, decay respectively into $\mu\bar{\mu}c\bar{c}$ and $\mu\bar{\mu}s\bar{s}$ final states.

Table 5.8 shows a comparison of raw yields at different stages of event selection between the two samples, and the efficiency of all the event selection requirements differ by only 2% between the two samples. The leptoquark signal samples at different mass points generated to decay into two muons and two charm quarks

are hence sufficient for this analysis, without the need of extra considerations regarding the alternate final state with strange quarks.

Sample	Start	Vertex Requirement	Trigger	Trigger Matching	3-Station μ Requirement	$2\times\mu$ && $\geq 2\times$Jets
Charm	5000	4990	4478	3979	2570	2543
Strange	5000	4990	4511	4006	2656	2623

TABLE 5.8: Comparison of unscaled raw yields between MC signal samples generated at $M_{LQ} = 1100$ GeV decaying into two muons and two charm quarks, and alternatively into two strange quarks instead of charm quarks.

5.8.2 Full VS Fast Simulation

The Drell-Yan MC samples used for the $Z + jets$ background in this analysis were generated using the `ATLFAST-II` [137, 138] simulation package, rather than the usual "Full" simulation. "Full" simulation was used to generate extra samples at 2 different mass ranges (Run number 180772, 800-1000 GeV and Run number 180780, 2750-3000 GeV) for a consistency check. Besides the fact that the `ATLFAST-II` samples were generated with 10 times more statistics (100000 events) compared to the "Full" simulation samples (10000 events), the rejection efficiency at each event selection cut remain very similar. Comparisons of their unscaled raw yields in the selection cut-flow are shown in Table 5.9.

Distributions of different key kinematic variables between the two types of simulation for both mass ranges are compared in Figure 5.8, and no difference beyond the scale of statistical fluctuations are observed. Distributions of additional variables showing their agreement are shown in Appendix C. The samples generated with the ATLFAST methods are hence suitable to use in our analysis in place of their equivalent "Full" simulation versions.

Sample	180772 (Full)	Cut Efficiency	180772 (Fast)	Cut Efficiency
Start	100000	1.00	100000	1.00
Vertex Requirement	99229	0.99	99280	0.99
Trigger	88963	0.89	88960	0.89
Trigger Matching	78254	0.78	78750	0.79
3-Station μ Requirement	48180	0.48	48640	0.49
$2\times\mu$ && $\geq 2\times$Jets	8707	0.09	8950	0.09

(A)

Sample	180780 (Full)	Cut Efficiency	180780 (Fast)	Cut Efficiency
Start	97000	1.00	100000	1.00
Vertex Requirement	96383	0.99	99400	0.99
Trigger	85439	0.88	88500	0.89
Trigger Matching	73394	0.76	75800	0.76
3-Station μ Requirement	44898	0.46	46940	0.47
$2\times\mu$ && $\geq 2\times$Jets	7925	0.08	8400	0.08

(B)

TABLE 5.9: Comparison of predicted yields between MC simulated samples generated with "Full" simulation and alternatively with the `ATLFAST-II` algorithm. MC samples representing the $\gamma* \rightarrow \mu\mu$ processes at two ranges of dimuon invariant mass, 800-1000 GeV (Run number 180772) in 5.9a and 2750-3000 GeV (Run number 180780) in 5.9b, are used for comparison.

5.9 Systematic Uncertainties

Systematic uncertainties are inherent biases that shifts measurements in a consistent manner, their considerations are important to obtaining the final result. In cases such as exclusion limits, their contributions can influence the final result. Each uncertainty can be categorized as either a *Systematic Uncertainty* or a *Sta-*

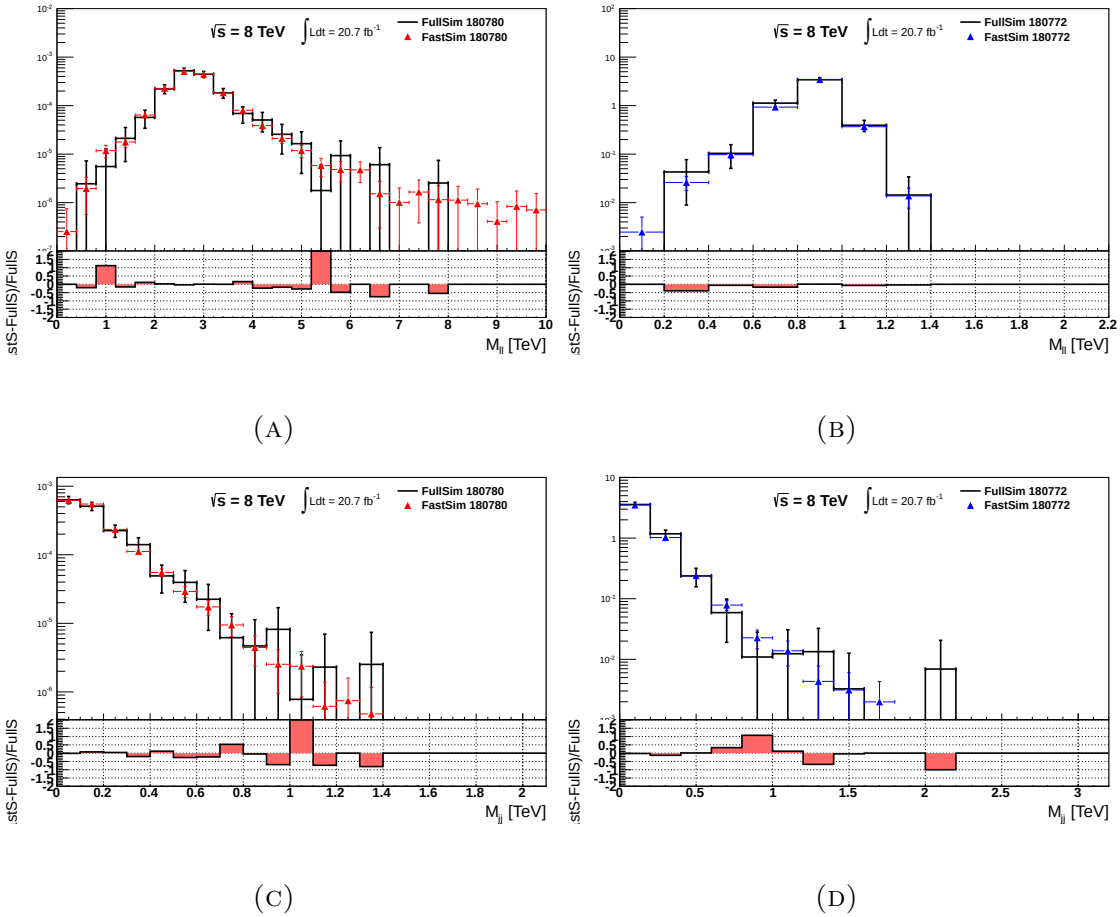

FIGURE 5.8: Comparisons of different key kinematic variables between Full and Fast simulations for the two selected mass ranges of the Drell-Yan MC samples.

tistical Uncertainty. While the latter is proportional to $\frac{1}{\sqrt{n}}$ (n denotes the number of events) and can be reduced by increasing the data sample size, the former represents consistent shifts of values due to experimental effects or theoretical biases, and cannot be reduced by taking more data.

Alternate distributions are produced for each type of systematic uncertainty considered. They are produced from the nominal analysis selection with respective systematic variations implemented. All of these alternate distributions will be used as inputs to the HistFitter tool [139, 140] as contributions to the final result.

5.9.1 Luminosity

During the 2012 data taking period with $\sqrt{s} = 8$ TeV, a total integrated luminosity of $\mathscr{L}_{int} = 20.7$ fb^{-1} was recorded by the ATLAS detector. The accuracy in this measurement of absolute luminosity affects the evaluation of background levels as well as the sensitivity of the signal, and is carefully calibrated using a series of dedicated *van der Meer* scans. The uncertainty on the integrated luminosity is $\pm 2.8\%$. It is derived, following the same methodology as that detailed in [141], from a preliminary calibration of the luminosity scale derived from beam-separation scans performed in November 2012.

5.9.2 Jet Energy Scale and Resolution

The uncertainties of Jet Energy Scale (JES) measurements are determined following the recommendations of the JetEtMiss group [142, 143]. Their recommendations account for:

- in-situ analysis (Z+jets balance, γ+jets balance, multi-jet balance)
- Eta calibration (Calibration on the response of jets)
- Pile-up (Dependence on p_T offsets, No. of primary vertices (NPV) and average No. of interactions per bunch crossing (μ))
- High p_T jets (uncertainties from single hadron propagation behaviour)
- Flavour Composition and response (Uncertainty on gluon fraction from jet reconstruction)

In their software package developed especially for this task, these several types of JES related uncertainties are grouped into seven different sets of nuisance parameters. Variation of 1σ for all parameters are also provided in the package, and are

propagated in parallel though the selection criteria of the analysis to produce alternate distributions showing corresponding effects. Comparisons with the nominal p_T distribution are shown in Figure 5.9.

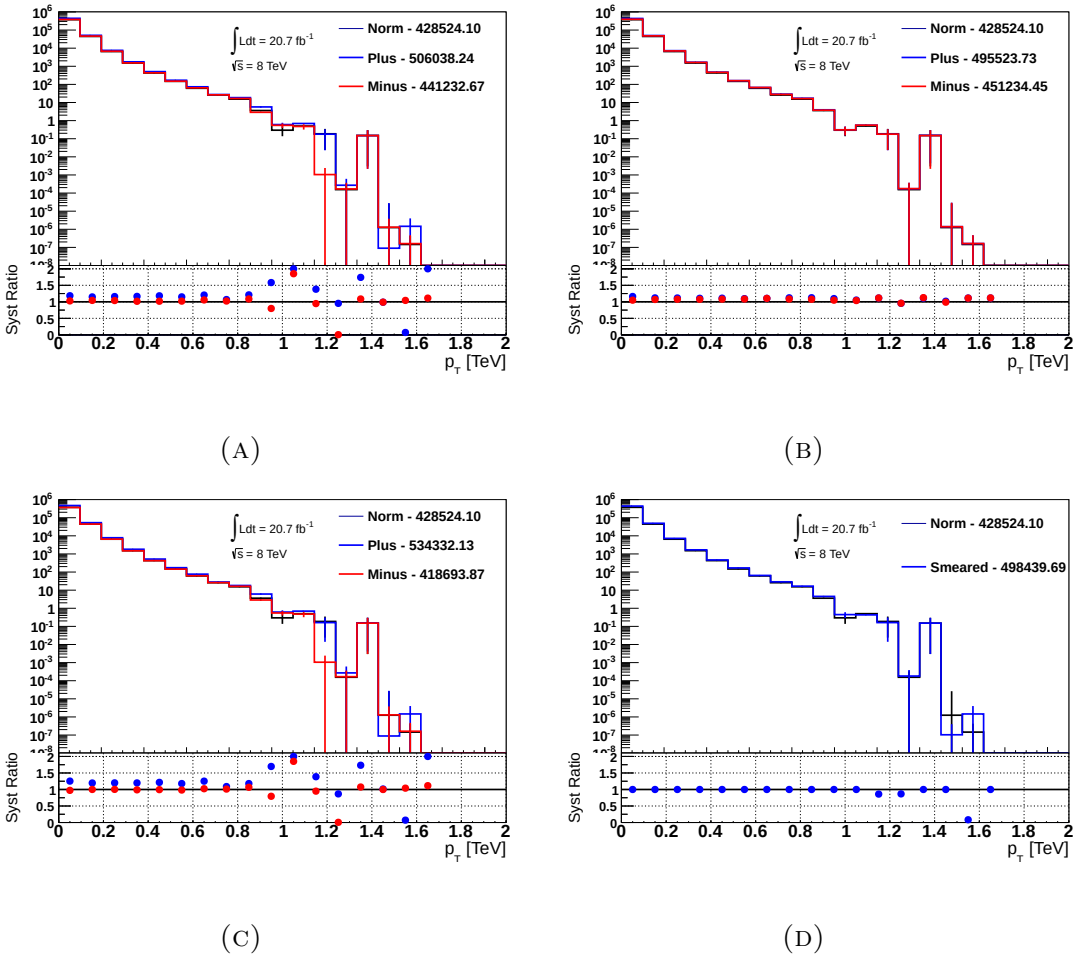

FIGURE 5.9: Figure 5.9a, 5.9b and 5.9c shows the 1σ variation in p_T respectively from Baseline, Pile-up and Flavour Topology related nuisance parameters that are associated with Jet Energy Scale uncertainty. Figure 5.9d shows the effect of smearing to the p_T distribution, representing the uncertainty associated to Jet Energy resolution. These uncertainties are shown in these distributions to only have small effects, and are used to derive the final result presented in Chapter 6.

As the level of agreement in resolutions of jets between data and MC simulations is very high, the smearing of jets in the nominal selections are not required. The smearing tool for jets is hence recommended to use for obtaining the corresponding

systematic uncertainty [143], the associated effect to the p_T distribution is shown in Figure 5.9d.

5.9.3 Muon momentum corrections

Correction scale factors (as discussed in Section 5.2.2) derived by the MCP [129] group that account for issues such as resolution and reconstruction efficiencies also have associated uncertainties. The official software package that was developed by the MCP group for these corrections also provide their systematic uncertainties. Variations on the difference in scale, muon p_T resolution in the Inner Detector and Muon Spectrometer are shifted at 1σ, and propagated in parallel through the selection criteria of the analysis to produce alternate distributions. Comparisons with the nominal p_T distribution are shown in Figure 5.10.

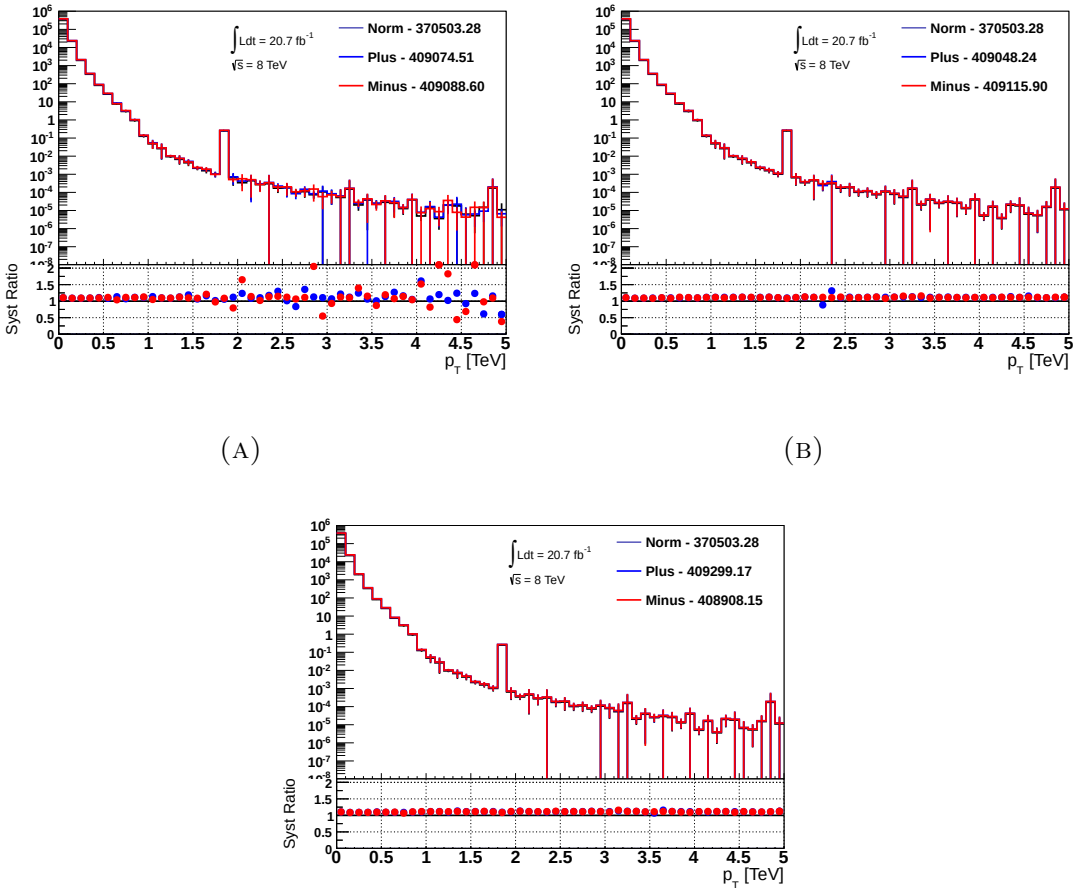

(A) (B)

(C)

FIGURE 5.10: Figure 5.10a, 5.10b and 5.10c show the uncertainties associated with scale, muon p_T resolution in the Inner Detector and Muon Spectrometer in the p_T spectrum, compared to the nominal distribution. The "spike" at 1900 GeV is a statistical effect from the $Z \to \mu\mu$ MC sample generated by `SHERPA`. These uncertainties are shown in these distributions to only have small effects, and are used to derive the final result presented in Chapter 6.

Chapter 6

Results

Procedures presented in Chapter 5 were carried out for the analysis to ensure the validity of our assumptions, such as corroborating in various ways the level of accuracy at describing the physics processes using the MC samples. These procedures are important as they assure the analysis result to be unbiased, as well as its validity. Final results of the analysis are presented in this chapter. No presence of leptoquarks have been observed in data, and a statiscal treatment is performed to obtain exclusion bounds.

6.1 Observed Results

Comparison of the observed number of events from data were compared to MC samples representing the SM background processes in each of the defined signal regions as described in Section 5.7.2. Their comparisons are presented in Table 6.1. Presence of leptoquarks can be interpreted as an excess of events above SM expectations in these signal regions. No such excess were found in data in any of the defined signal regions, as the number of observed events in each of the signal regions are within the predictions from the MC samples representing the SM processes.

Comparison between data and MC samples is also performed in the M_{LQ} distribution as shown in Figure 6.1, where presence of leptoquarks in data can also be observed as excess over expected predictions from the SM. No excess above the SM predictions has been observed from this comparison, which is in agreement

M_{LQ}	Data	MC Backgrounds	MC Signal
600	17	20.75 ± 2.07	147.03 ± 3.77
650	15	18.64 ± 1.94	88.27 ± 2.18
700	15	18.64 ± 1.94	58.52 ± 1.35
750	9	11.53 ± 1.46	33.80 ± 0.78
800	6	6.90 ± 1.01	20.00 ± 0.46
850	5	4.34 ± 0.77	12.25 ± 0.28
900	2	3.11 ± 0.66	7.22 ± 0.17
950	2	2.05 ± 0.53	4.30 ± 0.10
1000	2	1.58 ± 0.45	2.72 ± 0.06
1050	2	1.61 ± 0.45	1.79 ± 0.04
1100	2	1.34 ± 0.40	1.17 ± 0.03
1150	2	1.36 ± 0.40	0.82 ± 0.02
1200	1	1.20 ± 0.38	0.54 ± 0.01
1250	1	1.18 ± 0.38	0.34 ± 0.01
1300	1	0.94 ± 0.32	0.23 ± 0.01

TABLE 6.1: Comparison of observed number of events from data in various signal regions with predictions from MC samples representing the SM background processes.

with the observations in the signal regions.

6.2 Limit Setting

No significant excess over the SM-only hypothesis was found in data, and the hypothesis containing the presence of LQs in addition to the SM processes is tested against the SM-only hypothesis to obtain upper exclusion limits as a function of the LQ mass M_{LQ}. The HistFitter tool [140] is used to determine the **Expected** 95% CL upper exclusion limit with the MC samples produced for the background and signal processes at different M_{LQ} values, and the **Observed** 95% CL upper exclusion limit with collected data, using the Modified-Frequentist approach [139].

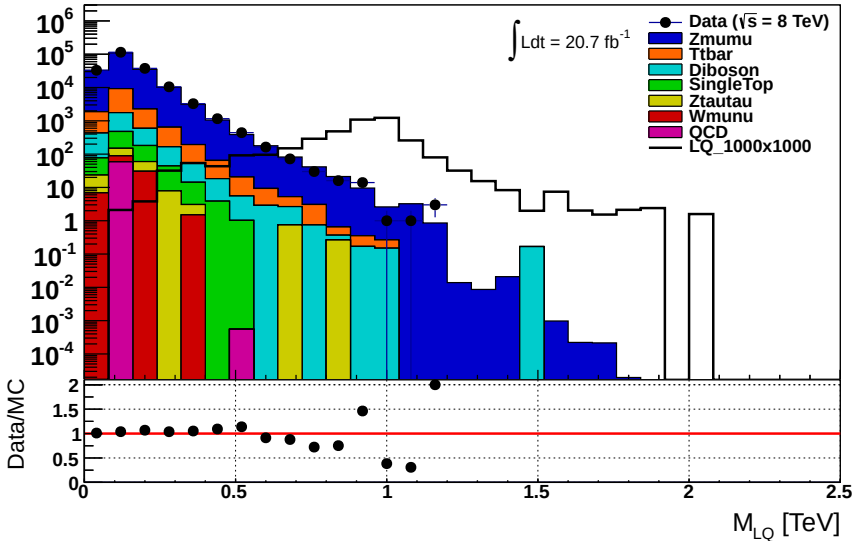

FIGURE 6.1: Comparison between data and MC predictions over the M_{LQ} distribution.

6.2.1 Profile Likelihood

The leptoquark mass M_{LQ} is an observable that is most sensitive to the presence of the signal for this analysis, as shown in figure 6.1. It is used with background MC samples to construct a histogram $\vec{n} = (n_1...n_N)$ of N bins. Expectation values of n_i can be written as $E[n_i] = \mu s_i + b_i$, where μ is the signal strength with $\mu = 0$ corresponding to the background-only hypothesis, and $\mu = 1$ refers to the nominal signal hypothesis. The mean number on entries in the ith bin from signal (s_i) and background (b_i) are defined as:

$$s_i = s_{tot} \int_{bin\ i} f_s(x; \vec{\theta}_s)\ dx \qquad\qquad b_i = b_{tot} \int_{bin\ i} f_b(x; \vec{\theta}_b)\ dx \tag{6.1}$$

The evaluation of the corresponding integrals represent the fraction of the total number signal/background entries (s_{tot}, b_{tot}) in the histogram present in the bin.

The functions $f_s(x;\vec{\theta}_s)$ and $f_b(x;\vec{\theta}_b)$ denotes respectively the probability density functions (**PDF**s) of the signal and background events for variable x, and parameters $\vec{\theta}_s$ and $\vec{\theta}_b$ define the characteristics of the PDF shapes. The variable s_{tot} is fixed by the nominal signal model, while the other nuisance parameters can be denoted by $\vec{\theta} = (\vec{\theta}_s, \vec{\theta}_b, b_{tot})$.

Relevant kinematic variables in the defined control regions ($Z + jets$ and $t\bar{t}$) are chosen to construct histograms $\vec{m} = (m_1...m_M)$ of M bins, with expectation values $E[m_i] = u_i(\vec{\theta})$. The likelihood function considering an outcome containing background and signal processes is defined to be the product of Poisson probabilities from all bins:

$$L(\mu, \vec{\theta}) = \prod_{j=1}^{N} \frac{(\mu s_j + b_j)^{n_j}}{n_j!} e^{-(\mu s_j + b_j)} \prod_{k=1}^{M} \frac{u_k^{m_k}}{m_k!} e^{-(u_k)} \tag{6.2}$$

This definition of likelihood permits the nuisance parameters $\vec{\theta}$ to be "*profiled out*". Since the parameter of interest for this analysis, the signal strength μ, is unknown, the Maximum Likelihood (**ML**) $L_{max,\mu'}$ can be determined for each signal strength value μ'. This is achieved by determining $\hat{\hat{\vec{\theta}}}$, the conditional (fixed μ) ML estimator of $\vec{\theta}$, via the fitting of nuisance parameters from the MC background samples to collected data in the control regions.

The unconditional ML estimators $\hat{\mu}$ and $\hat{\vec{\theta}}$ can then be determined from the resulting likelihood functions $L(\hat{\hat{\vec{\theta}}} \mid \mu)$ across a range of μ values. These can then be used to construct the **Profile Likelihood** ratio:

$$\lambda(\mu) = \frac{L(\mu, \hat{\hat{\vec{\theta}}})}{L(\hat{\mu}, \hat{\vec{\theta}})} \tag{6.3}$$

This definition of likelihood ratio makes it broaden as a function of μ due to the presence of nuisance parameters, relative to the alternative where their values are

fixed. This indicate the loss of information about μ from the presence of systematic uncertainties. Corresponding P-values are then determined with this ratio over the range of μ values, which subsequently gives the signal strength upper limit μ_{up} for a confidence interval 1-p.

6.2.2 Fitting with Systematics

The fitting of nuisance parameters $\vec{\theta}$ to determine the conditional ML function $L(\hat{\hat{\vec{\theta}}} \mid \mu)$ is performed with the HistFitter tool. The HistFitter tool takes the MC and data samples as described in Section 5.1 as input into three categories for fitting:

- **Signal Region (SR)**: Signal-enriched samples with negligible contribution from background processes, which are the optimized signal regions described in Section 5.7.2.
- **Control Region (CR)**: Background-enriched samples with negligible contribution from signal processes, which are the control regions defined in Section 5.5.
- **Validation Region (VR)**: Samples where contributions from background and signal processes are predicted by PDFs, but not used in the fit. There are the key kinematic variables described in Section 5.4, at the nominal selection level described in Section 5.3.

The background parameters of the PDFs are shared across all SR, CR and VR, while mostly constrained from CR, and large statistics can reduce their uncertainties within SR. Fit results to CR are used to determine the expected contributions of background parameters in SR, and its validation can be verified by extrapolating the result to VR.

The alternate histograms produced from variating each considered systematic uncertainty, as described in Section 5.9, are used as external inputs to the fit. By normalising the integral of the alternate histograms to the nominal histogram, the relative effect of the $\pm 1\sigma$ variations are computed, and applied the effect from such systematic uncertainty to the nominal histogram as a global scaling factor. Such effects are propagated through the fit as contributions to the uncertainty of the final result.

This procedure of determining the upper limit for signal strength μ_{up} is carried out at each of the defined signal regions, using the MC background samples to determine the **Expected** limit, and the collected data for the **Observed** limit. The obtained expected and observed upper limits at each M_{LQ} value are compared to the theoretical cross section as a function of M_{LQ}.

6.2.3 Limits

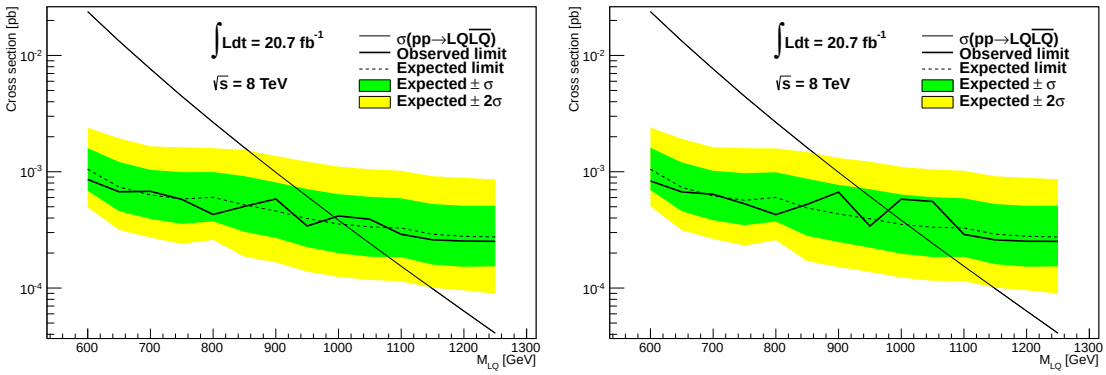

(A) (B)

FIGURE 6.2: Observed and expected cross section exclusion limits at 95% CL as a function of leptoquark mass M_{LQ}, With (Figure 6.2a) and without (Figure 6.2b) the inclusion of systematic uncertainties.

Figure 6.2a and 6.2b show respectively the fit result from HistFitter with and without the input of systematic uncertainties, displaying the observed and expected

95% CL exclusion limit on the cross section as a function of the leptoquark mass M_{LQ}. The inclusion of the systematic uncertainties brings a small effect on the final mass limit ($\approx$ 15 GeV). The observed and expected 95% CL exclusion limits on the M_{LQ} are respectively determined to be 994 GeV and 1011 GeV.

Chapter 7

Conclusions and Outlook

Results of the search for pair-produced second generation scalar leptoquarks in the dimuon plus jets final state, have been presented in this thesis. The analysis was performed on the dataset recorded by the ATLAS detector during the 2012 pp run at $\sqrt{s} = 8$ TeV, totaling to an intergrated luminosity of $\mathscr{L}_{int} = 20.3$ fb^{-1}. No presence of leptoquarks have been observed in the collected data, and an upper limit on the leptoquark mass M_{LQ} was obtained. Background processes from within the SM were estimated with a combination of MC simulations and data-driven methods. Control regions with minimal presence of the leptoquark process were used to validate and improve the prediction of background processes.

Insufficient statistics is a common limitation in searches for new physics, and searches for leptoquarks is no exception. Sensitivity of leptoquark mass can be extended to higher values by collecting more data, however the improvements with the current centre of mass energy will be limited as the leptoquark's production cross section decays exponentially with increasing mass, as previously shown in Figure 1.6.

Figure 7.1 shows the relative increase in parton luminosities for processes initiated by gg, gq and $q\bar{q}$ collisions, from 8 TeV to 13 TeV of collision energy. Including the pair-production of leptoquarks, the sensitivity to higher mass values will be increased greatly when LHC begins data taking again in Run 2, at the beginning of 2015 [144, 145].

The understanding of the various sub-detectors have been improving over the duration of Run 1, which have lead to reduction of related systematic uncertainties as

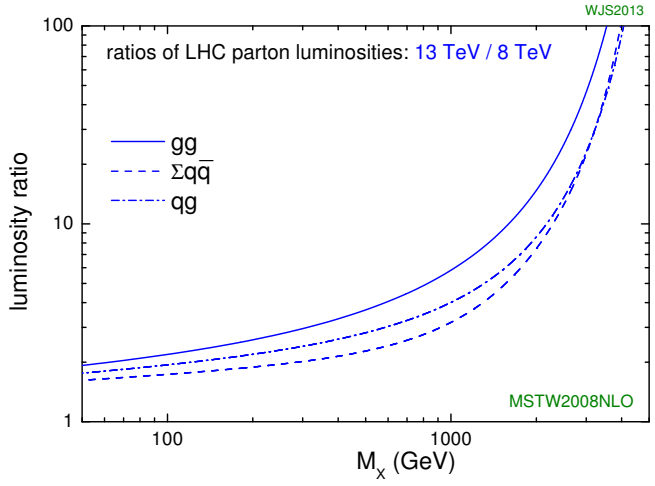

FIGURE 7.1: Ratio of parton luminosities at 13 TeV CM energy relative to 8 TeV, separately for processes initiated by gg, qg and $q\bar{q}$ collisions at the LHC [146].

well as upgrade plans for Run 2. These continuous efforts in gaining understanding of the hardware together with results from precision measurements of Standard Model processes will improve the modelling of Monte-Carlo simulations, predicting the background processes with more accuracy and precision which subsequently extends the experiment's sensitivity to search for signals of new physics that are even smaller in scale.

Despite the successes that the ATLAS detector and other experiements of the LHC have achieved in Run 1, such as the discovery of the Higgs boson [12] and $Z(4430)^-$ tetraquark state [147], there remain many unanswered questions in nature that can be probed with collider experiments at higher energy scales. Precision measurements on the properties of the newly discovered Higgs boson will continue in Run 2, to gain further understanding on its role in the Standard Model. Searches for new physics in both the supersymmetry and exotic sectors, including leptoquarks, will continue to progress in the new energy frontier, either with discoveries or improving current exlusion limits. There will be new challenges such as harsher pileup

and radiation conditions, where thousands of physicists from around the world collaborate to tackle, for a better understanding of Nature at the most fundamental level.

Appendix A

Event Generators

There is a high degree of difficulty in modelling particle collision events at collider experiments with high precision, due to the complexities of the wide range of interactions involved. Various event generators with different emphasis have been developed to produce MC simulations for a wide range of different physics processes.

SHERPA

SHERPA (**S**imulation of **H**igh **E**nergy **R**eactions of **PA**rticles) is a multi-purpose event generator that is capable of simulating photon-photon, photon-lepton, lepton-lepton, lepton-hadron and hadron-hadron collisions. It provides the ability to calculate particle productions at tree level within the Standard Model framework, as well as the Minimal Supersymmetric Standard Model. It has an intrinsic phase-space generator as well as matrix element generators, which can calculate and integrate matrix elements for implemented models at tree level. These functions allow SHERPA to fill the roles of cross section integrator as well as a parton-level event generator. SHERPA essentially stands for the collection of modules within its structure, where each module operate independently with their corresponding functionality such as parton showering and hadronization. More detailed information can be found at [110, 148].

PYTHIA

`PYTHIA` [108, 149] is another multi-purpose event generator that can simulate particle collisions in pp, ep and e^+e^- colliders. It contains a coherent set of models for the evolution from hard processes involving multiple particles, to complex final states that includes multiple hadrons. It also contains models accounting for initial and final state parton showers, beam remnants, string fragmentation and particle decays. It can be used as a standalone generator for particle collisions, while it is also capable to interface with other programs to utilize external parton distribution functions, input parameters for SUSY as well as various decay packages. It is initially written in `Fortran 77` with continous developments for almost 30 years, a complete re-write in C++ to cope with modern day collider experiments lead to the release of `PYTHIA 8.1` in 2007.

HERWIG

`HERWIG` [150] (**H**adron **E**mission **R**eactions **W**ith **I**nterfering **G**luons) is another multi-purpose event generator that is designed with special emphasis on detail simulation of QCD parton showers. It is capable of simulating hard processes of lepton-lepton, lepton-hadron and hadron-hadron collisions, as well as soft processes of hadron-hadron collisions. It uses parton shower as an approach to the simulation of initial and final state QCD radiation including the associated coherent colour effects, as well as azimuthal correlations within and between hadronic jets. It intrinsically contains many processes from SM and many BSM frameworks, including the production and decay of many SUSY particles, with the option of R-parity violation. Similar to `PYTHIA`, `HERWIG` was originally written `Fortran`, and later rewritten in C++ to produce `HERWIG++` [151] as a successor.

ALPGEN

ALPGEN [152, 120] is an event generator dedicated to the simulation of multiparton hard processes in hadron-hadron collisions. It is capable to compute the exact matrix elements for a large set of parton-level processes, at leading order for QCD and EW interactions. However its functionality does not include parton showering and hadronization, its output of either weighted or unweighted event samples are used as inputs to interface with other packages such as PYTHIA and JIMMY.

MC@NLO

MC@NLO [153] is a partonic matrix element generator for production processes such as for heavy quark pairs, single top and inclusive W and Z processes. It makes use of the MC@NLO formulism [114], which consistently combines the Parton Shower Monte Carlo (**PSMC**) and the perturbative QCD approaches to achieve QCD precision at NLO level. The package provides MC subtraction terms required to modify the parton-level short-distance cross sections in standard NLO computations. to avoid double counting when interfacing NLO results with PSMC. HERWIG and JIMMY are common PSMCs that MC@NLO interfaces to the simulation of hadronization and showering.

JIMMY

JIMMY [154] is a package that specializes in simulating multiparton interactions. It computes the multiparton interaction rate using cross section of hard subprocesses, parton densities and area overlapping function $A(b)$, by assuming an associated impact parameter b of the matter distribution. It is commonly used to describe underlying events in collisions, which are often additional activity observed from interactions of beam remnants.

Appendix B

Charm VS Strange Comparison

Comparisons between MC samples of LQ signal process at $M_{LQ} = 1100$ GeV, decaying into two muons and two charm quarks, and alternatively into two muons and two strange quarks. These distributions are produced with the event selection requirements applied, as described in Section 5.3.4.

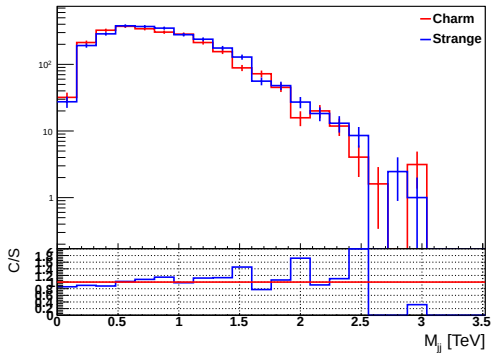

FIGURE B.1: Di-jet invariant mass

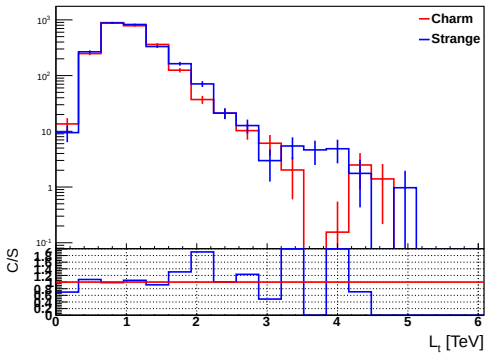

FIGURE B.2: $L_T = p_T^{\mu_1} + p_T^{\mu_2}$

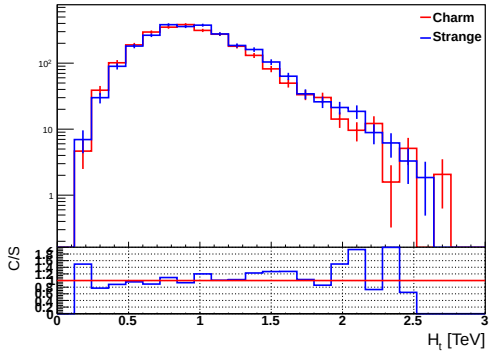

FIGURE B.3: $H_T = p_T^{jet_1} + p_T^{jet_2}$

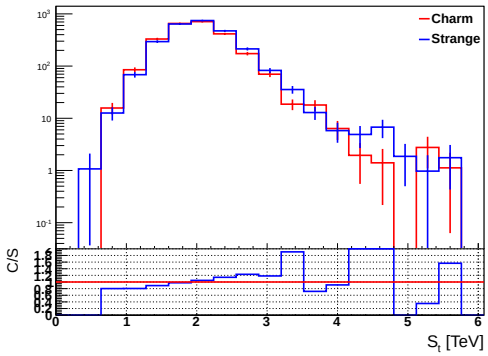

FIGURE B.4: $S_T = L_T + H_T$

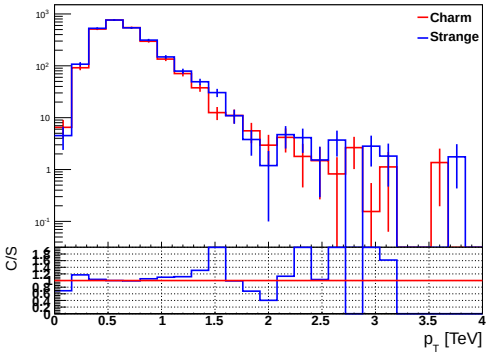

FIGURE B.5: Leading muon p_T

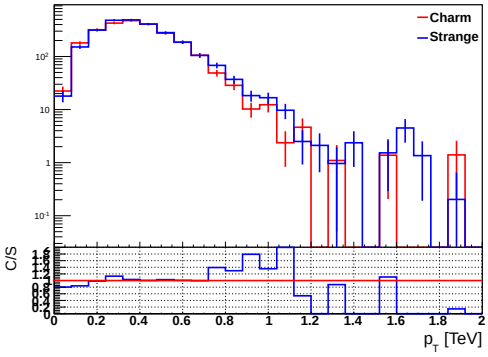

FIGURE B.6: Sub-leading muon p_T

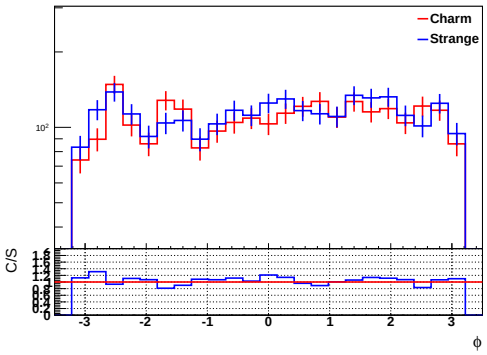

FIGURE B.7: Leading muon ϕ

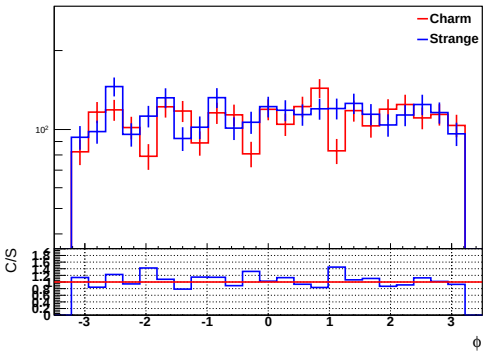

FIGURE B.8: Sub-leading muon ϕ

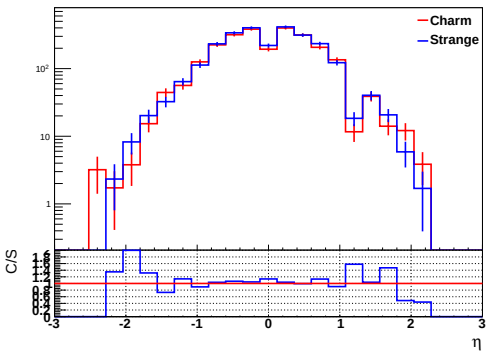

FIGURE B.9: Leading muon η

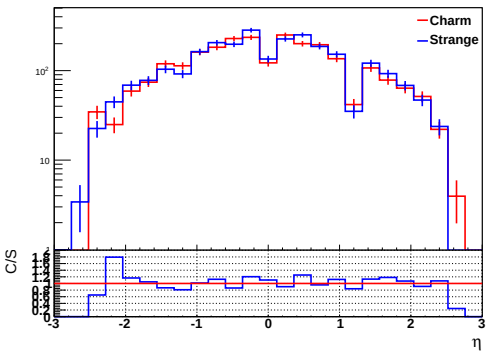

FIGURE B.10: Sub-leading muon η

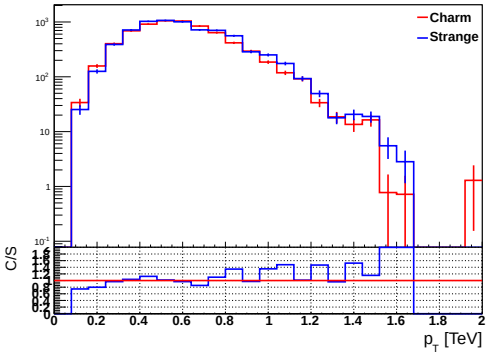

FIGURE B.11: Leading jet p_T

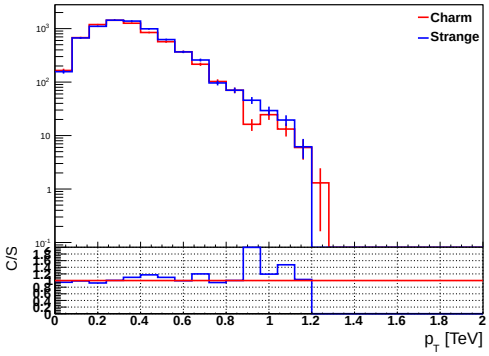

FIGURE B.12: Sub-leading jet p_T

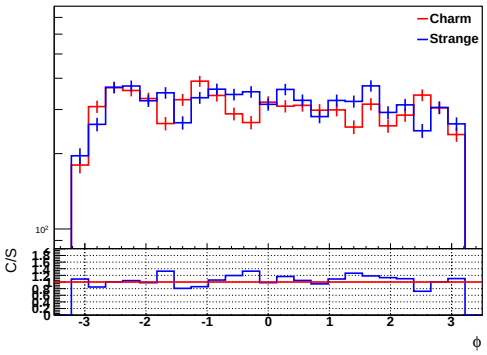

FIGURE B.13: Leading jet ϕ

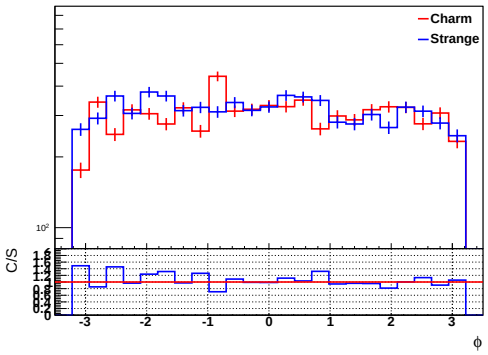

FIGURE B.14: Sub-leading jet ϕ

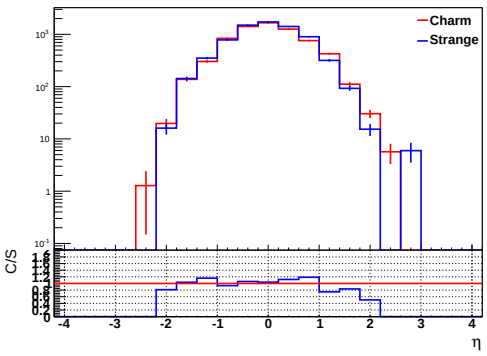

FIGURE B.15: Leading jet η

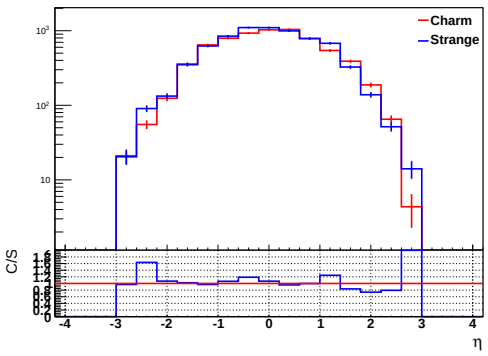

FIGURE B.16: Sub-leading jet η

Appendix C

Full VS Fast Simulation

The Drell-Yan MC samples used for the $Z + jets$ background in this analysis were generated using the `ATLFAST-II` [137, 138] simulation package, rather than the usual "Full" simulation. "Full" simulation was used to generate extra samples at 2 different mass ranges (Run number 180772, 800-1000 GeV and Run number 180780, 2750-3000 GeV) for consistancy check. Besides the fact that the `ATLFAST-II` samples were generated with 10 times more statistics (100000 events) compared to the "Full" simulation samples (10000 events), their differences are within the scale of statistical fluctuations, hence the samples generated with the ATLFAST methods are as suitable to use in our analysis as their equivalent "Full" simulation versions.

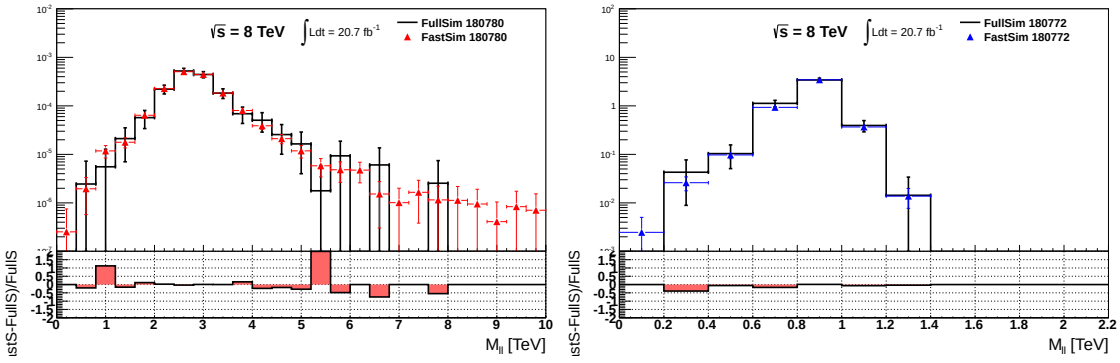

(A) (B)

FIGURE C.1: Invariant mass of the muons

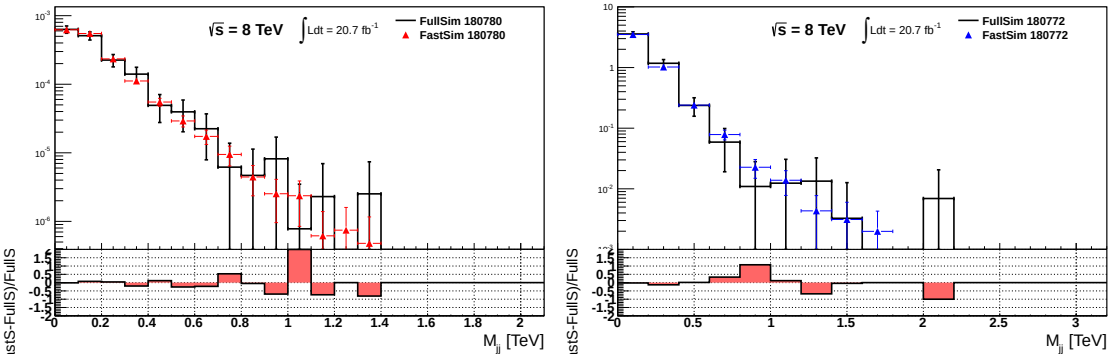

(A) (B)

FIGURE C.2: Invariant mass of the two leading jets

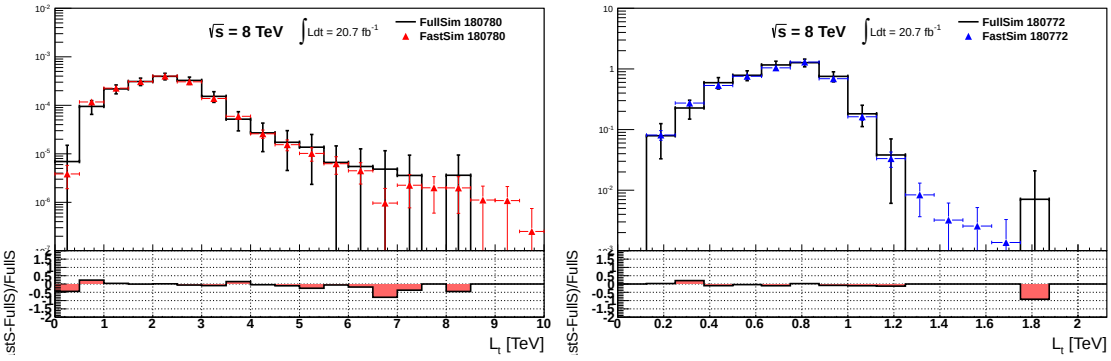

(A) (B)

FIGURE C.3: $L_T = p_T^{\mu_1} + p_T^{\mu_2}$

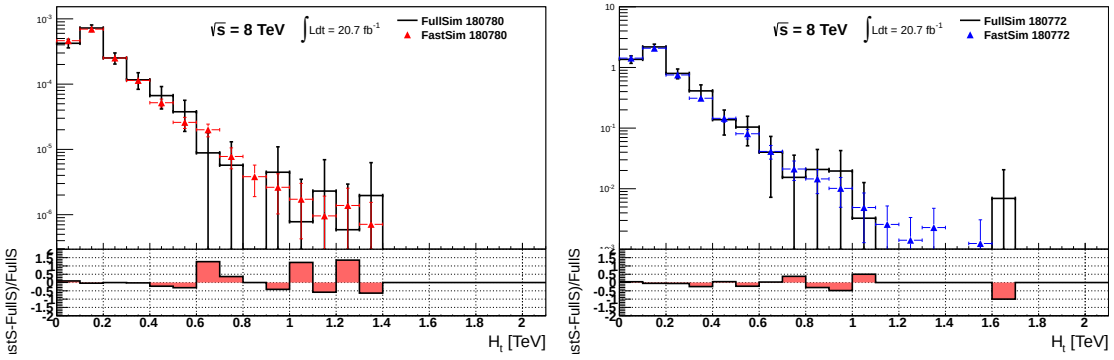

(A) (B)

FIGURE C.4: $H_T = p_T^{jet_1} + p_T^{jet_2}$

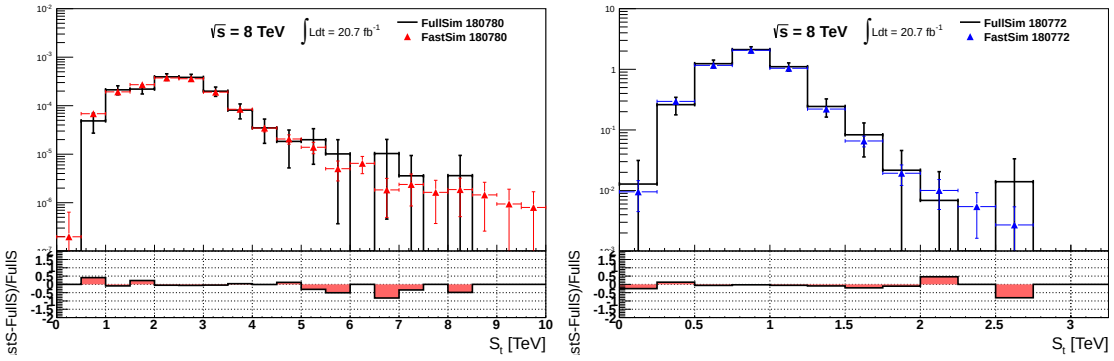

(A) (B)

FIGURE C.5: $S_T = L_T + H_T$

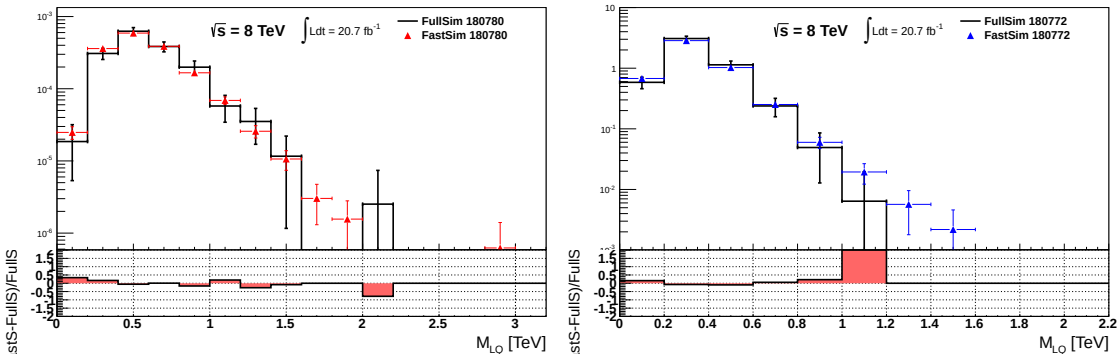

(A) (B)

FIGURE C.6: Average LQ mass $< M_{LQ} >$

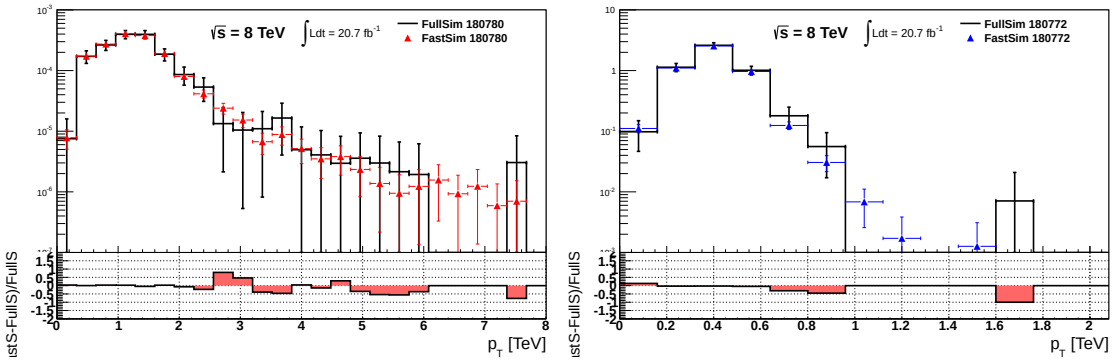

(A) (B)

FIGURE C.7: Leading muon p_T

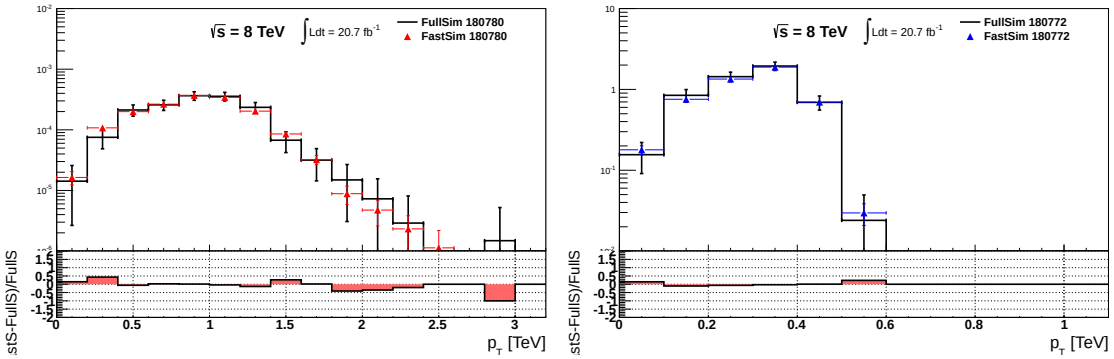

(A) (B)

FIGURE C.8: Sub-leading muon p_T

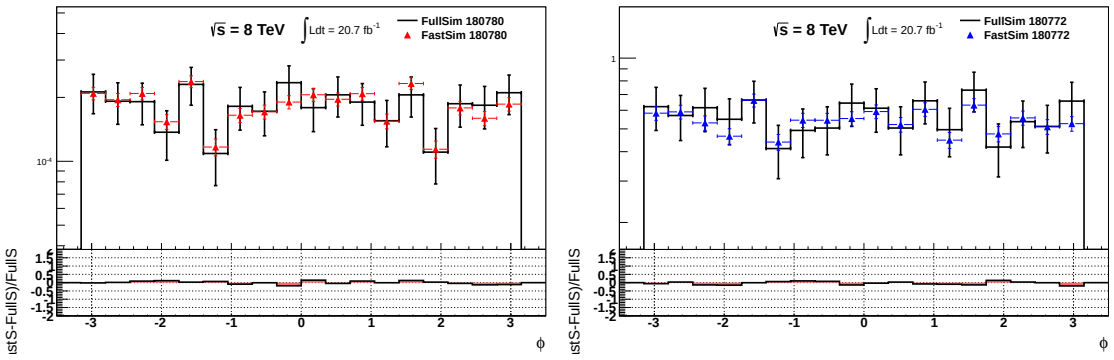

(A) (B)

FIGURE C.9: Muon ϕ

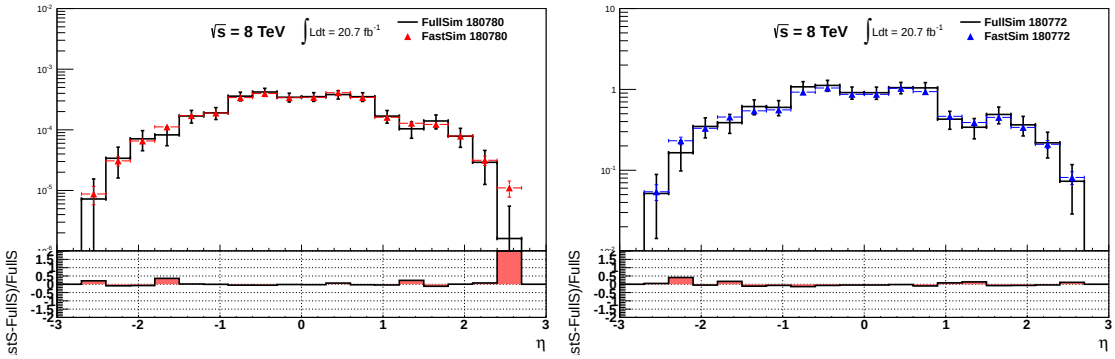

(A) (B)

FIGURE C.10: Muon η

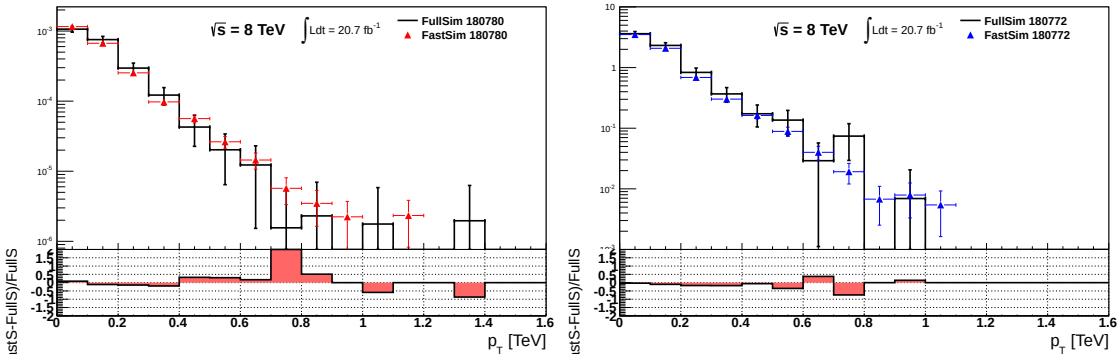

(A) (B)

FIGURE C.11: Leading jet p_T

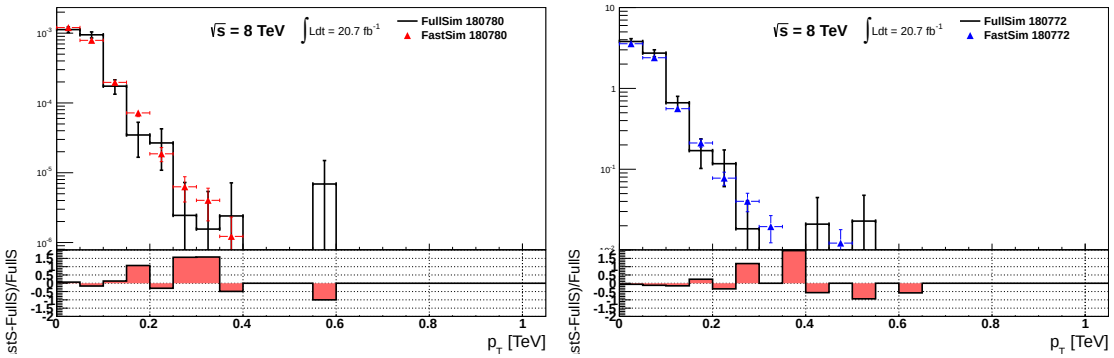

(A) (B)

FIGURE C.12: Sub-leading jet p_T

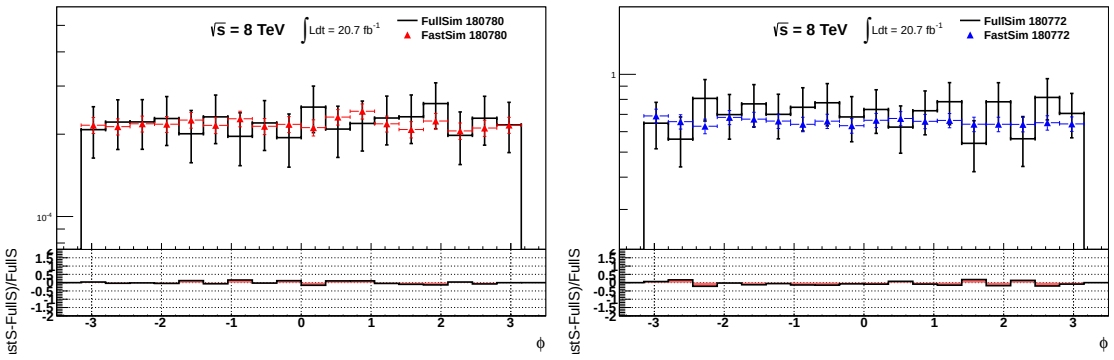

(A) (B)

FIGURE C.13: ϕ distribution of the two leading jets

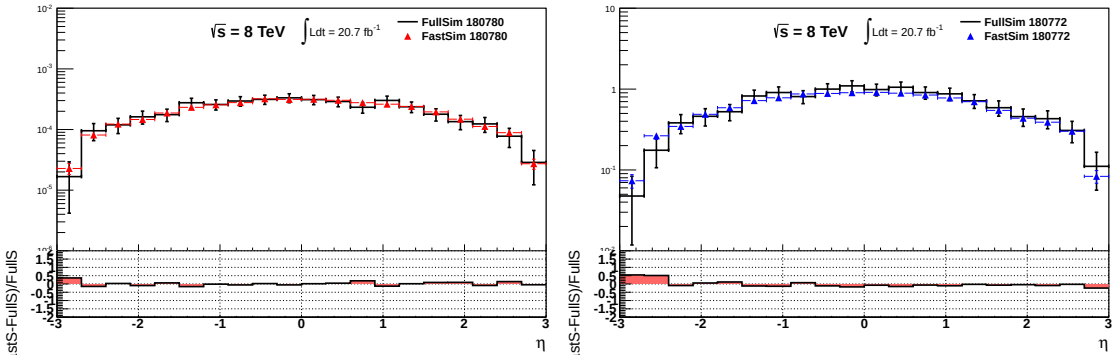

(A) (B)

FIGURE C.14: η distribution of the two leading jets

Bibliography

[1] M.Peskin and D.Schroeder. An Introduction To Quantum Field Theory. Westview Press, 1995.

[2] J.J.Thomson. "Cathode Rays", The Electrician, volume 39. James Gray, 1897.

[3] E.Rutherford. The scattering of alpha and beta particles by matter and the structure of the atom. Phil.Mag., 21:669–688, 1911.

[4] D.Griffiths. Introduction to Elementary Particles. Wiley-VCH, 2004.

[5] A.D.Sakharov. Violation of cp invariance, c asymmetry, and baryon asymmetry of the universe. Pis'ma Zh. Eksp. Teor. Fis., 5:32–35, 1967.

[6] Makoto Kobayashi and Toshihide Maskawa. CP Violation in the Renormalizable Theory of Weak Interaction. Prog.Theor.Phys., 49:652–657, 1973.

[7] K.Nakamura et al. Review of Particle Physics. J. Phys. G: Nucl. Part. Phys., 37(075021), 2010.

[8] E.Noether. Invariant Variation Problems. Gott.Nachr., 1918:235–257, 1918.

[9] A.Salam. Elementary particle theory. Proceedings Of The Nobel Symposium, pages 367–377, 1968.

[10] P.Higgs. Broken symmetries, massless particles and gauge fields. Phys.Lett., (2):132–133, 1964.

[11] The CMS Collaboration. Observation of a new boson at a mass of 125 GeV with the CMS experiment at the LHC. Phys.Lett.B, (716):30, 2012.

[12] The ATLAS Collaboration. Observation of a new particle in the search for the Standard Model Higgs boson with the ATLAS detector at the LHC. Phys.Lett.B, (716):1–29, 2012.

[13] The CMS Collaboration. Study of the mass and spin-parity of the Higgs boson candidate via its decays to Z boson pairs. Phys.Lett.B, 110(081803), 2013.

[14] The ATLAS Collaboration. Evidence for the Spin-0 nature of the Higgs boson using ATLAS data. Phys.Lett.B, (726):120, 2013.

[15] The ATLAS Collaboration. Measurements of Higgs boson production and couplings in diboson final states with the ATLAS detector at the LHC. Phys.Lett.B, (726):88, 2013.

[16] A.Sushkov et al. New experimental limits on non-newtonian forces in the micrometer range. Phys.Rev.Lett., (107), 2011.

[17] P.Peebles and B.Ratra. The cosmological constant and dark energy. Rev.Mod.Phys., (75):559–606, 2003.

[18] G.Bertone. Particle Dark Matter: Observations, Models and Searches. Cambridge University Press, 2010.

[19] M.Peskin. The matter with antimatter. Nature, 419:24–27, 2002.

[20] S.Fukuda et al. Solar b-8 and hep neutrino measurements from 1258 days of super-kamiokande data. Phys.Rev.Lett., 86:5651–5655, 2001.

[21] H.Nilles. Supersymmetry, supergravity and particle physics. Phys.Rept., (110):1–162, 1984.

[22] S.Dimopoulos and H.Georgi. Softly Broken Supersymmetry and SU(5). Nucl.Phys., (B193):150, 1981.

[23] D.Morrissey, T.Plehn, and T.Tait. Physics searches at the LHC. Phys.Rept., (515):1–114, 2012.

[24] G.Ross. Grand Unified Theories. Westview Press, 1984.

[25] Adel Bilal. Lectures on Anomalies. (LPTENS-08-05), 2008.

[26] Barbara Schrempp and Fridger Schrempp. Light Leptoquarks. Phys.Lett., B153:101, 1985.

[27] J.L.Hewett and T.G.Rizzor. Much Ado About Leptoquarks: A Comprehensive Analysis. Phys.Rev., (D56):5709–5724, 1997. arXiv:hep-ph/9703337.

[28] J.Pati and A.Salam. Lepton number as the fourth "color". Phys. Rev., (D 10):275–289, 1974.

[29] F.Zwirner. Lepton number as the fourth "color". Int. J. Mod. Phys., (A 03):49, 1988.

[30] H.Saller. Dynamical interpretation of the technifermion approach motivated by composite gravity. Technical Report MPI-PAE-PTH-7-83. MPI-PAE-PTH-83-7, Max-Planck Inst. Phys., Munich, Jan 1983.

[31] W.Buchmüller, R.Rückl, and D.Wyler. Leptoquarks in Lepton-Quark Collisions. Phys. Lett., B(191):442–448, 1987.

[32] C.Regis and others. Search for Proton Decay via $p \to \mu^+ K^0$ in Super-Kamiokande I, II, and III. Phys.Rev., D86:012006, 2012.

[33] P.Straub. Minireview on Leptoquark Searches. Proceedings of ICHEP, pages 792–795, 2002.

[34] H1 Collaboration. Search for First Generation Leptoquarks in ep Collisions at HERA. Phys.Lett.B, 704(5):388–396, 2011.

[35] H1 Collaboration. Search for Lepton Flavour Violation at HERA. Phys.Lett.B, 701(1):20–30, 2011.

[36] CDF Collaboration D0 Collaboration. Combined Limits on First Generation Leptoquarks from the CDF and D0 Experiments. Technical report, FERMILAB, Oct 1998.

[37] DØ Collaboration. Search for first generation leptoquark pair production in the electron + missing energy + jets final state. Phys.Rev.D, 84(071104), 2011.

[38] DØ Collaboration. Search for pair production of second generation scalar leptoquarks. Phys.Lett.B, 671(2):224–232, 2009.

[39] DØ Collaboration. Search for scalar bottom quarks and third-generation leptoquarks in $p\bar{p}$ collisions at $\sqrt{s} = 1.96TeV$. Phys.Lett.B, 693:95–101, 2010.

[40] ATLAS Collaboration. Search for first generation scalar leptoquarks in pp collisions at $\sqrt{s} = 7$ TeV with the ATLAS detector. Phys.Lett.B, 709:158–176, 2012.

[41] ATLAS Collaboration. Search for second generation scalar leptoquarks in pp collisions at $\sqrt{s} = 7$ TeV with the ATLAS detector. Eur.Phys.J. C72 2151, 2012.

[42] ATLAS Collaboration. Search for third generation scalar leptoquarks in pp collisions at $\sqrt{s} = 7$ TeV with the ATLAS detector. JHEP, (06), 2013.

[43] CMS Collaboration. Search for pair production of first- and second- generation scalar leptoquarks in pp collisions at $\sqrt{s} = 7$ TeV. Phys.Rev.D, 86:052013, 2012.

[44] CMS Collaboration. Search for pair production of third-generation leptoquarks and top squarks in pp collisions at $\sqrt{s} = 7$ TeV. Phys.Rev.Lett., 110:081801, 2013.

[45] CMS Collaboration. Search for third-generation leptoquarks and scalar bottom quarks in pp collisions at $\sqrt{s} = 7$ TeV. JHEP, 55, 2012.

[46] M.Krämer et al. Pair production of scalar leptoquarks at the CERN LHC. Phys.Rev.D, 71:057503, 2005.

[47] Oliver Sim Brüning, Paul Collier, P Lebrun, Stephen Myers, Ranko Ostojic, John Poole, and Paul Proudlock. LHC Design Report. CERN, Geneva, 2004.

[48] Home page of European Organization of Nuclear Research (CERN). http://home.web.cern.ch/, 2014.

[49] S.Myers. Lhc commissioning and first operation. Phil.Trans.R.Soc.A 28, 370(1961):859–875, 2012.

[50] First beam in the LHC - accelerating science. http://press.web.cern.ch/press-releases/2008/09/first-beam-lhc-accelerating-science, 2008.

[51] H.Haseroth, H.Hora, and Heinrich. Ion sources. (CERN-PS-92-23-HI):59 p, Apr 1992.

[52] K.Schindl. The Injector Chain for the LHC; rev. version. (CERN-PS-99-018-DI):7 p, Mar 1999.

[53] F.Zimmermann. LHC: The Machine. 2012. SLAC Summer Institute.

[54] R.Bailey and P.Collier. Standard Filling Schemes for Various LHC Operation Modes. Technical Report LHC-PROJECT-NOTE-323, CERN, Geneva, Sep 2003.

[55] ATLAS Collaboration. The ATLAS Experiment at the CERN Large Hadron Collider. JINST, 3:S08003, 2008.

[56] CMS Collaboration. The CMS experiment at the CERN LHC. JINST, 3:S08004, 2008.

[57] ALICE Collaboration. The ALICE experiment at the CERN LHC. JINST, 3:S08002, 2008.

[58] LHCb Collaboration. The LHCb Detector at the LHC. JINST, 3:S08005, 2008.

[59] S.Myers. The Large Hadron Collider 2008-2013. Int. J. Mod. Phys. A, 28, 2013.

[60] S.Baird. Accelerators for pedestrians; rev. version. Technical Report AB-Note-2007-014. CERN-AB-Note-2007-014. PS-OP-Note-95-17-Rev-2. CERN-PS-OP-Note-95-17-Rev-2, CERN, Geneva, Feb 2007.

[61] S.White. Determination of the Absolute Luminosity at the LHC. PhD thesis, Orsay, Université Paris-Sud 11, Orsay, 2010. Presented on 11 Oct 2010.

[62] ATLAS detector and physics performance: Technical Design Report, 1. Technical Design Report ATLAS. CERN, Geneva, 1999. Electronic version not available.

[63] Atlas public results on luminosity measurements. https://twiki.cern.ch/twiki/bin/view/AtlasPublic/LuminosityPublicResults.

[64] ATLAS Collaboration. Technical Design Report I. Technical report, CERN, Geneva, 1999.

[65] Atlas fact sheet. http://www.atlas.ch/fact-sheets-view.html. Basic Technical information distributed by the ATLAS Secretariat.

[66] ATLAS Collaboration. Technical Design Report I, chapter 1.1.1 Nomenclature. CERN, 1999.

[67] ATLAS Collaboration. Technical Design Report I, chapter 1.3 Magnet system. CERN, 1999.

[68] ATLAS Collaboration. Technical Design Report I, chapter 1.4 Inner Detector. CERN, 1999.

[69] ATLAS Collaboration. Technical Design Report I, chapter 1.5 Calorimeters. CERN, 1999.

[70] ATLAS Collaboration. Technical Design Report I, chapter 1.6 Muon Spectrometer. CERN, 1999.

[71] ATLAS Collaboration. Standalone Vertex Finding in the ATLAS Muon Spectrometer. Technical Report arXiv:1311.7070. CERN-PH-EP-2013-185, CERN, Geneva, Nov 2013.

[72] J C Barriere, F Bauer, M Fontaine, A Formica, V Gautard, P F Giraud, H Graaf, C Guyot, R Hart, S Horvat, O Kortner, S Kotov, H Kroha, F Linde, I Ponsot, I Potrap, and P Schune. The alignment system of the barrel part of the ATLAS muon spectrometer. Technical Report ATL-MUON-PUB-2008-007. ATL-COM-MUON-2008-002, CERN, Geneva, Jan 2008.

[73] S Aefsky, C Amelung, J Bensinger, C Blocker, A Dushkin, M Gardner, K Hashemi, E Henry, B Kaplan, M Ketchum, P Keselman, U Landgraf, A Ostapchuk, J E Rothberg, A Schricker, N Skvorodnev, and H Wellenstein. The Optical Alignment System of the ATLAS Muon Spectrometer Endcaps. J. Instrum., 3(ATL-MUON-PUB-2008-003. ATL-COM-MUON-2008-005):P11005. 49 p, Feb 2008.

[74] Y.Arai et al. ATLAS Muon Drift Tube Electronics. J. Instrum., 3(ATL-MUON-PUB-2008-008. ATL-COM-MUON-2008-010):P09001. 58 p, Apr 2008.

[75] V.Hedberg. http://hedberg.web.cern.ch/hedberg/home/atlas/atlas.html. Private Communication.

[76] J.J. Goodson. Search for Supersymmetry in States with Large Missing Transverse Momentum and Three Leptons including a Z-Boson. PhD thesis, Stony Brook University, May 2012. Presented 17 Apr 2012.

[77] P.Jenni and M.Nessi. ATLAS Forward Detectors for Luminosity Measurement and Monitoring. Technical Report CERN-LHCC-2004-010. LHCC-I-014, CERN, Geneva, Mar 2004.

[78] P.Jenni, M.Nessi, and M.Nordberg. Zero Degree Calorimeters for ATLAS. Technical Report LHCC-I-016. CERN-LHCC-2007-001, CERN, Geneva, Jan 2007.

[79] P.Jenni, M.Nessi, M.Nordberg, and K.Jon-And. ATLAS Forward Detectors for Measurement of Elastic Scattering and Luminosity. Technical Design Report. CERN, Geneva, 2008.

[80] R.Bartoldus et al. Technical Design Report for the Phase-I Upgrade of the ATLAS TDAQ System. Technical Report CERN-LHCC-2013-018. ATLAS-TDR-023, CERN, Geneva, Sep 2013.

[81] G.Duckeck et al. ATLAS computing: Technical design report. 2005.

[82] F.Siegert. Monte-Carlo event generation for the LHC. PhD thesis, Durham University, 2010.

[83] V.Barger and R.Phillips. Collider Physics. Addison- Wesley, 1997.

[84] B.R.Webber. Fragmentation and Hadronization. Int.J.Mod.Phys, (A15S1):577–606, 2000.

[85] V.A.Khoze and W.Ochs. Perturbative QCD Approach to Multiparticle Production. Int.J.Mod.Phys, (A12):2949–3120, 1997.

[86] J.Beringer et al. 2012 Review of Particle Physics. Phys.Rev., D86(1), 2012.

[87] S. Agostinelli et al. GEANT4: A simulation toolkit. Nucl. Instrum. Meth, (A506):250, 2003.

[88] I.Antcheva et al. ROOT — A C++ framework for petabyte data storage, statistical analysis and visualization. Comput. Phys. Commun., 180(12):2499–2512, 2009.

[89] T.Cornelissen, M.Elsing, S.Fleischmann, W.Liebig, E.Moyse, and A.Salzburger. Concepts, Design and Implementation of the ATLAS

New Tracking (NEWT). Technical Report ATL-SOFT-PUB-2007-007. ATL-COM-SOFT-2007-002, CERN, Geneva, Mar 2007.

[90] Performance of the ATLAS Inner Detector Track and Vertex Reconstruction in the High Pile-Up LHC Environment. Technical Report ATLAS-CONF-2012-042, CERN, Geneva, Mar 2012.

[91] R.Frühwirth. Application of Kalman filtering to track and vertex fitting. Nucl. Instrum. Methods Phys. Res., A, 262(HEPHY-PUB-503):444. 19 p, Jun 1987.

[92] G.Aad et al. Expected performance of the ATLAS experiment: detector, trigger and physics. Technical report, Geneva, 2009.

[93] Performance of primary vertex reconstruction in proton-proton collisions at $\sqrt{s}$ =7 TeV in the ATLAS experiment. Technical Report ATLAS-CONF-2010-069, CERN, Geneva, Jul 2010.

[94] R.Fruhwirth, W.Waltenberger, and P.Vanlaer. Adaptive vertex fitting. J.Phys., G34:N343, 2007.

[95] E.Bouhova-Thacker, P.Lichard, V.Kostyukhin, W.Liebig, MLimper, G.Piacquadio, P.Lichard, and C.Weiser. Vertex Reconstruction in the ATLAS Experiment at the LHC. Technical Report ATL-INDET-PROC-2008-003. ATL-COM-INDET-2008-018, CERN, Geneva, Nov 2008. 14.11.2008.

[96] ATLAS Collaboration. Muon Reconstruction Performance. 2010. ATLAS-CONF-2010-064, ATLAS-COM-CONF-2010-065.

[97] Hassani S et al. A muon identification and combined reconstruction procedure for the ATLAS detector at the LHC using the (MUONBOY, STACO,MuTag) reconstruction packages. NIM., A572:77–79, 2006.

[98] Zdenko van Kesteren. Identification of muons in ATLAS. PhD thesis, Amsterdam U., Amsterdam, 2010.

[99] T.Kanno. Commissioning of the ATLAS Muon High Level Trigger with beam collisions at the LHC. Oct 2010.

[100] M.Cacciari, G.Salam, and G.Soyez. The Anti-k(t) jet clustering algorithm. JHEP, 0804:063, 2008.

[101] W.Lampl, S.Laplace, D.Lelas, P.Loch, H.Ma, S.Menke, S.Rajagopalan, D.Rousseau, S.Snyder, and G.Unal. Calorimeter Clustering Algorithms: Description and Performance. Technical Report ATL-LARG-PUB-2008-002. ATL-COM-LARG-2008-003, CERN, Geneva, Apr 2008.

[102] The ATLAS Collaboration. Electron performance measurements with the ATLAS detector using the 2010 LHC proton-proton collision data. Eur.Phys.J, C72:1909, 2012.

[103] Reconstruction and Calibration of Missing Transverse Energy and Performance in Z and W events in ATLAS Proton-Proton Collisions at 7 TeV. Technical Report ATLAS-CONF-2011-080, ATLAS Collaboration, Geneva, Jun 2011.

[104] M.Baak, C.Guyot, et al. Data Quality Status Flags and Good Run Lists for Physics Analysis in ATLAS. Technical Report ATL-COM-GEN-2009-015, CERN, Geneva, Mar 2009.

[105] ATLAS offical GRLs. http://atlasdqm.web.cern.ch/atlasdqm/grlgen/All_Good/.

[106] The ATLAS Collaboration. The ATLAS Simulation Infrastructure. EPJC, (70):823–874, 2010.

[107] W.Ehrenfeld. Challenges of the ATLAS Monte Carlo production during run 1 and beyond. 2013. 20th International Conference on Computing in High Energy and Nuclear Physics.

[108] T.Sjöstrand, S.Mrenna, and P.Skands. A Brief Introduction to PYTHIA 8.1. Comput.Phys.Commun., (178):852–867, 2008.

[109] Summary of ATLAS Pythia 8 tunes. Technical Report ATL-PHYS-PUB-2012-003, CERN, Geneva, Aug 2012.

[110] T.Gleisberg et al. Event generation with SHERPA 1.1. JHEP, (0902:007), 2009.

[111] T.Yamanaka. Validation of Sherpa Diboson with Massive c,b. https://savannah.cern.ch/file/SherpaDibosonValidation_130704.pdf?file_id=34314, 2013.

[112] G.Corcella et al. HERWIG 6.5: an event generator for Hadron Emission Reactions With Interfering Gluons (including supersymmetric processes). JHEP, (0101:010), 2001.

[113] New ATLAS event generator tunes to 2010 data. Technical Report ATL-PHYS-PUB-2011-008, CERN, Geneva, Apr 2011.

[114] S.Frixione and B.R.Webber. Matching NLO QCD computations and parton shower simulations. JHEP, (0206:029), 2002.

[115] S.Frixione, E.Laenen, P.Motylinski, and B.R.Webber. Single-top production in MC@NLO. JHEP, (0603:092), 2006.

[116] S.Frixione, E.Laenen, P.Motylinski, B.Webber, and C.D.White. Single-top hadroproduction in association with a W boson. JHEP, (0807:029), 2008.

[117] J.M.Butterworth, J.R.Forshaw, and M.H.Seymour. Multiparton Interactions in Photoproduction at HERA. Z.Phys, C72:637–646, 1996. arXiv:hep-ph/9601371.

[118] B.P.Kersevan and E.Richter-Was. The Monte Carlo Event Generator AcerMC 2.0 with Interfaces to PYTHIA 6.2 and HERWIG 6.5. Comput.Phys.Commun., 184(3):919–985, 2013. arXiv:hep-ph/0405247.

[119] Further ATLAS tunes of PYTHIA6 and Pythia 8. Technical Report ATL-PHYS-PUB-2011-014, CERN, Geneva, Nov 2011.

[120] M.Mangano et al. ALPGEN, a generator for hard multiparton processes in hadronic collisions. JHEP, 07, 2003. arXiv:hep-ph/0206293.

[121] P.M.Nadolsky et al. Implications of CTEQ global analysis for collider observables. Phys.Rev., D78(013004), 2008. arXiv:hep-ph/0802.0007.

[122] H.L.Lai et al. New parton distributions for collider physics. Phys.Rev., (D82:074024), 2010.

[123] Muon reconstruction efficiency in reprocessed 2010 LHC proton-proton collision data recorded with the ATLAS detector. Technical Report ATLAS-CONF-2011-063, ATLAS Collaboration, Geneva, Apr 2011.

[124] Determination of the muon reconstruction efficiency in ATLAS at the Z resonance in proton-proton collisons at sqrt(s)=7 TeV. Technical Report ATLAS-CONF-2011-008, ATLAS Collaboration, Feb 2011.

[125] ATLAS Collaboration. Jet Calibration at ATLAS, 2011. Poster presected at LHCC 2011 at CERN by R.Camacho.

[126] Close-by Jet Effects on Jet Energy Scale Calibration in pp Collisions at sqrt(s)=7 TeV with the ATLAS Detector. Technical Report ATLAS-CONF-2011-062, ATLAS Collaboration, Geneva, Apr 2011.

[127] Jet energy resolution and selection efficiency relative to track jets from in-situ techniques with the ATLAS Detector Using Proton-Proton Collisions at a Center of Mass Energy $sqrts = 7$ TeV. Technical Report ATLAS-CONF-2010-054, ATLAS Collaboration, Geneva, Jul 2010.

[128] ATLAS Collaboration. Jet energy resolution in proton-proton collisions at $\sqrt{s} = 7$ TeV recorded in 2010 with the ATLAS detector. Eur. Phys. J. C, 73(arXiv:1210.6210. CERN-PH-EP-2012-191):2306. 26 p, Oct 2012.

[129] Preliminary results on the muon reconstruction efficiency, momentum resolution, and momentum scale in ATLAS 2012 pp collision data. Technical Report ATLAS-CONF-2013-088, CERN, Geneva, Aug 2013.

[130] M. Cacciari and G. P. Salam. Dispelling the N^3 myth for the Kt jet-finder. Phys. Lett. B 641 57, 2006.

[131] M.Baak, M.Petteni, and N.Makovec. Data-Quality Requirements and Event Cleaning for Jets and Missing Transverse Energy Reconstruction with the ATLAS Detector in Proton-Proton Collisions at a Center-of-Mass Energy of $\sqrt{s} = 7$ TeV. Technical Report ATLAS-COM-CONF-2010-038, CERN, Geneva, May 2010.

[132] ATLAS Collaboration. Electron performance measurements with the ATLAS detector using the 2010 LHC proton-proton collision data. Eur. Phys. J. C, 72:1909. 45 p, Oct 2011.

[133] A.Quadt. Top quark physics at hadron colliders. Eur.Phys.J., C48:835–1000, 2006.

[134] ATLAS Collaboration. Measurement of the top quark-pair production cross section with ATLAS in *pp* collisions at $\sqrt{s} = 7$ TeV. Eur.Phys.J., C71(1577), 2011. arXiv:hep-ph/1012.1792.

[135] G.Cowan et al. Asymptotic formulae for likelihood-based tests of new physics. Eur.Phys.J., C71(1554), 2011. arXiv:1007.1727.

[136] Glen Cowan. Likelihood ratios for search experiments. PHYSTAT2011. Jan 2011.

[137] W.Lukas. Fast simulation for ATLAS: ATLFAST-II and ISF. May 2012.

[138] E.Torró Pastor, D.Côté, and X.Portell Bueso. Validation of the ATLFAST-II package for the simulation of supersymmetry events. Technical Report ATL-COM-PHYS-2011-1181, CERN, Geneva, Sep 2011.

[139] Glen Cowan, Kyle Cranmer, Eilam Gross, and Ofer Vitells. Asymptotic formulae for likelihood-based tests of new physics. Eur.Phys.J., C71:1554, 2011.

[140] T.Kruker and B.Schneider. How we use HistFitter - Today and Tomorrow. 2012. WP SUSY at 8 TeV : Statistical Interpretations.

[141] ATLAS Collaboration. Improved luminosity determination in pp collisions at $\sqrt{s} = 7$ TeV using the ATLAS detector at the LHC. Eur.Phys.J., C73:2518, 2013.

[142] M.Vetterli. Jets, MET, pileup, and systematic uncertainties (ATLAS/CMS/CDF/D0). Oct 2013. 6th International Workshop on Top Quark Physics.

[143] ATLAS Collaboration. Jet energy measurement and its systematic uncertainty in proton–proton collisions at $\sqrt{s} = 7$ TeV with the ATLAS detector. Technical Report CERN-PH-EP-2013-222. arXiv:1406.0076, CERN, Geneva, May 2014.

[144] G.Landsberg. The LHC: Past, Present, and Future. 2013. 25th Rencontres de Blois on "Particle Physics and Cosmology".

[145] J.B.Hansen. Physics at the LHC in Run2. 2013. WLCG Collaboration Workshop.

[146] W.J.Stirling. http://www.hep.ph.ic.ac.uk/~wstirlin/plots/plots.html. Private Communication.

[147] Observation of the resonant character of the $Z(4430)^-$ state. Technical Report LHCB-PAPER-2014-014, CERN-PH-EP-2014-061, LHCb collaboration, Geneva, 2014.

[148] SHERPA Homepage. http://www.sherpa-mc.de/, 2013.

[149] PYTHIA Homepage. http://home.thep.lu.se/~torbjorn/Pythia.html, 2014.

[150] HERWIG Homepage. http://www.hep.phy.cam.ac.uk/theory/webber/Herwig/, 2014.

[151] M.Bahr et al. Herwig++ Physics and Manual. Eur.Phys.J, (C58):639–707, 2008.

[152] Alpgen Homepage. http://mlm.home.cern.ch/mlm/alpgen/, 2014.

[153] MC@NLO Homepage. http://www.hep.phy.cam.ac.uk/theory/webber/MCatNLO/, 2014.

[154] J.Butterworth and M.Seymour. JIMMY 4: Multiparton Interactions in HERWIG for the LHC. Technical report, Oct 2004.

Acknowledgements

Firstly I would like to thank my Doctoral supervisor Professor Dr. Raimund Ströhmer, and Professor Dr. Werner Porod, the Speaker for DFG Graduate School GRK1147 "Theoretical Astrophysics and Particle Physics", for making this opportunity possible. Along with Professor Dr. Matthias Kadler, the three professors have provided guidance as my "Betreuungskommission" that have benefited me in many invaluable ways.

Professor Ströhmer and Dr Giovanni Siragusa, who have provided guidance and expertise in all aspects throughout the course of the PhD program that have helped me in many ways that are beyond the description of words.

I would like to express my thanks to my colleagues in the Teilchen-PiD working group, Jochen Meyer, Manuel Schreyer, Stefan Weber, Verena Herget and Dominik Köth, as well as many other colleagues from the Graduate School, who has assisted me greatly in overcoming the cultural and language barriers while in Germany, their kind help had provided solutions to many of my obstacles along the way.

My gratitude also extends to Karin Kuhns, Anna Weisensel and Brigitte Wehner, for their administrative assistance which has smoothed out many of my difficulties.

Finally I would like to express my wholehearted appreciation to my family, my wife Sinco and her family, and my friends that have given so much but asked nothing in return. For without their love, support and tolerance, this achievement would

not have been possible and I am truly grateful for the continuous motivation that they have given me.

Erklärung

Hiermit erkläre ich, dass ich die vorliegende Arbeit selbstständig verfasst, keine anderen als die angegebenen Quellen und Hilfsmittel benutzt und die Arbeit bisher oder gleichzeitig keiner anderen Prüfungsbehörde zur Erlangung eines akademischen Grades vorgelegt habe.

Jason Tam
Würzburg, den 24 Juli 2014